

LAMINAR BOUNDARY-LAYER INSTABILITIES ON HYPERSONIC CONES:  
COMPUTATIONS FOR BENCHMARK EXPERIMENTS

A Thesis

Submitted to the Faculty

of

Purdue University

by

Tyler W. Robarge

In Partial Fulfillment of the

Requirements for the Degree

of

Master of Science in Aeronautics and Astronautics

August 2005

Report Documentation Page				Form Approved OMB No. 0704-0188	
Public reporting burden for the collection of information is estimated to average 1 hour per response, including the time for reviewing instructions, searching existing data sources, gathering and maintaining the data needed, and completing and reviewing the collection of information. Send comments regarding this burden estimate or any other aspect of this collection of information, including suggestions for reducing this burden, to Washington Headquarters Services, Directorate for Information Operations and Reports, 1215 Jefferson Davis Highway, Suite 1204, Arlington VA 22202-4302. Respondents should be aware that notwithstanding any other provision of law, no person shall be subject to a penalty for failing to comply with a collection of information if it does not display a currently valid OMB control number.					
1. REPORT DATE <b>00 AUG 2005</b>		2. REPORT TYPE <b>N/A</b>		3. DATES COVERED <b>-</b>	
4. TITLE AND SUBTITLE <b>Laminar Boundary-Layer Instabilities On Hypersonic Cones: Computations For Benchmark Experiments</b>				5a. CONTRACT NUMBER	
				5b. GRANT NUMBER	
				5c. PROGRAM ELEMENT NUMBER	
6. AUTHOR(S)				5d. PROJECT NUMBER	
				5e. TASK NUMBER	
				5f. WORK UNIT NUMBER	
7. PERFORMING ORGANIZATION NAME(S) AND ADDRESS(ES) <b>Purdue University</b>				8. PERFORMING ORGANIZATION REPORT NUMBER	
9. SPONSORING/MONITORING AGENCY NAME(S) AND ADDRESS(ES)				10. SPONSOR/MONITOR'S ACRONYM(S)	
				11. SPONSOR/MONITOR'S REPORT NUMBER(S)	
12. DISTRIBUTION/AVAILABILITY STATEMENT <b>Approved for public release, distribution unlimited</b>					
13. SUPPLEMENTARY NOTES					
14. ABSTRACT					
15. SUBJECT TERMS					
16. SECURITY CLASSIFICATION OF:			17. LIMITATION OF ABSTRACT <b>UU</b>	18. NUMBER OF PAGES <b>146</b>	19a. NAME OF RESPONSIBLE PERSON
a. REPORT <b>unclassified</b>	b. ABSTRACT <b>unclassified</b>	c. THIS PAGE <b>unclassified</b>			

## ACKNOWLEDGMENTS

The author gratefully acknowledges the support of the Fannie and John Hertz Foundation and the Air Force Institute of Technology's Civilian Institutions program. Sandia National Laboratories provided supercomputer access. Equipment and travel support were provided by the Air Force Office of Scientific Research. Additionally, I would like to thank the members of my committee for their time and support.

I especially want to thank Heath Johnson of the University of Minnesota for listening to me and answering my many questions. With all of the years invested in PSE-Chem and STABL, it must have taken a leap of faith to listen to the suggestions of one who had only been working with it for a few months. I appreciate the opportunity to be a part of the project.

Above all, thank you to my wife and parents. This would not have been worth it without your love and support.

The views expressed in this thesis are those of the author and do not reflect the official policy or position of the United States Air Force, Department of Defense, or the U.S. Government.

## TABLE OF CONTENTS

	Page
LIST OF TABLES . . . . .	vi
LIST OF FIGURES . . . . .	vii
SYMBOLS . . . . .	xii
ABSTRACT . . . . .	xv
1 Introduction . . . . .	1
1.1 Transition Prediction Methods . . . . .	2
1.2 Verification and Validation . . . . .	5
2 Code Description . . . . .	7
2.1 History . . . . .	7
2.2 Major Components of STABL . . . . .	8
2.2.1 Grid Generator . . . . .	8
2.2.2 Mean Flow Solver . . . . .	9
2.2.3 Stability Solver . . . . .	13
2.3 Equipment Used . . . . .	18
3 Second Mode Verification: Stetson's Blunt Cone . . . . .	19
3.1 Experimental Conditions . . . . .	19
3.2 Issues Addressed . . . . .	23
3.2.1 Laminar Transport Properties . . . . .	23
3.2.2 Input Conditions . . . . .	33
3.2.3 Boundary-Layer Edge Detection . . . . .	36
3.2.4 Grid Generation . . . . .	38
3.2.5 Wall Temperature . . . . .	40
3.2.6 STABL User Options . . . . .	42
3.2.7 Freestream Thermal Non-Equilibrium . . . . .	44

	Page
3.2.8 Normalization . . . . .	46
3.2.9 Compilers . . . . .	47
3.2.10 Numerical Behavior . . . . .	48
3.3 Computational Comparison . . . . .	51
4 First-Mode Verification . . . . .	59
4.1 Sharp Cone at Mach 3.5 . . . . .	59
4.1.1 Experimental Conditions . . . . .	59
4.1.2 Computational Comparison . . . . .	60
4.1.3 Verification and Validation Issues . . . . .	69
4.2 Large-Bluntness Cone at Mach 8 . . . . .	69
4.2.1 First Mode Stability . . . . .	71
4.2.2 Second Mode Stability . . . . .	74
5 Comparisons to Purdue Mach-6 Ludwig Tube Experiments . . . . .	79
5.1 Sharp Cones . . . . .	81
5.1.1 Sharp Cone: 90 psia . . . . .	81
5.1.2 Sharp Cone: 125 psia . . . . .	86
5.2 Blunt Cones . . . . .	87
5.2.1 Blunt Cone: 125 psia . . . . .	87
5.2.2 Blunt Cone: 45 psia . . . . .	90
5.3 Sensitivity Studies . . . . .	92
6 Conclusions . . . . .	98
LIST OF REFERENCES . . . . .	103
APPENDICES . . . . .	108
Appendix A: Typical N-Factor Script . . . . .	108
Appendix B: STABL User's Guide . . . . .	111
B.1 Prerequisites . . . . .	111
B.2 Method of Operation . . . . .	115
B.3 Final Thoughts . . . . .	120

	Page
Appendix C: Boundary Layer Edge Detection . . . . .	121
Appendix D: Input and Output Data for Rufer's 45 psia Blunt Cone . . .	123
D.1    Mean Flow Input File . . . . .	123
D.2    PSE Script . . . . .	126

## LIST OF TABLES

Table	Page
3.1 Test conditions for Stetson et al. [33] blunt cone experiment for all computations presented here. . . . .	20
3.2 Blottner's Viscosity Curve Fit Coefficients . . . . .	25
3.3 Unit Reynolds number for the Stetson et al. blunt cone experiment calculated using various viscosity models. . . . .	34
3.4 Location of the peak amplification as computed by STABL and several researchers. . . . .	53
3.5 Transition location predicted by STABL for Stetson et al. blunt cone case compared with that predicted by other researchers. Transition was assumed at $N=5.5$ for all computations. . . . .	56
4.1 Test conditions for sharp cone at Mach 3.5 . . . . .	60
4.2 Test conditions for cone with $r_n = 42.67$ mm at Mach 8 . . . . .	71
4.3 Transition location predictions for the large bluntness cone at Mach 8. Transition is assumed at $N = 5.5$ . . . . .	73
5.1 Nominal test conditions for the hot-wire experiments of Rufer [64] . .	80
5.2 Comparison of most unstable frequencies calculated by STABL and measured by Rufer [64]. Transition N factors are also shown for each case. . . . .	85
5.3 Frequencies, N factors, and transition locations for a variety of input conditions for Rufer's blunt cone at a nominal driver tube pressure of 45 psia. Frequencies and N factors are for $x = 20$ inches. . . . .	94
D.1 Grid input conditions for Rufer's 45 psia blunt cone. . . . .	125
D.2 Selected mean-flow data points for Rufer's 45 psia blunt cone. . . . .	128
D.3 Selected PSE N-factor data for Rufer's 45 psia blunt cone. . . . .	129

## LIST OF FIGURES

Figure		Page
1.1	Shadowgraph of a sharp cone in free flight at Mach 4.3. Picture first published by Schneider [4]. . . . .	2
2.1	Representative grids for blunt and sharp cone cases. The range is limited to the nosetip region, and only every tenth grid point is shown for clarity. . . . .	10
2.2	Typical RMS residual and CFL behavior for the mean-flow computations described in this thesis. . . . .	12
3.1	Amplification rate for Stetson's blunt cone at $s/r_n = 175$ with $r_n = 3.81$ mm as computed by other researchers. Symbols are for identification only. . . . .	22
3.2	Viscosity of air computed using various methods compared with experimental data. . . . .	26
3.3	Viscosity models and experimental data for air at low temperatures. . . . .	27
3.4	Temperature variation of Prandtl number and specific heat at constant pressure for air. Data is taken from Keyes [52]. . . . .	29
3.5	Thermal conductivity for air computed using various methods compared with experimental data. . . . .	30
3.6	Thermal conductivity models and experimental data at low temperatures. . . . .	30
3.7	Velocity profile for Stetson's blunt cone at $s/r_n = 175$ with $r_n = 3.81$ mm with original viscosity model and new blended model. . . . .	31
3.8	Second derivative of the velocity in the normal direction for Stetson's blunt cone at $s/r_n = 175$ with $r_n = 3.81$ mm with the original and blended viscosity models. . . . .	32
3.9	Amplification rate with the original and blended viscosity models for Stetson's blunt cone at $s/r_n = 175$ with $r_n = 3.81$ mm. . . . .	33
3.10	Amplification rates computed using two different values of freestream density for Stetson's blunt cone at $s/r_n = 175$ with $r_n = 3.81$ mm. . . . .	35



Figure	Page
3.11 N factors computed using two different values of freestream density for Stetson's blunt cone with $r_n = 3.81$ mm. . . . .	36
3.12 Representative total enthalpy and mass flux profiles. . . . .	38
3.13 Amplification rate for Stetson's blunt cone at $s/r_n = 175$ with $r_n = 3.81$ mm computed using mean flows with varying grid resolutions. . . . .	39
3.14 N factors computed using mean flows with varying grid resolutions for Stetson's blunt cone with $r_n = 3.81$ mm. . . . .	39
3.15 Surface temperature distribution for Stetson's blunt cone with $r_n = 3.81$ mm as computed by STABL and by Lyttle et al. [41]. . . . .	41
3.16 Amplification rate for Stetson's blunt cone at $s/r_n = 175$ with $r_n = 3.81$ mm computed using mean flows with the surface temperature distributions calculated by Lyttle and STABL. . . . .	42
3.17 N factors for Stetson's blunt cone with $r_n = 3.81$ mm computed using mean flows with the surface temperature distributions calculated by Lyttle and STABL. . . . .	43
3.18 Amplification rate curves for Stetson's blunt cone at $s/r_n = 175$ with $r_n = 3.81$ mm computed using various user-specified options in STABL. . . . .	43
3.19 N factor curves for Stetson's blunt cone with $r_n = 3.81$ mm computed using various user-specified options in STABL. . . . .	44
3.20 N factors calculated for Stetson's blunt cone with $r_n = 3.81$ mm assuming both equilibrium and frozen thermal states. . . . .	45
3.21 The effect of using different C and Fortran compilers on complex wave number for Stetson's blunt cone at $s/r_n = 175$ with $r_n = 3.81$ mm. . . . .	47
3.22 Amplification curve for Stetson's blunt cone with $r_n = 3.81$ mm at $s = 0.3$ m showing the existence of multiple families of solutions with different phase speeds. . . . .	48
3.23 Amplification curves for Stetson's blunt cone at $s/r_n = 175$ with $r_n = 3.81$ mm obtained with the original extrapolation routine and with the modified extrapolation routine. . . . .	49
3.24 Spatial growth rate and N factor for Stetson's blunt cone with $r_n = 3.81$ mm computed using different step sizes for the PSE marching procedure. . . . .	50
3.25 Mean velocity profile for conditions of Stetson et al. [33] at $s/r_n = 175$ with $r_n = 3.81$ mm compared with the results of Kufner et al. [36]. . . . .	51

Figure	Page
3.26 Second normal derivative of velocity profile for conditions of Stetson et al. [33] at $s/r_n = 175$ with $r_n = 3.81$ mm compared with the results of Kufner et al. [36] and Esfahanian [35]. . . . .	52
3.27 Amplification rate for conditions of Stetson et al. [33] at $s/r_n = 175$ with $r_n = 3.81$ mm. . . . .	52
3.28 Amplification rate for Stetson's blunt cone with $r_n = 3.81$ mm at $s/r_n = 215$ compared with the data of Malik et al. [34]. . . . .	54
3.29 Amplification rate curves at axial locations ranging from $s = 0.3$ m to $s = 1.0$ m for Stetson's blunt cone with $r_n = 3.81$ mm. . . . .	54
3.30 Maximum N factors obtained for various frequencies for Stetson's blunt cone with $r_n = 3.81$ mm. . . . .	55
3.31 Comparison of N factors calculated by STABL with local N factors of Rosenboom et al. [38] for Stetson's blunt cone with $r_n = 3.81$ mm. . .	57
3.32 Amplitude and phase of the temperature eigenfunction at the aft end of the cone for Stetson's blunt cone with $r_n = 3.81$ mm. . . . .	58
3.33 Amplitude and phase of the pressure eigenfunction at the aft end of the cone for Stetson's blunt cone with $r_n = 3.81$ mm. . . . .	58
4.1 Lines of constant pressure at the nosetip for a sharp cone at Mach 3.5.	61
4.2 Mean flow velocity profiles for the sharp cone at Mach 3.5 at several axial locations. . . . .	62
4.3 Mean flow temperature profiles for the sharp cone at Mach 3.5 at several axial locations. . . . .	62
4.4 Amplification rate for the sharp cone at Mach 3.5 as a function of frequency and wave angle for various axial locations. . . . .	64
4.5 N factor calculations for the sharp cone at Mach 3.5 with five separate mean flow grids. Calculations are for a mode with $\omega = 104$ kHz and $\beta = 2400/\text{m}$ , beginning at $s = 0.0339$ m. . . . .	65
4.6 Maximum N factors obtained from many combinations of frequency, spanwise wavenumber, and starting location for the sharp cone at Mach 3.5. . . . .	65
4.7 Ratio of edge momentum thickness Reynolds number to edge Mach number for the sharp cone at Mach 3.5. . . . .	66
4.8 The phase speed for the five most amplified modes on the sharp cone at Mach 3.5. . . . .	66

Figure	Page
4.9 The wave angle for the five most amplified modes on the sharp cone at Mach 3.5. . . . .	67
4.10 Amplitude and phase of the temperature eigenfunction for a 104 kHz disturbance with $\beta = 2400$ 1/m at the aft end of the sharp cone at Mach 3.5. . . . .	68
4.11 Amplitude and phase of the pressure eigenfunction for a 104 kHz disturbance with $\beta = 2400$ 1/m at the aft end of the sharp cone at Mach 3.5. . . . .	68
4.12 N factors calculated using STABL compared with results of Kimmel using $e^{Malik}$ for a mode at 104 kHz with $\beta = 2400$ 1/m for the sharp cone at Mach 3.5. . . . .	70
4.13 First mode N factors for the large bluntness cone at Mach 8. . . . .	72
4.14 Second mode amplification curves for the large-bluntness cone at Mach 8. 74	
4.15 Second mode N factors for the large-bluntness cone at Mach 8. . . . .	75
4.16 A comparison of the spatial growth rates of the largest first and second-mode N factors for the large-bluntness cone at Mach 8. . . . .	76
4.17 A comparison of the largest first and second-mode N factors calculated by STABL for the large bluntness cone at Mach 8. . . . .	77
4.18 N factors of a two-dimensional instability at 1 kHz on the large-bluntness cone at Mach 8. The four lines represent different beginning marching locations. . . . .	77
5.1 N factors calculated for Rufer's blunt cone at 125 psia using two separate grids. . . . .	81
5.2 A comparison of the mass flux calculated by STABL with the uncalibrated hot wire measurements of Rufer at two locations on the sharp cone at 90 psia. . . . .	82
5.3 Amplification rate curves for Rufer's sharp cone at 90 psia. The spacing between the curves is two inches. . . . .	83
5.4 N factors for Rufer's sharp cone at 90 psia. The spacing between the curves is 10 kHz. . . . .	84
5.5 Amplification rate curves for Rufer's sharp cone at 125 psia. The spacing between the curves is two inches. . . . .	85

Figure	Page
5.6 N factors for Rufer's sharp cone at 90 psia. The spacing between the curves is 20 kHz. . . . .	86
5.7 A comparison of the mass flux calculated by STABL with the uncalibrated hot wire measurements of Rufer at $x = 14.25$ inches on the blunt cone at 125 psia. . . . .	87
5.8 Amplification rate curves for Rufer's blunt cone at 125 psia. The spacing between the curves is two inches. . . . .	88
5.9 N factor curves for Rufer's blunt cone at 125 psia. The spacing between the curves is 20 kHz. . . . .	88
5.10 Frequency spectra measured by Rufer at $x = 14.25$ inches on the blunt cone at 125 psia. . . . .	89
5.11 A comparison of the mass flux calculated by STABL with the uncalibrated hot wire measurements of Rufer at two locations on the blunt cone at 45 psia. . . . .	90
5.12 Amplification rate curves for Rufer's blunt cone at 45 psia. The spacing between the curves is two inches. . . . .	91
5.13 N factors for Rufer's blunt cone at 45 psia. The spacing between the curves is 10 kHz. . . . .	92
5.14 N factor curves obtained with various perturbations to nominal boundary conditions for Rufer's 45 psia blunt cone. . . . .	93
5.15 N factors and transition locations obtained with various perturbations to nominal boundary conditions for Rufer's 45 psia blunt cone. . . .	94
5.16 Wall temperature distribution "dist1" used in sensitivity study on Rufer's 45 psia blunt cone. . . . .	96
5.17 Amplification rate curves at $x = 20$ inches for baseline and perturbed boundary conditions. . . . .	97

## SYMBOLS

$C_p$	specific heat at constant pressure
$C_v$	specific heat at constant volume
$c_r$	phase speed
$E$	disturbance kinetic energy
$e_v$	vibrational energy
$h$	enthalpy
$\vec{k}$	wavenumber vector
$k$	thermal conductivity
$M$	Mach number; molecular weight
$ns$	number of species in a mixture
$Pr$	Prandtl number
$p$	pressure
$R$	stability Reynolds number $R = \sqrt{\frac{U_\epsilon s}{\nu_\epsilon}}$ ; Universal gas constant, 8.3144 J/mol-K
$Re_\theta$	Reynolds number $Re = \frac{U_\epsilon \theta}{\nu_\epsilon}$
$Re_{\infty, s}$	Reynolds number $Re = \frac{U_\infty s}{\nu_\infty}$
$r_n$	nose radius
$S$	Sutherland constant
$s$	arc length along the body surface
$T$	temperature
$t$	time
$U$	mean velocity
$u$	velocity in streamwise direction
$v$	velocity in body-normal direction
$w$	velocity in spanwise direction

$x$	distance in streamwise direction
$y$	distance in body-normal direction
$z$	distance in spanwise direction
$\alpha$	streamwise complex wavenumber
$\beta$	spanwise complex wavenumber
$\varepsilon$	numerical dissipation parameter
$\eta$	wall-normal computational coordinate
$\theta$	momentum thickness
$\mu$	first coefficient of viscosity
$\nu$	kinematic viscosity
$\rho$	density
$\sigma$	disturbance growth rate
$\phi$	vector of disturbance quantities; cone half angle
$\xi$	streamwise computational coordinate
$\psi$	shape function; wave angle
$\Omega$	domain of integration for PSE
$\omega$	frequency

#### Subscripts

$e$	edge conditions
$i$	imaginary component; computational coordinate in the body-parallel direction
$j$	computational coordinate in the body-normal direction
$o$	stagnation conditions
$r$	real component
$rot$	component of the rotational mode
$s$	relating to a specific chemical species
$tr$	translational; transition
$vib$	vibrational

$\theta$	component of the azimuthal directions
$\infty$	freestream conditions

#### Superscripts

$-$	mean component
$'$	fluctuating component
$\sim$	form of Jacobian in Equation 2.4
$\wedge$	form of Jacobian in Equation 2.7
$\hat{\phantom{x}}$	fluctuating component in computational space

#### Acronyms

AEDC	Arnold Engineering and Development Center
CFL	Courant-Friedrichs-Lewy number
GUI	Graphical User Interface
LST	Linear Stability Theory
M6LT	Mach-6 Ludwig Tube
PSE	Parabolized Stability Equations
RMS	Root mean square
SMP	Symmetric Multi-Processing

# ABSTRACT

Robarge, Tyler W. MSAE, Purdue University, August, 2005. Laminar Boundary-Layer Instabilities on Hypersonic Cones: Computations for Benchmark Experiments. Major Professor: Steven P. Schneider.

Although significant advances have been made in hypersonic boundary-layer transition prediction in the last several decades, most design work still relies on unreliable empirical correlations or wind-tunnel tests. Codes using the semi-empirical  $e^N$  method will need to be well verified and validated before being used for expensive flight vehicles. The code package STABL and its PSE-Chem stability solver are used to compute first and second-mode instabilities for both sharp and blunt cones at wind-tunnel conditions using a Navier-Stokes mean-flow solution. Computations are performed for Stetson's 3.81 mm nose-radius cone, a sharp cone at Mach 3.5, a large-bluntness cone at Mach 8, and sharp and blunt cones corresponding to the experiments of Rufer. Comparisons to previous computations by other researchers show differences on the order of 10% in local amplification rates and frequencies, but better agreement is obtained for the transition location. Many issues are examined for verification and validation, including the laminar transport properties, the freestream boundary conditions, and the effect of freestream thermal nonequilibrium. This work helps to verify and validate STABL, extend its applicability to low-temperature flows, and develop the methodologies for using STABL.



## 1. Introduction

Despite more than fifty years of hypersonics research, many critical areas are still poorly understood [1]. Hypersonic flight remains a top priority in defense research, as any vehicle that ascends to or from space must traverse the hypersonic regime. An Air Force Scientific Advisory Board study found that hypersonics will be necessary to fulfill the Air Force's vision of "controlling and exploiting the full aerospace continuum" [2]. The reduction in forward-deployed forces since the end of the Cold War has increased the need for hypersonics, as a need remains to be able to strike high-value, time-critical targets anywhere in the world in minutes or hours [3]. Hypersonic flight is a key component of most plans to provide that capability.

The location and extent of laminar-to-turbulent boundary-layer transition is a critical parameter in hypersonic vehicle design [1]. The transition location directly affects estimates of aeroheating and skin friction drag, which in turn affect heat shield weight and materials, range, and payload capacity. Infrared and radar signatures, as well as communications with the vehicle, are also affected by transition. Vehicle designers can now compute the laminar and turbulent aeroheating with good accuracy; in many cases, the largest uncertainty in calculating the total heat flux to the vehicle results from the estimates of transition location [4]. As an example, the Defense Science Board found that estimates for transition location on the National Aerospace Plane ranged from 20% to 80% of the body, and the estimate used could affect the vehicle gross takeoff weight by a factor of two or more [5]. Transition is especially important on vehicles that spend a significant amount of time in high-speed, high-altitude atmospheric flight, such as hypersonic cruise vehicles and maneuvering reentry vehicles.

Figure 1.1 shows a magnified portion of a shadowgraph of a sharp cone model in free flight at Mach 4.3 in the Naval Ordnance Lab ballistics range. This photograph,

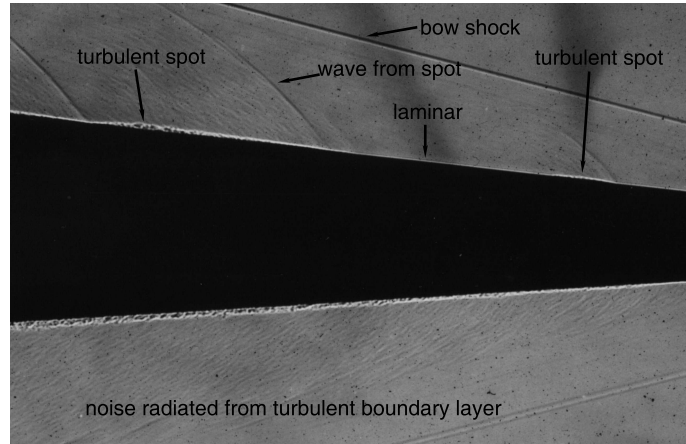


Figure 1.1: Shadowgraph of a sharp cone in free flight at Mach 4.3. Picture first published by Schneider [4].

first published by Schneider [4], illustrates many of the salient features of hypersonic boundary-layer transition. The boundary layer on the upper surface of the cone is mostly laminar with discrete turbulent spots. Small shocks are visible forward of the spots. The visible lower surface is entirely turbulent, and acoustic noise can be seen radiated from the boundary layer. A vast difference in the boundary-layer thickness between the laminar and turbulent states is evident.

## 1.1 Transition Prediction Methods

The overall transition process is not well understood [6]. Environmental disturbances, which could come from either the freestream or the body, enter the boundary layer through a process called receptivity. These disturbances amplify through one or more of many possible mechanisms. This thesis will consider only first and second mode amplification, but roughness-induced transition, cross-flow vortices, and Görtler instabilities are all examples of other mechanisms that are dominant under various conditions. As the disturbances amplify, they will eventually breakdown in a nonlinear fashion, form turbulent spots, and develop into full turbulence.

Despite this complex nature of transition, transition prediction for vehicle design has historically relied on empirical correlations and extrapolations from wind tunnel experiments. A large body of empirical and semi-empirical correlations exist; many of these were cataloged and evaluated by Berkowitz et al. [7]. One popular correlation is shown in Equation 1.1.

$$\frac{Re_\theta}{M_e} = C \quad (1.1)$$

The constant  $C$  is specified based on empirical data and is usually in the range of 100–500. Transition is assumed to occur when the local boundary-layer properties satisfy Equation 1.1. The designers of the Space Shuttle used Equation 1.1 and applied a correction based on the surface roughness caused by misaligned Thermal Protection System tiles [8].

As Berkowitz et al. showed, many correlations exist, and most fit some subset of the experimental data. However, no empirical model can accurately predict transition for a general dataset [1]. In fact, Schneider [9] has shown that for a general data set the predictions generated by different correlations scatter by a factor of 3 in momentum thickness Reynolds number and an order of magnitude in arc length Reynolds number. None of the correlations can be expected to provide accurate predictions for configurations and conditions outside of the database used for their development.

Extrapolating from wind tunnel experiments is also problematic. Transition depends on a multitude of factors, including local Mach number, flow enthalpy, unit Reynolds number, surface roughness, reacting chemistry, and mass ablation [6]. Any single ground facility can only match a small subset of these parameters, and even then determining the location and extent of transition in an accurate and consistent manner is not a trivial task [1]. Further complicating matters, the acoustic noise produced by the turbulent boundary layer on the walls of conventional hypersonic wind tunnels produces a freestream disturbance environment markedly different from that of flight. These disturbances have been shown to affect not only the transition location, but also the parametric trends [10]. This has led to a push for the devel-

opment of ‘quiet’ tunnels, but that itself is an exercise in boundary-layer transition prediction and control. There are currently no hypersonic wind tunnels that are quiet at significant Reynolds numbers, anywhere in the world [11].

Given the constraints of ground testing, the only situation that can accurately capture all of the relevant flow-field characteristics is flight. However, flight testing usually only permits surface measurements, and recovery of the actual vehicle is often impossible. Flight testing is extremely expensive, and sufficient funds are not likely to be available in the foreseeable future.

Much research in hypersonic boundary-layer transition has been accomplished in the last fifty years. In particular, Linear Stability Theory (LST) [12] and the Parabolized Stability Equations (PSE) [13] have been coupled with the semi-empirical  $e^N$  method to predict transition on simple geometries, such as cones and flat plates. More details on all of these methods will be provided in Chapter 2. Recently, Malik [14] showed that transition locations could be correlated on two hypersonic flight tests using the PSE for chemically reacting flows and the  $e^N$  method. Although these methods have shown success for many applications in research settings [6], hypersonic vehicle designers are hesitant to stake expensive programs on these newer methods until they have been shown to be better validated, faster, and simpler to use. Given these constraints, Oberkampf and Blottner [15] assert that reliable engineering techniques for transition prediction are currently lacking.

Since hypersonic vehicles remain a priority, and current design methods are inadequate for many applications, an improved method for hypersonic boundary-layer transition prediction is needed. The overall project that this work is a part of aims to provide mechanism-based methods that are suitable for design purposes, including predictions using the PSE and the  $e^N$  method. The present work is concerned primarily with the verification and validation of the 2D/axisymmetric version of the PSE/ $e^N$  code package. This code package will not be the final solution to the problem of transition prediction, as the only mechanisms currently included are the first and second mode, and the effects of receptivity and nonlinear breakdown are treated

empirically. However, it is hoped that the inclusion of more of the relevant flow physics will result in a more accurate and more robust method than those which are currently in use.

## 1.2 Verification and Validation

Before computational results can be used to make important decisions, measures must be taken to ensure confidence in the accuracy of the predictions. Although this issue has received considerable attention in recent years, developments in this area have not kept pace with increases in code size and complexity and the increasing reliance on computations to reduce the number and scope of wind tunnel and flight tests [16]. Attention to code quality, implementation, and the applicability of the algorithms and assumptions is required throughout all stages of code creation and use, but even this does not ensure that a code is free from defects. As an example, an inexperienced user can get incorrect results from a validated code.

Blottner [17] defines code validation as solving the right governing equations and code verification as solving the governing equations right. Examples of validation include confirming the accuracy of the assumptions made, such as when using the Euler instead of the Navier-Stokes equations, or comparing the accuracy of the closure models throughout the relevant parameter space. Verification means evaluating the accuracy of the numerical procedures used to solve the governing equations. Examples of verification include checking for general programming errors and ensuring that results are converged and grid independent. Code validation can only be accomplished by detailed comparisons to experimental data [18], and the validation of applicable equations and models is a responsibility of the community at large. In general, a code must be verified before it can be fully validated.

Oberkampf and Blottner [15] divide the sources of physical modeling errors into three categories: the partial differential equations (PDEs), the closure models, and the boundary conditions. The set of PDEs analyzed must be appropriate for the

flow phenomena of interest. In addition, the accuracy of the solution depends not just on the continuum mathematical model used to describe the flow, but also on the accuracy of the discrete approximation used to solve that model. The closure models must be accurate and valid for the full parameter space of temperature, density, etc. The boundary conditions are arguably the hardest to accurately model, as this requires detailed knowledge of the inflow and outflow profiles and disturbance spectra. This is rarely available, even in careful experiments designed for code validation. Aeschliman and Oberkampf [19] provide a good description of the type of experimental and computational procedure necessary to rigorously validate a code.

Verification is a difficult task, and it is never fully completed. Hatton and Roberts [20] found from a study of seismic data-processing software packages that numerical disagreement among commercially available codes grows at about 1% in average absolute difference per 4000 lines of code, and that the Fortran codes had a static fault rate of 6 per 1000 lines of code. These errors among the various packages examined led to results that were all reasonable but subtly different, making it impossible for even trained scientists to evaluate which results were the most accurate. Given that these results were obtained for a mature, highly competitive field, where the algorithms are well established and over fifteen independent packages exist to perform the same function, it is highly probable that the situation is worse for hypersonic transition prediction, where funding is insufficient to support many competing products.

Several approaches exist for code verification, including grid refinement studies, varying the boundary conditions, solving problems that have an analytical solution, and comparing results with previously verified codes [16,18]. Grid refinement studies and comparisons with other codes will be used in the present effort. This work expands on previous verification and validation work by Johnson and Johnson et al. [21–24].

## 2. Code Description

The computations presented in this thesis were performed using the STABL code package [24]. STABL is designed to be a comprehensive boundary-layer stability-analysis and transition-prediction tool, and it includes a mean flow code, a stability code, and other utilities such as a Graphical User Interface (GUI) and a grid generator. STABL is modular in nature, allowing individual components to be used instead of the whole package.

### 2.1 History

The heart of STABL is its stability code, PSE-Chem. PSE-Chem was written by Heath B. Johnson as part of his Ph.D. research under Professor Graham Candler at the University of Minnesota in the late 1990s. The original PSE-Chem was a research code with a very utilitarian user interface and very little documentation apart from the extensive comments within the source code. The Navier-Stokes code DPLR2D [25], written by Michael Wright, another of Professor Candler's former students, was used for the mean flow calculations.

After completing his degree, Johnson began improving the PSE-Chem code and the other components to add new capabilities and to make them more user-friendly. When the author began using the code package in December of 2003, he was the first individual outside of Professor Candler's research group to use the code. At the time, the user's manual was approximately fifteen pages long, a minimal GUI was in place, and compiling the codes required manually editing the makefiles to configure system-specific variables.

Over the course of the next eighteen months, the author served as the primary tester for new components and features released by Dr. Johnson. Many improve-

ments were made to the package, allowing for a much easier learning curve for new users. A large percentage of these improvements directly resulted from suggestions or ideas raised by the author. Over the successive months, a script was added that allows a user to answer a series of questions to configure the system-specific variables, which mostly eliminated the need to edit the obscure makefiles. The GUI was expanded and improved, such as through the addition of a flow analysis tool to allow for easier interpretation of mean flow results. Algorithm changes, detailed in later chapters, were made to provide more accurate and robust results.

In March of 2004, version 1.1 was released, and in April of 2004, the package was renamed to Stability and Transition Analysis for hypersonic Boundary Layers (STABL). The computations presented in this thesis were performed using versions of STABL ranging from 1.26 to 1.29.4. The ongoing development of STABL made obtaining all results with a consistent version impractical. Additional details about STABL can be found in the STABL Program Reference [26] and in Johnson and Candler [24].

## **2.2 Major Components of STABL**

### **2.2.1 Grid Generator**

The grids used for the mean flow solutions were created using the grid generator included with STABL. The model surface and outer boundaries were each specified using a single arc section and one or more line segments. In the case of a sharp cone, only line segments were used. As the mean flow solver uses a shock capturing scheme, the domain outer boundary had to be carefully defined to closely follow the shock shape to minimize the number of grid lines crossing the shock. Since the shock shape is not known *a priori*, an iterative approach was used in which a coarse, poorly fitted grid was used to obtain a solution, and the grid parameters were adjusted until the outer boundary of the new grid matched the shock shape in the original solution



with a small offset. A second mean flow solution was then obtained using the new grid parameters with a higher mesh density.

The lines of constant  $i$  were constrained to be always normal to the wall. This is necessary within the boundary layer for stability analyses. The distribution of points on the body surface was specified, and the distribution on the outer boundary was determined by the wall-normal requirement. For blunt nose grids, the surface spacing was uniform on the spherical portion of the nose, and a form of exponential stretching using two segments was employed to expand the spacing downstream.

The lines of constant  $j$  were constructed by interpolating between spacings specified at the upstream and downstream boundaries. Exponential stretching was used to cluster points within the boundary layer. An experiment was conducted in which grid points were clustered at both the wall and the boundary-layer edge. A mean flow solution was analyzed to give the edge location, and that data was fed along with the axial point distribution into the commercial software GRIDGEN. The grid was constructed in GRIDGEN and exported, and the resulting file was converted to the format required by the mean flow solver. The process was extremely cumbersome, and no significant difference was seen in the stability results. The large total number of grid points used reduced the need for more advanced clustering schemes.

Figure 2.1 shows examples of typical grids for both blunt and sharp cones. For clarity, only every tenth point is shown, and the range is limited to the nosetip region.

### 2.2.2 Mean Flow Solver

A modified form of the mean flow solver DPLR2D is included with STABL. DPLR2D solves the finite-volume axisymmetric Navier-Stokes equations for real gas flows in chemical and thermal nonequilibrium using a general chemistry model.

DPLR2D is based on the data-parallel line relaxation method, described by Wright et al. [25]. The use of an implicit method allows for rapid convergence of the stiff equation set that results from the vastly different length scales encountered

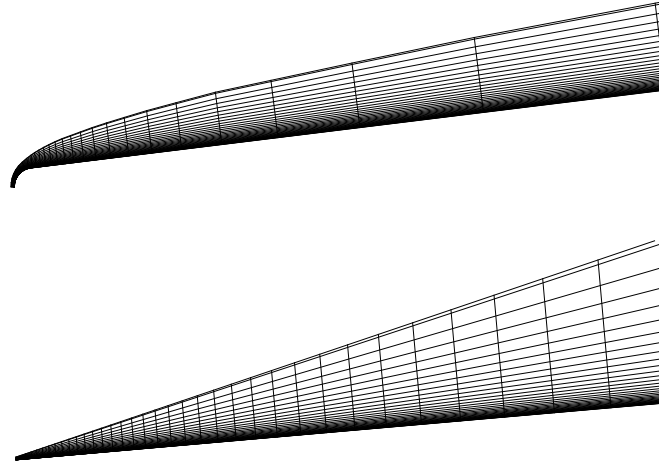


Figure 2.1: Representative grids for blunt and sharp cone cases. The range is limited to the nosetip region, and only every tenth grid point is shown for clarity.

in high Reynolds number flows. DPLR2D takes advantage of the structured mesh to provide for efficient interprocessor communication without explicit domain decomposition. The resulting method combines the parallelization of the data-parallel lower-upper relaxation method with the high cell aspect ratio convergence properties of the Gauss-Seidel line relaxation method. DPLR2D parallelizes extremely efficiently, allowing for very large problem sizes constrained primarily by available memory.

A modified form of Steger-Warming flux vector splitting is used to give an accurate solution within the boundary layer. The original flux vector splitting method proposed by Steger and Warming [27] was developed primarily for the solution of inviscid flows. MacCormack and Candler [28] showed that flux splitting causes problems in boundary layers through either abnormally large numerical mixing or a fictitious pressure gradient. Their modification makes the method much more accurate within boundary layers. Second order accuracy is used in both the streamwise and

wall-normal directions, but a limiter switches the algorithm to first order accuracy near the shock.

DPLR2D has excellent convergence properties. The highest stable Courant-Friedrichs-Lewy (CFL) number begins near one and rapidly increases as the solution converges. A set of CFL numbers can be specified in the input file, and a suggestion by the author led to a modification to allow a user to change the CFL number on-the-fly, which proved helpful when working on a time-sharing system. Stable CFL numbers of at least 10,000 are attainable, although 2,000 was usually the maximum used to obtain solutions for this thesis. The maximum stable CFL number decreases with increasing mesh density and aspect ratio, so DPLR2D offers the option to freeze a portion of the solution from the stagnation point to a specified distance once that portion is sufficiently converged. This freezing stops the iterations in the specified area, which eliminates the highest aspect-ratio cells from the solution space, allowing for higher CFL numbers and faster convergence of the downstream section. Although this option is helpful, it was not used for most of the cases presented in this thesis since it was easier to let the solution run overnight unattended. This option will probably be more beneficial for design purposes when the amount of analysis time needed for any given configuration is less.

Boundary conditions are specified at the freestream, outflow, and wall. At the wall, a no-slip condition is imposed along with requirements for zero wall-normal pressure gradients and mass concentration gradients. Either an adiabatic wall or a specified wall temperature was assumed, as indicated for each individual case. The Mach number, static density, static translational and vibrational temperatures, and species mass fractions are specified in the freestream. The inflow and outflow boundaries are supersonic except in the boundary layer. A zero gradient condition is applied at the outflow boundary. Zero gradient is also assumed along the outer domain boundary to ensure relaxation of the flow variables.

Real gas effects are modeled following the method of Candler and MacCormack [29]. These effects include non-equilibrium chemical reactions and thermal

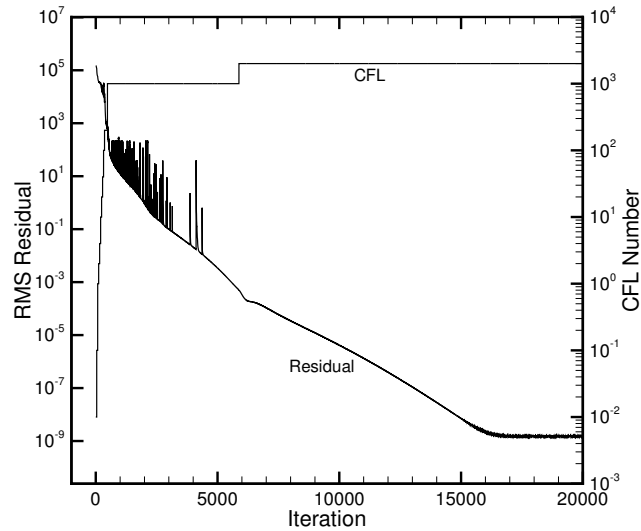


Figure 2.2: Typical RMS residual and CFL behavior for the mean-flow computations described in this thesis.

non-equilibrium and have been shown to be critical factors in obtaining accurate predictions of boundary-layer stability and transition for high enthalpy flows [21]. For the cases presented here, a five-species air model consisting of  $N_2$ ,  $O_2$ ,  $N$ ,  $O$ , and  $NO$  was used with the standard freestream mass fractions of 76.7%  $N_2$  and 23.3%  $O_2$  (79%  $N_2$  and 21%  $O_2$  by volume) [24]. Thermal equilibrium was assumed in the freestream except where otherwise specified. Section 3.2.1 gives a detailed discussion of the transport properties used. Stoke's hypothesis is used for the bulk viscosity. Equilibrium constants and other properties are taken from the NASA thermodynamic data file for the CEA program [30]. The stability solver also used this chemistry modeling.

The residuals were checked in two stages to ensure iterative convergence. DPLR prints a convergence file that includes the RMS residual based on the density. That value was monitored during the run, and a typical convergence history can be seen in Figure 2.2. A residual drop of approximately 14 orders of magnitude is present.

The spikes within the first 5000 iterations are thought to be due to fluctuations in the location of the shock relative to the grid lines. The CFL number started small but was rapidly increased by five orders of magnitude. As a second check on the convergence, after the RMS had flattened, contour plots of the residual were plotted using an exponential scale to look for any local spots of higher residual and to ensure that the solution was fully converged on the aft end of the body.

### 2.2.3 Stability Solver

The code PSE-Chem is used to analyze the stability of the laminar mean flow profiles. PSE-Chem uses the linear PSE coupled with the  $e^N$  method to produce transition predictions. Since the PSE constitute an initial-boundary-value problem, the wavenumber and eigenfunction at the starting location are obtained from LST. A summary of the relevant equations and their derivation will be given here for familiarization. The full derivation used in PSE-Chem is given by Johnson [23].

The stability equations are obtained from the Navier-Stokes equations by first decomposing the instantaneous flow into a mean and a fluctuating component,  $q = \bar{q} + q'$ , where  $q$  is any flow variable. This decomposed form is substituted into the Navier-Stokes equations, and the mean flow equation is subtracted, resulting in the disturbance equation given in Equation 2.1, where  $\phi$  is the vector of disturbance quantities given in Equation 2.2.

$$\begin{aligned} \Gamma \frac{\partial \phi}{\partial t} + A \frac{\partial \phi}{\partial x} + B \frac{\partial \phi}{\partial y} + C \frac{\partial \phi}{\partial z} + D\phi + V_{xx} \frac{\partial^2 \phi}{\partial x^2} + V_{yy} \frac{\partial^2 \phi}{\partial y^2} \\ + V_{zz} \frac{\partial^2 \phi}{\partial z^2} + V_{xy} \frac{\partial^2 \phi}{\partial x \partial y} + V_{xz} \frac{\partial^2 \phi}{\partial x \partial z} + V_{yz} \frac{\partial^2 \phi}{\partial y \partial z} + F^n = 0 \end{aligned} \quad (2.1)$$

$$\phi = (\rho'_1, \rho'_2, \dots, \rho'_{ns}, u', v', w', T', T'_v)^T \quad (2.2)$$

The terms in the Jacobian matrices  $\Gamma, A, B, \dots, V_{yz}$  depend only on the known mean-flow variables and their derivatives, and all of the terms that vary nonlinearly with  $\phi$  are contained in the vector  $F^n$ .

The disturbance quantities are assumed to be traveling waves of the form given by Equation 2.3.

$$\phi = \chi(\xi, \eta) e^{i(kz - \omega t)} \quad (2.3)$$

Here  $\xi$  and  $\eta$  are the body-tangential and body-normal computational coordinates,  $k$  is the real spanwise wavenumber,  $z$  is the distance in the spanwise direction, and  $\omega$  is the real frequency.

When Equation 2.3 is substituted into Equation 2.1, the derivatives are calculated, and the equation is converted to computational coordinates, the result is Equation 2.4, where the Jacobians are given in Reference [23].

$$\tilde{D}\phi + \tilde{A}\frac{\partial\phi}{\partial\xi} + \tilde{B}\frac{\partial\phi}{\partial\eta} + \hat{V}_{\xi\xi}\frac{\partial^2\phi}{\partial\xi^2} + \hat{V}_{\eta\eta}\frac{\partial^2\phi}{\partial\eta^2} + \hat{V}_{\xi\eta}\frac{\partial^2\phi}{\partial\xi\partial\eta} + F^n = 0 \quad (2.4)$$

$\chi$  is decomposed using Equations 2.5 and 2.6,

$$\chi = \psi(\xi, \eta) A(\xi) \quad (2.5)$$

$$A(\xi) = e^{i\theta(\xi)} \quad (2.6)$$

where  $d\theta/d\xi = \alpha(\xi)$ ,  $\alpha$  is the body-parallel wavenumber in computational coordinates, and  $\psi$  is the shape function vector. This allows for all of the ellipticity in the wave function to be retained while parabolizing only the shape factor. After further substitutions and rearranging, the result is the disturbance equations in computational coordinates,

$$\hat{D}\psi + \hat{A}\frac{\partial\psi}{\partial\xi} + \hat{B}\frac{\partial\psi}{\partial\eta} + \hat{V}_{\xi\xi}\frac{\partial^2\psi}{\partial\xi^2} + \hat{V}_{\eta\eta}\frac{\partial^2\psi}{\partial\eta^2} + \hat{V}_{\xi\eta}\frac{\partial^2\psi}{\partial\xi\partial\eta} + \hat{F}^n = 0 \quad (2.7)$$

To arrive at the PSE, the terms  $\hat{V}_{\xi\xi}\frac{\partial^2\psi}{\partial\xi^2}$  and  $\hat{V}_{\xi\eta}\frac{\partial^2\psi}{\partial\xi\partial\eta}$  are neglected. The disturbances are assumed to be small, allowing the nonlinear terms that comprise  $\hat{F}^n$  to be neglected as well. The resulting terms give the linear PSE,

$$\hat{D}\psi + \hat{A}\frac{\partial\psi}{\partial\xi} + \hat{B}\frac{\partial\psi}{\partial\eta} + \hat{V}_{\eta\eta}\frac{\partial^2\psi}{\partial\eta^2} = 0 \quad (2.8)$$

The PSE constitute an initial boundary value problem, and the marching procedure requires an initial wavenumber solution, which is obtained from the linear

stability equations. These are obtained by assuming a quasi-parallel flow, which means that  $\psi = \psi(\eta)$  and  $d\alpha/d\xi = 0$ . Equation 2.9 gives the resulting linear stability equations.

$$\hat{D}\psi + \hat{B}\frac{\partial\psi}{\partial\eta} + \hat{V}_{\eta\eta}\frac{\partial^2\psi}{\partial\eta^2} = 0 \quad (2.9)$$

These equations are solved using the global and local two-step procedure of Malik [31].

In the global procedure, the approximation that  $\alpha^2 = 0$  is made. This results in a generalized eigenvalue problem for the complex wavenumber  $\alpha$ . Second-order central differences are used to discretize the  $\eta$  derivatives. The boundary conditions of zero velocity and temperature disturbances and zero disturbance pressure gradient are imposed at the wall. Zero disturbances are imposed for all variables at the outer domain. The generalized eigenvalue problem is solved using the LZ algorithm [32]. The result is a spectrum of approximate eigenvalue guesses for the complex wavenumber  $\alpha$ .

The local procedure is then used to refine the wavenumber guesses produced by the global method. Since the global process is computationally expensive, it is run for a small number of frequencies and PSE-Chem interpolates those results to intermediate frequencies. Discretization is accomplished through fourth-order central differences at the interior points and second-order central differences at the boundaries. A non-homogeneous boundary condition must be imposed to prevent arriving at the trivial solution for Equation 2.9. The  $\hat{u} = 0$  condition is replaced with a normalization condition for the density fluctuation  $\hat{\rho} = \rho_{norm} = \rho_\infty$ . The resulting system is a block pentadiagonal matrix system containing terms in both  $\alpha$  and  $\alpha^2$ . Using the initial guess provided by the global method, iterations are performed on  $\alpha$  using the secant method until  $\hat{V}_{x,j=1}^n$  is reduced to zero. This results in the complex wavenumber  $\alpha$  and the disturbance eigenfunction  $\psi$  at the starting location.

The PSE are solved using the method of Herbert [13]. The variables  $\alpha$  and  $\psi$  are updated simultaneously at each marching step. The boundary conditions of LST are used, but without the normalization of  $\rho$ . The disturbance kinetic energy is used to

normalize the integrals used in the wavenumber updates. Iterations are performed until the wavenumber has converged to within some tolerance, and that solution is used as the starting guess for the next marching station. Further details of the PSE solution procedure implemented in PSE-Chem are given in Reference [23].

Transition prediction is accomplished using the  $e^N$  method. The value  $e^N$ , where  $N$  is given by Equation 2.10, represents the total growth factor of a small amplitude initial disturbance.

$$N = \int_{\xi_0}^{\xi} \sigma d\xi \quad (2.10)$$

For the PSE, the disturbance growth rate  $\sigma$  is obtained from Equations 2.11 and 2.12. Here the domain of integration,  $\Omega$ , extends in the body-normal direction from the surface to the outer boundary.

$$\sigma = -\alpha_i + \frac{1}{2E} \frac{dE}{d\xi} \quad (2.11)$$

$$E = \int_{\Omega} \bar{\rho}(|\hat{u}|^2 + |\hat{v}|^2 + |\hat{w}|^2) d\xi \quad (2.12)$$

This differs from LST, where only the contribution of  $-\alpha_i$  is used to calculate  $N$  factors, as opposed to including the change in the disturbance shape factor. The disturbance kinetic energy is only one option available for calculating the amplitude. Johnson [26] showed that the use of the massflux can produce slightly different results, but the ability to perform the calculations either way is useful for comparisons with other results.

Mack [12] showed that the disturbances with the form given in Equation 2.3 can have several modes. The first mode is analogous to the Tollmien-Schlichting waves of incompressible flow. It is damped by wall cooling and is most amplified when it is at an oblique angle. The second mode can be thought of as a trapped acoustical wave. It is amplified by wall cooling, and it is most amplified when it is 2D. Higher modes exist, but they always have lower amplification rates than the first or second mode. Only the first and second modes will be considered in this thesis.

The stability solver uses a different grid than the mean flow solver. Before beginning the global, local, and PSE marching steps, the mean flow solution at each



streamwise location is linearly interpolated onto a grid with parameters specified in the PSE-Chem input file. This grid can have standard hyperbolic or exponential stretching, or it can cluster points at both the wall and edge using either hyperbolic or cosine-exponential stretching. This interpolation will slightly decrease the accuracy of the mean-flow variables, but the effect of this change was not examined. No significant difference was found in the results obtained with the various available stretching methods.

PSE-Chem is designed for parallel processing using the MPI message passing libraries. The global solution procedure divides the frequencies to be searched among the available processors. The local procedure divides the guesses to be refined for a given frequency among the processors. The linear PSE marching does not parallelize as well, but this step is normally much faster than the global or local steps.

The majority of the results presented in this thesis were obtained using Perl scripts to automatically run many cases sequentially, label the cases logically, and save the relevant results. Appendix A gives an example of a script to calculate  $N$  factors for combinations of starting location,  $\omega$ , and  $\beta$ . These scripts use functions from the scripting library recently added to STABL. This is a powerful and robust methodology, but it is inefficient. The computations performed for this thesis generally used a wide, but fairly coarse, band of parameters. This ensured that the most unstable modes were captured, but the resolution near the most unstable modes was not always as good as desired. To increase the resolution with this system without resulting in an unreasonable number of cases would require either better knowledge of the expected results to reduce the parameter bandwidth or the development of some sort of adaptive refinement algorithm. With the current system, the best solution would probably be to run a wide, coarse parameter matrix, analyze the results, and then run a second set of cases with a finer parameter matrix centered on the critical modes.

### 2.3 Equipment Used

The computations described in this thesis were performed on one of two systems. A Dell Precision 650 workstation with two 3.06 GHz Intel Xeon processors and 2 GB of RAM was used for some of the computations and all of the post-processing. In addition, access to the ‘Rogue’ Beowulf cluster was provided by Sandia National Laboratories. This cluster has 247 nodes with two 3.06 GHz Intel Xeon processors on each node, connected by 2 Gb/s Myrinet connections, and 160 nodes with two 2.4 GHz Intel Xeon processors on each node, connected by 100 Mb/s Ethernet connections. All nodes on Rogue had 2 GB of RAM. Both the local workstation and Rogue used the Red Hat 9 Linux operating system. The workstation had a 2.4.20-31.9smp kernel, and Rogue had a 2.4.20-30.9smp kernel with GPFS patches applied. The codes were compiled using the Portland Group `pgf90` and `pgcc` compilers. Message passing was accomplished using the MPICH MPI libraries.

Both mean flow and stability calculations were performed on both systems. No significant difference was seen between the results on either system. Solutions with 150,000 cells, which were typical of the size used in this thesis, could be obtained in approximately four hours on sixteen processors, and the solution time scaled approximately linearly with the number of processors. The residual typically dropped by 12–14 orders of magnitude. If necessary, the computational time required could be significantly decreased by freezing the solution and increasing the CFL number more aggressively. The global and local solutions each took approximately one minute per frequency per processor. The time required for sweeps over multiple combinations of starting location, frequency, and spanwise wavenumber, as shown in Chapter 4, was approximately 16 hours on two 2.4 GHz processors. A more advanced script using an adaptive refinement scheme could significantly decrease the run time if necessary.

Appendix B provides a detailed description of the methods of operation used for STABL as well as the lessons learned along the way.

### 3. Second Mode Verification: Stetson’s Blunt Cone

Chapters 3 and 4 will present the results of computations that were performed to verify and validate the ability of STABL to accurately compute instabilities and predict transition. All of the cases are for wind-tunnel conditions. Wind-tunnel cases were chosen for verification because a large body of previous computations exists and to match the general conditions of the Rufer wind-tunnel experiments, which have not been previously analyzed. The Rufer results will be presented in Chapter 5. Since it is not always possible to predict which is the dominant mode, computations for both the first and second modes were verified.

The second mode calculations in STABL were verified by benchmarking against other codes since accurate experimental data were not available for validation. This exercise uncovered a number of issues, including bugs, alternative algorithms, and different transport property models. These discoveries led to changes that improved the quality of STABL. However, this was not an ideal situation, as many of the details of the other calculations are unknown. The methods used are not identical, as STABL uses the PSE and is designed for chemically reacting flows, whereas all of the benchmark codes use LST for perfect gas air flows. In addition, unknown errors may exist in the various codes or their usage. These could account for the remaining differences in the results.

#### 3.1 Experimental Conditions

The conditions chosen for the exercise were those of the blunt cone experiments of Stetson et al. [33] with the 3.81 mm nose radius. Stetson performed hot-wire measurements in the boundary layer of a sphere-cone at  $0^\circ$  angle of attack and Mach 8 in Tunnel B at the Arnold Engineering and Development Center (AEDC). The test

Table 3.1: Test conditions for Stetson et al. [33] blunt cone experiment for all computations presented here.

Model Specifications	
Half angle	7°
Length (m)	1.016
Base diameter (m)	0.2495
Nose radius (mm)	3.81
Wall Temperature	Adiabatic
Freestream Conditions	
Fluid	Air
$M_\infty$	7.99
$p_o$ (Pa)	$4.0 \times 10^6$
$T_o$ (K)	750
$p_\infty$ (Pa)	410
$T_\infty$ (K)	54
$\rho_\infty$ (kg/m <sup>3</sup> )	0.0027
$Re_\infty$ /ft	$2.5 \times 10^6$

conditions for all Stetson computations in this thesis are summarized in Table 3.1. The freestream static temperature and density are required inputs for STABL, and they were calculated from the specified flow conditions using the isentropic relations and the perfect gas law. Further discussion of the input conditions will be given in Section 3.2.2.

The Stetson et al. experiment has been analyzed by numerous other researchers using many different codes, which makes it an ideal benchmark for wind-tunnel cases. All of the other researchers used LST-based codes for stability calculations, as opposed to the PSE used in STABL. Malik et al. [34] performed the first computations.

To compute the mean flow, they used a full Navier-Stokes solution for flow around a sphere to provide an initial data plane for a Parabolized Navier-Stokes (PNS) calculation on the cone frustum. Esfahanian [35] performed Thin-Layer Navier-Stokes calculations using very fine grid spacing by the standards of the day. Kufner et al. [36] performed a careful analysis of the sensitivity of the stability results to various assumptions made in computing the mean flow. Results obtained by Stilla using a second-order boundary-layer solver are included in Kufner et al. [36], as well as in Reference [37]. Rosenboom et al. [38] used Kufner's results as a basis for examining the effect of nose-tip bluntness on stability. More recently, Schneider [4, 39] performed a detailed reassessment of the Stetson experimental data and performed stability analyses using the mean flow generated by a boundary-layer solver. Esfahanian [40] performed additional computations using Stetson's conditions to test the accuracy of PNS mean flow solutions for stability applications. Lyttle et al. [41] used a DPLR solver to analyze Stetson's case with a particular emphasis on the wall temperature distribution. Zhong [42] performed LST calculations as part of an effort to analyze the flow using Direct Numerical Simulation.

Schneider [39] has shown that there are a number of open issues associated with this experiment. The axial station  $s/r_n = 175$  is used for the vast majority of the computations presented in the literature. However, Stetson's data show considerable nonlinearity at this station which will not be captured by a LST analysis. Overshoots are present in the pitot-pressure profiles, which are thought to be due to interference from the probe and have not appeared in any computation. Most researchers have assumed the wall is adiabatic, but the measured surface temperature is about 20% below the adiabatic temperature. The present work is not an attempt to resolve the discrepancies between computations and experiments. Rather, the intent is to replicate the computational results obtained with other codes to partially verify STABL. The large body of independent computational data makes this case ideal for verification, but these unresolved issues make complete validation from the experimental data impossible.

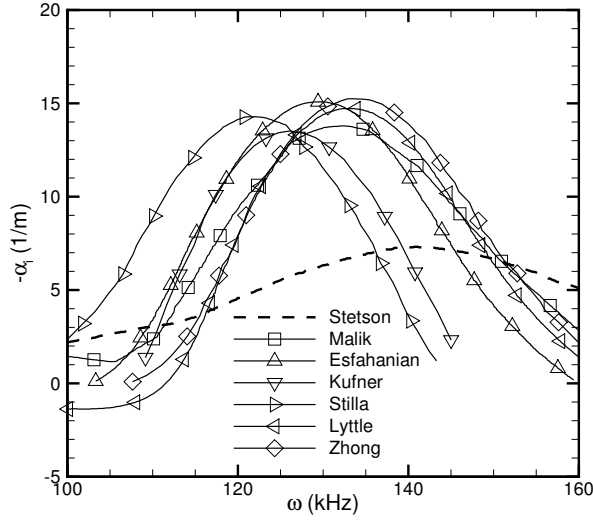


Figure 3.1: Amplification rate for Stetson's blunt cone at  $s/r_n = 175$  with  $r_n = 3.81$  mm as computed by other researchers. Symbols are for identification only.

Most of the researchers mentioned above published plots of the amplification rate at  $s/r_n = 175$ . Figure 3.1 shows these results on a single plot. The data was obtained by digitizing the figures in the references using the Un-Scan-It software package. The figures were electronically scanned to high resolution, and then the Un-Scan-It software was used to convert the graphical data to numerical data using an algorithm that interpolates based on the pixel coordinates of the line and the axes. The accuracy of the digitization is estimated to be on the order of the line width.

The computations in Figure 3.1 agree much better with each other than they do with the experimental data. This is most likely due to non-linearity and the other issues discussed above. The average peak amplification rate based on the six computations plotted is 14.4/m at a frequency of 129 kHz.

## 3.2 Issues Addressed

A number of issues were addressed to try to improve the agreement between the stability results of STABL and those of other researchers. Results incorporating the effects of the lessons learned from all of these issues are presented in Section 3.3. The following sections are intended to illustrate the incremental effect of each individual issue. Therefore, each section should be viewed as distinct from the others, rather than as a sequential progression of increasingly accurate solutions.

### 3.2.1 Laminar Transport Properties

The laminar transport properties are an essential component of any numerical model. These properties are the viscosity for momentum transport, the thermal conductivity for energy transport, and the diffusion coefficient for mass transport. Accepted models exist for usage within normal ranges of temperature and pressure. However, there is considerable subjectivity in determining the best model for very high or low temperatures, and the best choice for one extreme is generally not the best choice for the other. Lyttle and Reed [43] showed for high temperatures that the transport properties employed can have a large impact on hypersonic stability results.

The components of STABL were designed primarily for high enthalpy air flows, such as those found in hypersonic flight or in shock tunnels. These flows are characterized by extremely high temperatures, causing dissociation, ionization, and chemical and thermal non-equilibrium, phenomena known collectively as real-gas effects. Much more complicated flow models are required to accurately model these real gas effects than for situations where perfect gas behavior can be assumed.

Conventional hypersonic wind tunnels obtain high Mach numbers in part by lowering the static temperature in the test section to just above the condensation point of nitrogen. This lowers the speed of sound, creating hypersonic flow at lower freestream velocities than would be found in atmospheric flight at the same Mach

number [1]. Tunnel B at AEDC and the Purdue Mach-6 Ludwig Tube (M6LT) both have freestream static temperatures below 60 K for standard operating conditions. For slender bodies with highly oblique shocks, boundary-layer edge temperatures of 60–100 K are typical. For the STABL suite to be valid in the low enthalpy regime, transport property models appropriate to that regime must be employed.

All of the computations cited previously were performed with a Sutherland viscosity law. Not all of the references provide details about the thermal conductivity modeling, but those that did specify the method assumed a perfect gas with a constant Prandtl number. It is probable that those who did not specify their method used this technique as well. Because all of the computations in the literature treated the air as a single gas rather than a mixture, none included the effects of diffusion. Due to the low temperatures involved, the production of monatomic species is negligible. The binary diffusion model should therefore not be a significant factor, and its accuracy was not investigated.

## Viscosity

STABL originally used Blottner’s [44] viscosity model for reacting flows to determine individual species viscosities [23]. This model uses empirical curve fits of the form given by Equation 3.1 to compute individual viscosities in kg/m-s for each species in the mixture.

$$\mu_s = 0.1e^{(A_s \ln(T) + B_s) \ln(T) + C_s} \quad (3.1)$$

The viscosity of the mixture is found by Wilke’s semi-empirical mixing law, given in Equations 3.2–3.4.

$$\mu = \sum_{s=1}^{ns} \frac{X_s \mu_s}{\phi_s} \quad (3.2)$$

$$X_s = \frac{\frac{\rho_s}{M_s}}{\sum_{s=1}^{ns} \frac{\rho_s}{M_s}} \quad (3.3)$$



Table 3.2: Blottner's Viscosity Curve Fit Coefficients

Coefficient	High Temp	Low Temp
$A_{N_2}$	0.0268142	0.0089993
$B_{N_2}$	0.3177838	0.6039338
$C_{N_2}$	-11.3155513	-12.4453814
$A_{O_2}$	0.044929	-0.0255541
$B_{O_2}$	-0.0826158	1.0503525
$C_{O_2}$	-9.2019475	-13.7080219

$$\phi_s = \sum_{r=1}^{ns} X_s \frac{\left(1 + \left(\frac{M_r}{M_s}\right)^{1/4} \sqrt{\frac{\mu_s}{\mu_r}}\right)^2}{\sqrt{8\left(1 + \frac{M_s}{M_r}\right)}} \quad (3.4)$$

Two sets of the coefficients  $A_s$ ,  $B_s$ , and  $C_s$  are given in Table 3.2. The high temperature set was published in Blottner et al. [44] and is valid over the temperature range 1000 K–30000 K. The low temperature set represents unpublished data provided by Blottner (personal communication, October 2004) and is valid over the range 100 K–10000 K. Values for the species NO, N, and O are given in Reference [44] and are the same for both temperature ranges. These species have mass fractions many orders of magnitude below those of  $N_2$  and  $O_2$  at wind tunnel temperatures, and their viscosity modeling was not investigated.

The Sutherland law is the method most commonly used in CFD codes. This model is based on the kinetic theory of gases, and it is known to be a good approximation in the temperature range 100 K–2000 K [15]. Its form is given by Equation 3.5, where  $S$  is an effective temperature called the Sutherland constant and  $\mu_{ref}$  and  $T_{ref}$  are reference values [45].

$$\frac{\mu}{\mu_{ref}} = \left(\frac{T}{T_{ref}}\right)^{\frac{3}{2}} \frac{T_{ref} + S}{T + S} \quad (3.5)$$

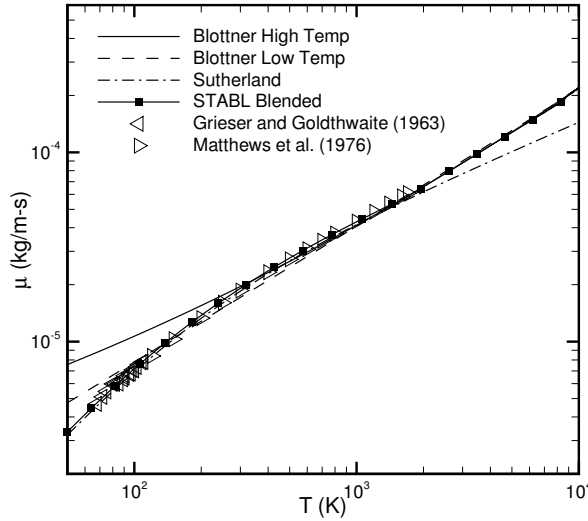


Figure 3.2: Viscosity of air computed using various methods compared with experimental data.

Figure 3.2 shows a comparison of the two methods given in Table 3.2 and the Sutherland law plotted with the experimental data of Grieser and Goldthwaite [46] and Matthews et al. [47]. Figure 3.3 shows a detail of the same plot at the low temperature limit. The viscosity reported by Grieser and Goldthwaite [46] near 50 K is two orders of magnitude smaller than the next closest value. This was based on one experimental measurement, and it illustrates the uncertainty that exists at very low temperatures. The Blottner high temperature model is seen to differ greatly from the experimental data at low temperatures. At 80 K, which is approximately the edge temperature for the Stetson case, the Blottner model overpredicts the viscosity by 70%. The Sutherland law diverges from the empirical models above approximately 1900 K, as is expected based on the approximations made in its derivation [45].

Based on this analysis, STABL was modified to incorporate different viscosity models for each temperature regime. STABL now uses the Sutherland law for low temperatures, the high-temperature Blottner law for high temperatures, and the low-

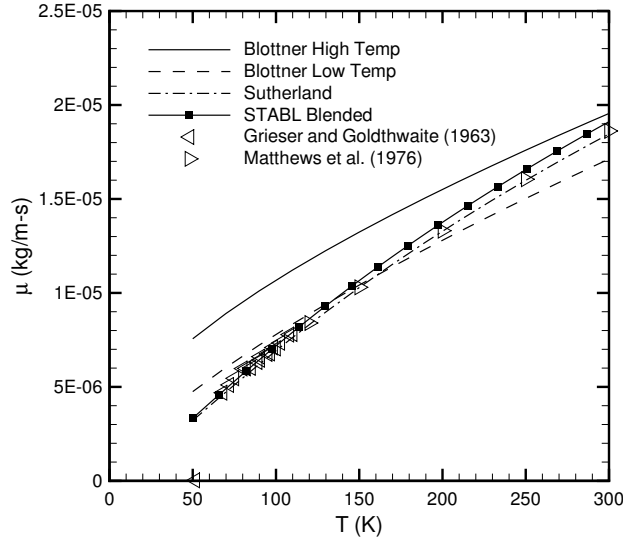


Figure 3.3: Viscosity models and experimental data for air at low temperatures.

temperature Blottner law for the intermediate range. Blending functions are used to ensure a smooth transition between the laws. The resulting method is shown as the STABL Blended curve in Figures 3.2 and 3.3. Agreement with the experimental data and the form of the Sutherland Law used in the other computations is considerably better.

It is important to note that there is considerably higher uncertainty in the experimental data below 200 K [48]. Several models exist for this low temperature regime. The Chapman-Enskog model [49] is based on the kinetic theory of gases and employs collision integrals to model the intermolecular forces. Keyes [50] and Maitland and Smith [51] both proposed empirical curve fits, and Mack [12] proposed a model hereafter referred to as the “Linear Sutherland Law” that is a linear extrapolation of the Sutherland Law below the Sutherland constant. Because the experimental data is so limited for this temperature range, there is no clear-cut choice for the best model. The Sutherland law was used for all computations in this work to provide consistency with the other computations referenced.

## Thermal Conductivity

STABL calculates thermal conductivities for both translational and vibrational modes [23]. It uses Eucken's relation, given in Equations 3.6–3.8, to calculate the translational thermal conductivity of each species.

$$k_s = \mu_s \left( \frac{5}{2} C_{v,tr_s} + C_{v,rot_s} \right) \quad (3.6)$$

$$C_{v,tr_s} = \frac{3R}{2M_s} \quad (3.7)$$

$$C_{v,rot_s} = \begin{cases} 0 & , \text{ monatomics} \\ \frac{R}{M_s} & , \text{ diatomics} \end{cases} \quad (3.8)$$

The vibrational thermal conductivity is given by Equation 3.9.

$$k_{vib_s} = \mu_s C_{v,vib_s} = \mu_s \frac{de_{v_s}}{dT_v} \quad (3.9)$$

The mixture thermal conductivities are computed with Wilke's semi-empirical mixing law, where  $k_s$  is substituted for  $\mu_s$  in Equation 3.2 and Equations 3.3 and 3.4 are unchanged.

The other researchers that have computed Stetson's blunt cone case have used perfect gas codes. Those that did specify their thermal conductivity method used a constant Prandtl number of 0.72, calculated the viscosity using Sutherland's law, assumed a constant  $C_p$ , and calculated the thermal conductivity from Equation 3.10.

$$Pr \equiv \frac{\mu C_p}{k} \quad (3.10)$$

Figure 3.4 shows the variation with temperature of Prandtl number and specific heat at constant pressure, for air. Data of Keyes [52] is plotted along with the values used by STABL. STABL uses a  $C_p$  that is constant with respect to temperature for a given gas mixture. The value shown was that calculated by the Flow Analysis module of the GUI for a mixture of 0.767 N<sub>2</sub> and 0.233 O<sub>2</sub>. The Prandtl number was calculated using Equation 3.10 with the value of  $C_p$  shown in Figure 3.4 and viscosity and thermal conductivity calculated using the blended model. The experimental

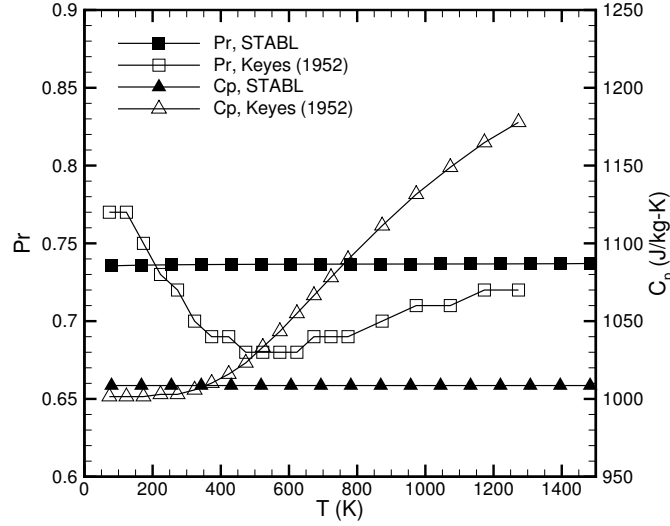


Figure 3.4: Temperature variation of Prandtl number and specific heat at constant pressure for air. Data is taken from Keyes [52].

Prandtl number varies from 0.77 at 100 K to 0.68 at 500 K, a range of 12% within the temperature span of the Stetson flowfield. The specific heat is reasonably constant at low temperatures, but it too begins to vary considerably, differing from the assumed constant value by 8% at 750 K. This shows that the common assumptions of constant  $C_p$  and  $Pr$  have relatively large errors, even for this temperature range. The impact of these assumptions on the stability results should be examined.

Figure 3.5 shows a comparison of the thermal conductivity as computed by STABL and as computed using a constant Prandtl number of 0.72. The curve marked “STABL Original” uses the Blottner high temperature viscosity model, the curve marked “STABL Blended” uses the blended viscosity model described earlier, and the constant Prandtl number curve uses a Sutherland Law. Experimental data of Taylor and Johnston [53], Keyes [52], and Vines [54] are also presented. Figure 3.6 shows a detail of the same plot for the low temperature regime. The STABL blended method agrees very well at low temperatures with both the experimental data and

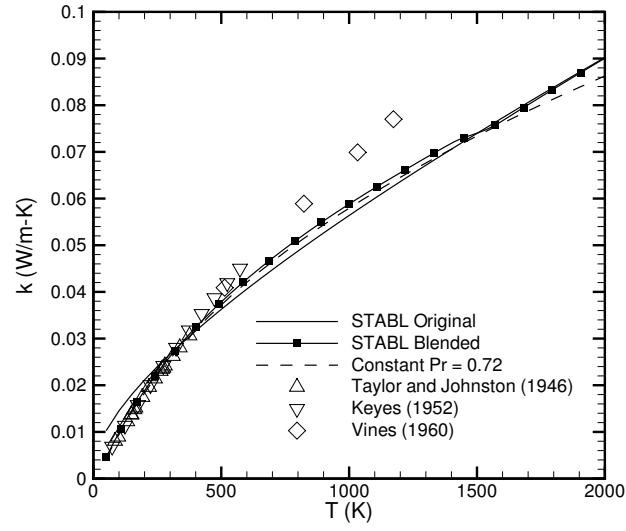


Figure 3.5: Thermal conductivity for air computed using various methods compared with experimental data.

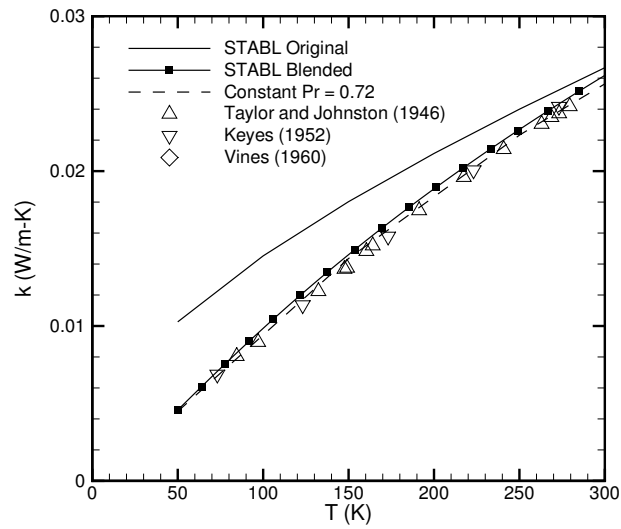


Figure 3.6: Thermal conductivity models and experimental data at low temperatures.

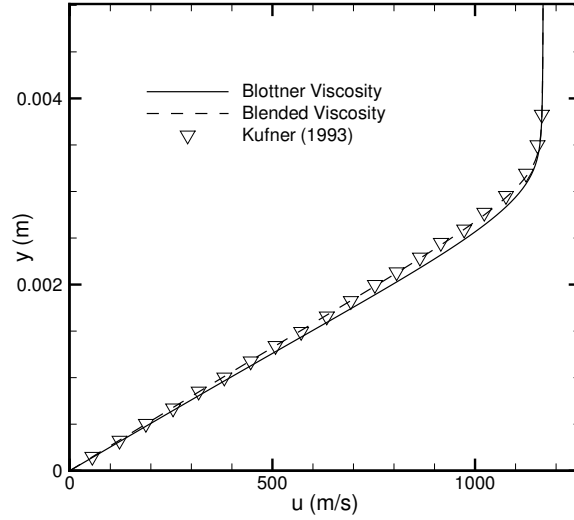


Figure 3.7: Velocity profile for Stetson's blunt cone at  $s/r_n = 175$  with  $r_n = 3.81$  mm with original viscosity model and new blended model.

the constant Prandtl number method. The use of the blended viscosity law causes the error in the calculated thermal conductivity with respect to the experimental data to drop from 70% to 4% at 80 K. However, all three of the methods differ significantly from the experimental data at higher temperatures. This may be due to the importance of the vibrational energy mode at higher temperatures, but this was not investigated further. Given the close agreement at high temperatures between the constant Prandtl number method and that used by STABL, this difference with the experimental data should not be a source of difference between STABL and the computational results of other researchers. However, it could have an impact on the accuracy of actual stability predictions.

## Effects

Figure 3.7 shows the effect of the change in the viscosity model on the boundary-layer profile at  $s/r_n = 175$ . The blended viscosity model makes the velocity profile

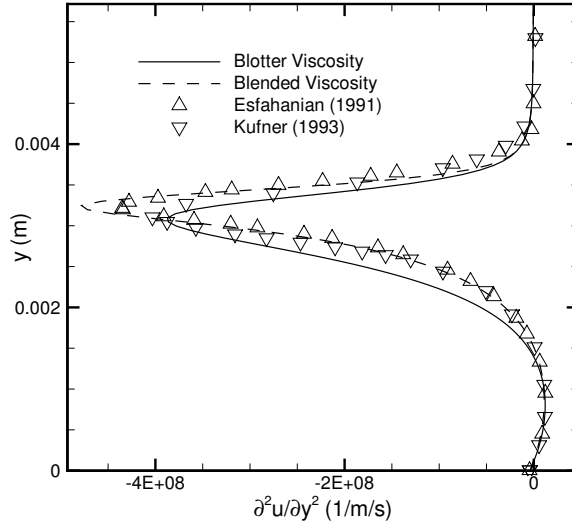


Figure 3.8: Second derivative of the velocity in the normal direction for Stetson's blunt cone at  $s/r_n = 175$  with  $r_n = 3.81$  mm with the original and blended viscosity models.

less full, and the agreement with the data of Kufner et al. [36] improves considerably. Figure 3.8 shows the effect of the viscosity model on the second derivative of the tangential velocity in the body-normal direction. The shape of the profile agrees much better with the data of Kufner et al. and Esfahanian [35]. The blended viscosity law causes the magnitude of the peak of the second derivative curve to increase by 23%, and it becomes larger than that of Kufner or Esfahanian. In addition, although agreement is improved near the boundary-layer edge, there are still small differences in the profiles in this region critical for stability.

Figure 3.9 shows the effect of the viscosity model on the amplification rate. The amplification curve peak is shifted from  $(\omega \text{ kHz}, -\alpha_i \text{ 1/m}) = (136, 13.4)$  to  $(132, 17.3)$ , which is an increase in the peak amplification rate of 29% and a decrease of 3% in the frequency at which that occurs. The decrease in the frequency causes better



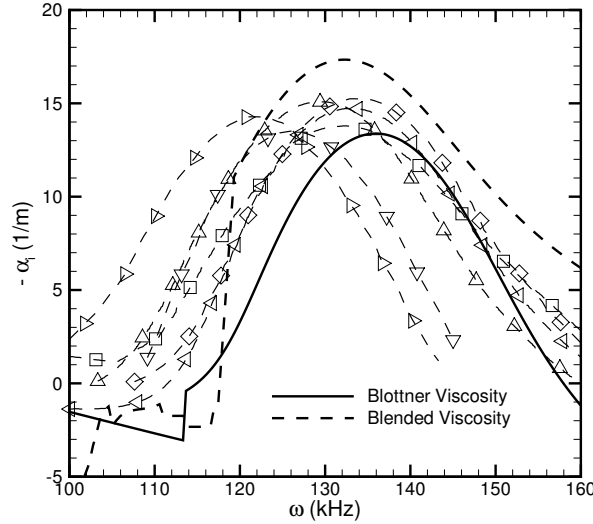


Figure 3.9: Amplification rate with the original and blended viscosity models for Stetson's blunt cone at  $s/r_n = 175$  with  $r_n = 3.81$  mm.

agreement with the other researchers, but the increase in the amplification rate causes worse agreement.

### 3.2.2 Input Conditions

In Reference [33], Stetson et al. specify the quantities  $M_\infty$ ,  $P_o$ ,  $T_o$ ,  $P_\infty$ , and unit Reynolds number. Discussions with Wayne Hawkins of AEDC (personal communication, July 2005) illustrated how these numbers were obtained. The stagnation pressure and temperature were measured directly in the stilling chamber. The Mach number was inferred from pitot measurements. The freestream static quantities were computed using a Beattie-Bridgeman correction to account for real gas effects, which was less than a 1% correction at these conditions. The unit Reynolds number is a derived quantity that depends on the viscosity model, which can be a source of uncertainty at the freestream temperature of 54.4 K. Table 3.3 shows a comparison of the unit Reynolds number calculated using different viscosity laws in common use

Table 3.3: Unit Reynolds number for the Stetson et al. blunt cone experiment calculated using various viscosity models.

Viscosity Model	$\mu \left( \frac{kg}{m-s} \right)$	$Re_{\infty}/ft$
Sutherland	$3.546 \times 10^{-6}$	$2.69 \times 10^6$
Linear Sutherland	$3.771 \times 10^{-6}$	$2.53 \times 10^6$
Keyes	$3.893 \times 10^{-6}$	$2.45 \times 10^6$
Chapman-Enskog	$3.788 \times 10^{-6}$	$2.53 \times 10^6$

for the low temperature regime. Stetson (personal communication, July 2005) stated that he obtained the freestream conditions from AEDC. Hawkins confirmed that the unit Reynolds number was calculated using a linear Sutherland law.

If the unit Reynolds number is used to determine the freestream conditions, the conditions will depend on the viscosity model used. All of the other researchers employed a standard Sutherland law for their computations, and the unit Reynolds number is an input condition for many CFD codes. To truly match the freestream conditions of Stetson’s experiment using a Sutherland law code, a unit Reynolds number of  $2.69 \times 10^6/ft$  would need to be used, rather than the  $2.50 \times 10^6/ft$  specified in Reference [33]. It seems likely that at least some of the other computations in the literature may have been performed using incorrect freestream conditions.

The STABL mean flow solver uses the freestream static temperature, freestream Mach number, and freestream static density as input conditions. The freestream static density is  $0.02652 \frac{kg}{m^3}$  when computed from the stagnation temperature and pressure using the perfect gas law and the isentropic relations. If a Sutherland viscosity law is used with a unit Reynolds number of  $2.50 \times 10^6/ft$ , the freestream density becomes  $0.02464 \frac{kg}{m^3}$ . The first value appears to be more physically accurate, and should be used for comparison with the experimental data. However, the second

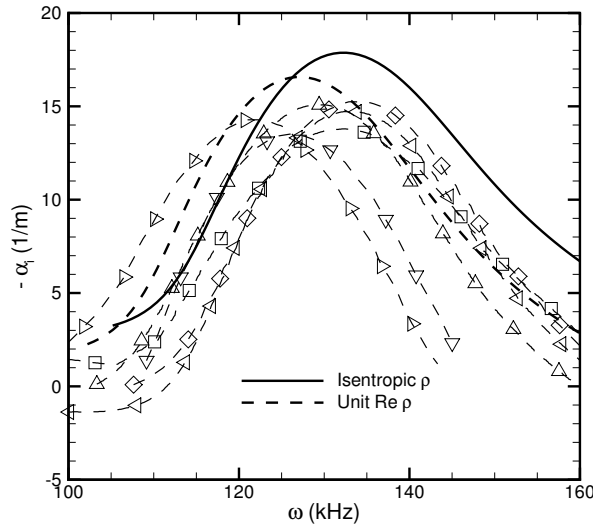


Figure 3.10: Amplification rates computed using two different values of freestream density for Stetson's blunt cone at  $s/r_n = 175$  with  $r_n = 3.81$  mm.

number is most likely what was actually used in the other researchers' computations, and thus it should be used for code verification with the current benchmarks.

Figure 3.10 shows the effect of changing the density input. Use of the value based on the unit Reynolds number shifts the amplification rate curve closer to the other researchers' results, moving the peak from (132,17.9) to (127,16.6). Figure 3.11 compares N factors for frequencies near 100 kHz calculated with each of the freestream density values. Despite the difference in the amplification rates, almost no difference is evident in the N factors.

A similar situation was described by Arnal et al. [55]. When they attempted to compute stability results independently by two groups, the use of two different viscosity models between the codes resulted in slightly different freestream conditions. Like the present results, this caused a small, but not negligible, difference in the amplification rate.

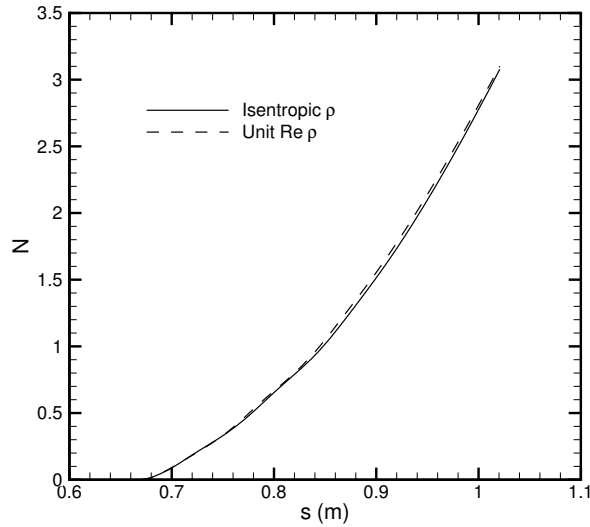


Figure 3.11: N factors computed using two different values of freestream density for Stetson’s blunt cone with  $r_n = 3.81$  mm.

### 3.2.3 Boundary-Layer Edge Detection

Many aspects of stability analysis depend on an accurate determination of the location of the boundary-layer edge. The most unstable first and second mode disturbances occur near the edge. For this reason, an accurate mean flow solution near the edge is vital, and PSE-Chem contains interpolation algorithms to structure the stability grid so that points are clustered at both the wall and edge. In addition, data presented in the literature is often presented in terms of edge quantities such as the Reynolds number  $R$ , but the edge velocity, temperature, and location are seldom specified.

Unfortunately, determining the location of the boundary-layer edge is not trivial. When the Prandtl number of the flow is not unity, the viscous and thermal boundary-layers will have different thicknesses. Valid arguments exist for using each to determine the “boundary-layer” thickness. In addition, a blunt body introduces an entropy layer that must be considered. Even if all of these factors are considered,

a parameter must be specified at which the local value is considered to be the edge. Choices of 95%, 99%, and 99.5% are all common in the literature.

For these reasons, STABL avoids the use of the edge location wherever possible. Since the full Navier-Stokes equations are solved over the entire shock layer, an edge parameter is not used in determining the mean flow. The edge location does matter in determining the grid for the stability analysis when edge clustering is employed. However, since this is an interpolation from the existing mean flow solution, the effect of small differences in the edge location will be minimal. The wave phase speed  $c_r$ , given by Equation 3.11, is used to classify instabilities based on their velocity relative to the edge. This requires an accurate determination of the edge location.

$$c_r = \frac{\omega}{\alpha_r U_e} \quad (3.11)$$

STABL uses the total enthalpy to determine the boundary-layer edge. For a Prandtl number less than unity, the thermal boundary layer will be thicker than the viscous boundary layer. In addition, the total enthalpy is constant outside of the thermal boundary layer, in contrast to velocity, which may vary outside of the viscous boundary layer due to pressure gradient effects.

It is possible for a flow to have an overshoot in its total enthalpy profile, as shown in Figure 3.12. This occurrence leads to three logical possibilities to declare as the boundary-layer edge, as indicated by the horizontal lines in Figure 3.12. The lowest line corresponds to the point where the total enthalpy first approaches the freestream value. The highest line is where the total enthalpy begins to stabilize at the freestream value. The middle line represents the peak of the overshoot, and could be seen as a compromise between the other options.

PSE-Chem originally used the lowest line as the boundary-layer edge. The outer line seems to be a much better choice, as shown by comparison with the mass flux profile plotted as the dashed line on Figure 3.12. Consequently, the PSE-Chem algorithm was modified to choose the outer line as the edge in the case of an overshoot; it still handle profiles without an overshoot correctly. A listing of the algorithm proposed by the author is given in Appendix C.

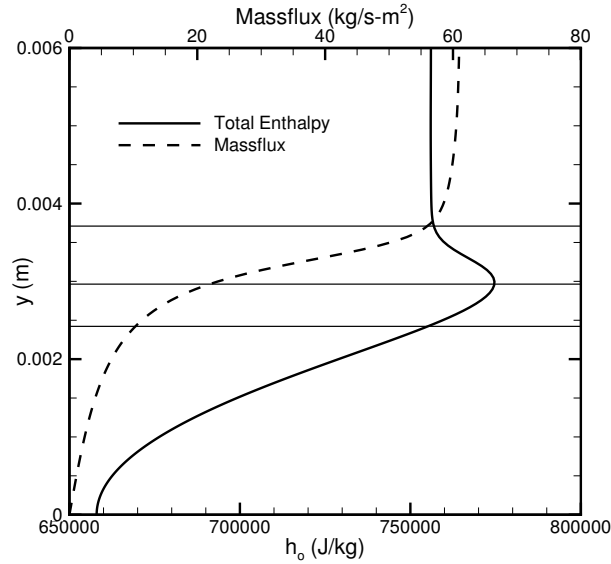


Figure 3.12: Representative total enthalpy and mass flux profiles.

### 3.2.4 Grid Generation

The requirement for accurate second derivatives of the velocity and temperature profiles throughout the boundary-layer means that much finer grids must be used for stability analysis than for most other CFD applications. Although results could sometimes be obtained with coarser grids, 80 points in the boundary layer was found to be an approximate minimum to obtain grid independent results. All of the results presented in this thesis were obtained with grids containing at least 300 axial points and at least 250 normal points.

Figure 3.13 shows the amplification curve computed for Stetson's blunt cone at  $s/r_n = 175$  with  $r_n = 3.81$  mm using several grids with varying resolution. The five curves shown used grids with 106, 121, 140, 239, and 276 points in the boundary layer. The points were clustered at the wall and exponentially stretched to the outer domain. The grids marked (b) in Figure 3.13 used an outer grid boundary that was very carefully constructed to match the shock shape over the entire length of the

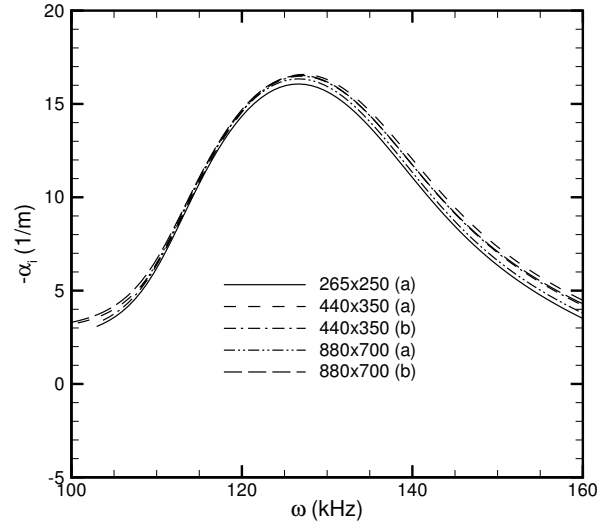


Figure 3.13: Amplification rate for Stetson's blunt cone at  $s/r_n = 175$  with  $r_n = 3.81$  mm computed using mean flows with varying grid resolutions.

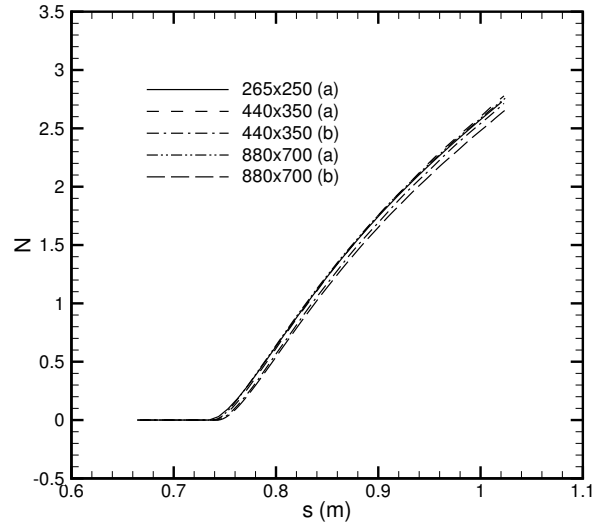


Figure 3.14: N factors computed using mean flows with varying grid resolutions for Stetson's blunt cone with  $r_n = 3.81$  mm.

cone. The grids marked (a) used a grid that matched the shape only reasonably well and is representative of the quality of grids used in most of the other computations shown in this thesis. Small differences between the grids are present, but no apparent trends are visible.

Figure 3.14 shows the  $N$  factors computed using each of the grids. Again, the differences are relatively small. The grids marked (b) produce slightly smaller  $N$  factors than the grids marked (a). There is no discernable trend with the total grid size. This suggests that the differences are due to the sensitivity of the stability calculations to small grid variations, and it cannot be conclusively said that one grid shape is better than the other. The scatter of approximately 5% at  $s = 1.0$  m may represent an uncertainty in the results that cannot be eliminated through increasing mesh density. In any case, the differences are slight compared with the overall uncertainty associated with the use of the  $e^N$  method, and sufficient mesh spacing is used for the present results.

### 3.2.5 Wall Temperature

Most previous computational comparisons to the Stetson experiment have assumed an adiabatic wall, but Schneider [4] showed that there was actually significant heat loss through the sting. Lyttle et al. [41] performed stability computations using both an adiabatic wall and wall temperature distribution similar to the experiment. They found a difference of approximately 15% in the peak amplification rate at  $s/r_n = 175$  m, but the difference did not explain the differences with the experimental amplification rates. All of the Stetson computations in this thesis were performed assuming an adiabatic wall for comparison with the other computations.

Lyttle et al. plot their calculated adiabatic wall temperature distribution in Figure 5 of Reference [41]. Figure 3.15 shows a comparison of Lyttle's distribution with that computed by STABL. A difference of about 5 K is evident along the frustum of



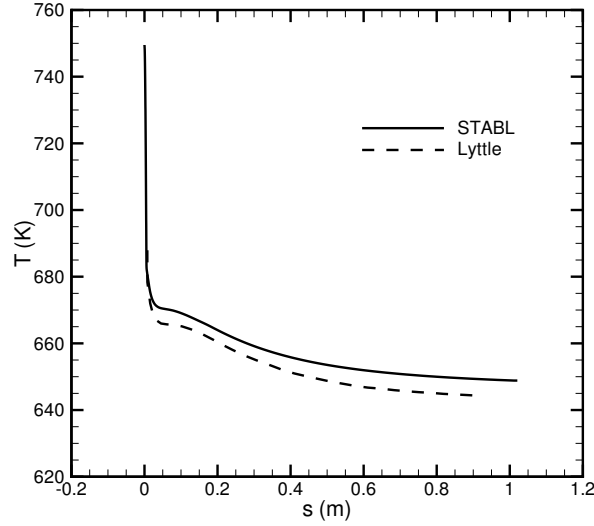


Figure 3.15: Surface temperature distribution for Stetson's blunt cone with  $r_n = 3.81$  mm as computed by STABL and by Lyttle et al. [41].

the cone. The reason for this difference is currently unknown, but it could be related to the differences in thermal conductivity shown in Figure 3.5.

A solution was obtained which used the wall temperature distribution computed by Lyttle as a fixed boundary condition, rather than the standard adiabatic wall condition. The adiabatic temperature distribution computed by STABL was used forward of  $s = 0.008$  m because accurate results could not be obtained from the plot in Reference [41]. Figure 3.16 shows the computed amplification rates using each mean flow solution. No significant differences are present in the local amplification. Figure 3.17 shows the N factors computed with each wall temperature distribution. The use of the Lyttle wall temperature distribution results in a slightly lower N factor than with the STABL calculated distribution, which is opposite the expected trend of a greater second-mode N factor for a colder wall. The difference appears to be in the critical location, as the local slopes of the two curves are the same.

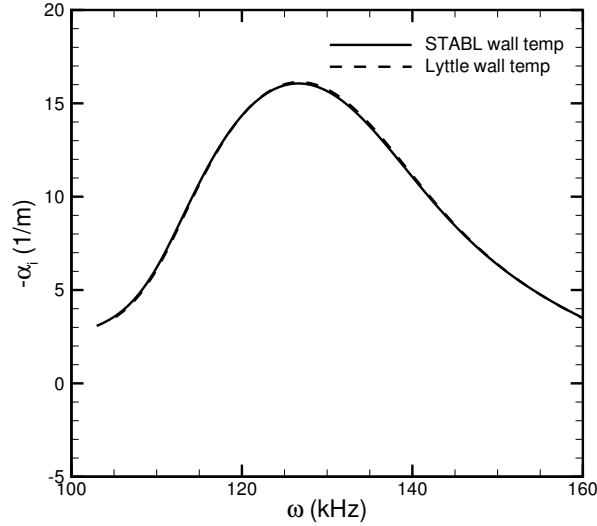


Figure 3.16: Amplification rate for Stetson’s blunt cone at  $s/r_n = 175$  with  $r_n = 3.81$  mm computed using mean flows with the surface temperature distributions calculated by Lytle and STABL.

### 3.2.6 STABL User Options

STABL has a number of options that a user can adjust to give more accurate results or to match the methods of another computation. Many combinations of various parameters were tested, and in all cases the effects on the stability results were found to be negligible. Figure 3.18 and Figure 3.19 show the effect on the amplification rate and N factor of changing two of these options. For the “without chemistry” line, chemical reactions and vibrational energy modeling were turned off. This is not expected to have a significant effect on the results for wind tunnel conditions. For the “reduced dissipation” line, the numerical dissipation parameters  $\varepsilon_i$  and  $\varepsilon_j$  in DPLR were halved. In all cases, the curves overlay each other completely, showing the independence of the solution with respect to these factors. The computational time was not significantly affected by either of these changes.

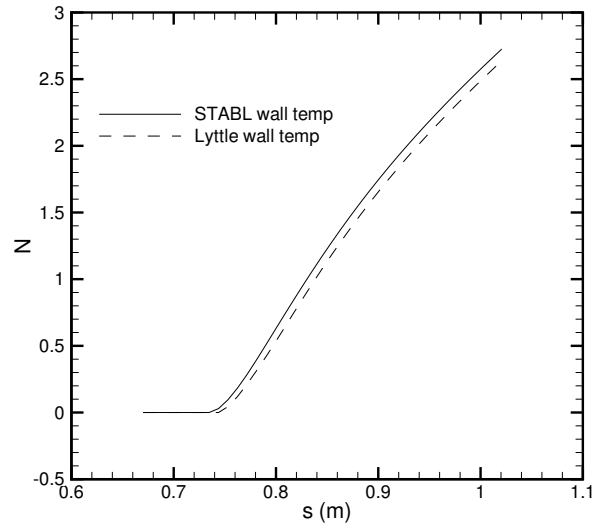


Figure 3.17: N factors for Stetson's blunt cone with  $r_n = 3.81$  mm computed using mean flows with the surface temperature distributions calculated by Lytle and STABL.

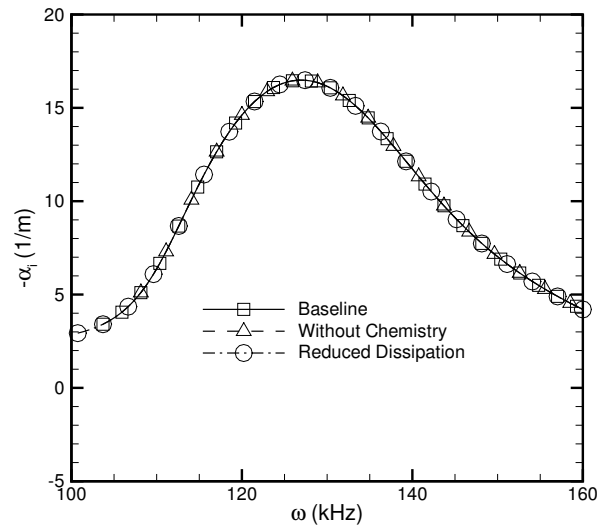


Figure 3.18: Amplification rate curves for Stetson's blunt cone at  $s/r_n = 175$  with  $r_n = 3.81$  mm computed using various user-specified options in STABL.

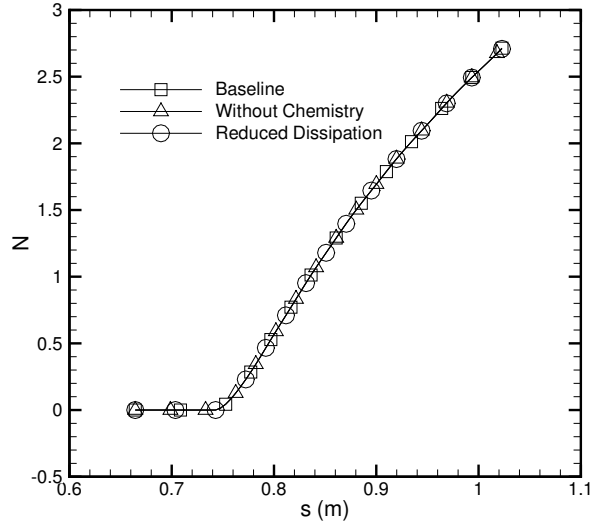


Figure 3.19: N factor curves for Stetson's blunt cone with  $r_n = 3.81$  mm computed using various user-specified options in STABL.

### 3.2.7 Freestream Thermal Non-Equilibrium

All of the other computations carried out in this chapter assume that the freestream flow is in thermal equilibrium. This is consistent with the other computations referenced, which were all performed with codes that do not consider any effect of the vibrational temperature.

Roy et al. [56] showed that the expansion rate in the Sandia National Laboratories hypersonic wind tunnel with the Mach 8 nozzle is much larger than the thermal relaxation rate, causing the vibrational temperature of the freestream flow in the test section to be frozen near the stagnation temperature. It seems likely that a similar situation could exist in AEDC's Tunnel B, which has a similar Mach number and slightly higher freestream stagnation temperature than the 633 K found in the Sandia tunnel. Bertolotti [57] showed that vibrational energy relaxation can have a significant effect on stability. He states that since the vibrational energy does not exceed 10% of the total internal energy of air until the flow stagnation temperature

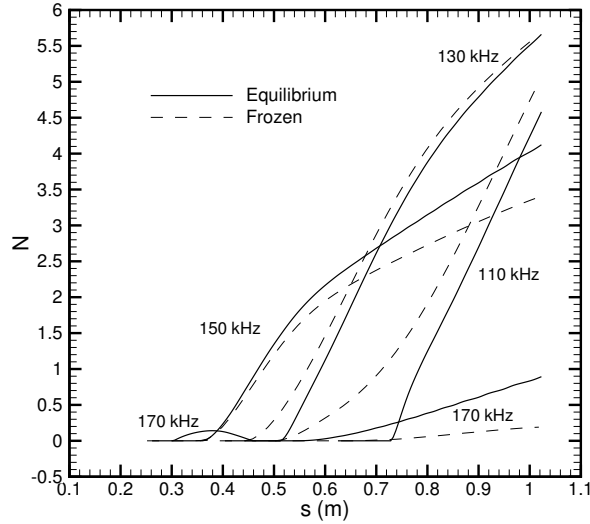


Figure 3.20: N factors calculated for Stetson's blunt cone with  $r_n = 3.81$  mm assuming both equilibrium and frozen thermal states.

surpasses 800 K, the degree of thermal nonequilibrium does not significantly impact stability below this temperature. Bertolotti does not present any computations for flows with stagnation temperatures below 1000 K.

Since stability results have been shown to be very sensitive to small changes in the mean flow, it seems likely that there could be some effect even at a stagnation temperature of 750 K. The degree of thermal nonequilibrium in Tunnel B was not calculated, but to gauge the maximum potential effects on stability, computations were performed with the freestream vibrational temperature set to the stagnation temperature. The true vibrational temperature should be somewhere between the stagnation temperature and the freestream static temperature, so these stability results and those for full equilibrium should bracket the results for the actual conditions.

Figure 3.20 shows a comparison of the N factors obtained when thermal equilibrium is assumed and when the vibrational temperature is frozen at the stagnation

temperature. Differences are evident in both the critical location for a given frequency and the growth rate, or slope of the curve. When the thermal state is frozen,  $N = 5.5$  is first reached by a 120 kHz mode (not shown on figure) at  $s = 0.959$ , which is 4% earlier than the location of  $s = 1.00$  obtained when thermal equilibrium is assumed. When the amplification rate at  $s/r_n = 175$  is plotted for both frozen and equilibrium flow, no difference is seen. This occurs despite the difference in slope evident in Figure 3.20 at both 150 and 170 kHz at that location,  $s = 0.67$  m. This suggests that the difference in slope might be caused by changes in the disturbance shape factor, which are included in a PSE analysis but not in a local LST calculation.

The effect on the amplification rates at  $s/r_n = 175$  is many orders of magnitude below the effect on the  $N$  factors. The reason for this is not currently known.

### 3.2.8 Normalization

All of the references cited present their amplification rates in non-dimensional form, but only Lyttle et al. [41] state the numerical values used in the normalization. The others all use the length scale given by Equation 3.12.

$$L = \sqrt{\frac{\nu_\infty s}{U_\infty}} \quad (3.12)$$

By default, PSE-Chem will output both dimensional amplification rates and those normalized by this length scale, but the value of the length scale depends on the viscosity model employed. Since there is no standard viscosity model for the freestream temperature, all of the figures in this thesis are presented in dimensional quantities to avoid confusion. The data digitized from the references was subsequently converted to dimensional form using the values provided for the Lyttle et al. data and Equation 3.12 for all of the others.

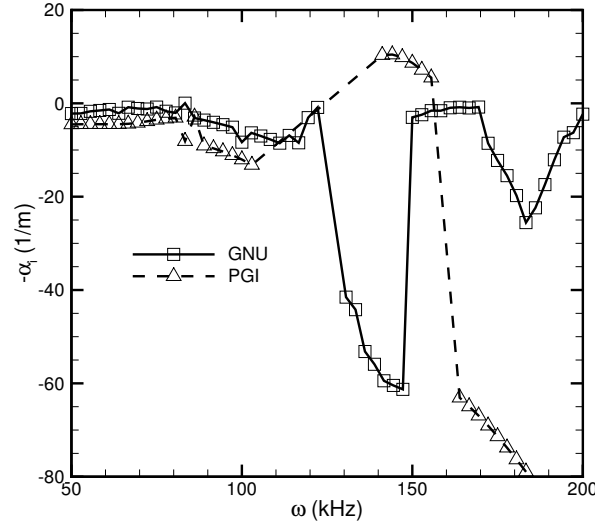


Figure 3.21: The effect of using different C and Fortran compilers on complex wave number for Stetson’s blunt cone at  $s/r_n = 175$  with  $r_n = 3.81$  mm.

### 3.2.9 Compilers

The C and Fortran compilers used to compile the STABL source code were at one time found to make a difference in the results obtained. The documentation states that STABL is compatible with either the GNU compilers `gcc` and `g77` or the Portland Group compilers `pgcc` and `pgf90` [26]. The GNU compilers were employed for the first eight months the code was used because of their ready availability on a Linux machine. Differences in the output obtained by the author and Heath Johnson using the same input files and source code led to a trial of the Portland Group compilers. This was found to have a significant effect, as illustrated in Figure 3.21, which shows the different results obtained with each set of compilers. In other cases, using the GNU compilers caused PSE-Chem to crash without producing any results at all. These problems were not encountered with the Portland Group compilers.

The discrepancy between the compilers appears to have been caused by a bug in the PSE-Chem source code that was recognized and avoided by the Portland Group

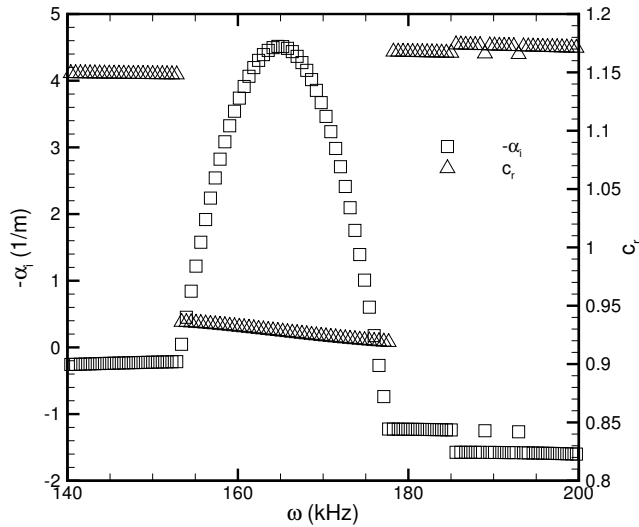


Figure 3.22: Amplification curve for Stetson's blunt cone with  $r_n = 3.81$  mm at  $s = 0.3$  m showing the existence of multiple families of solutions with different phase speeds.

compilers but that caused failure in the less sophisticated GNU compilers. That bug has since been fixed, and others have subsequently used the GNU compilers without incident. However, this is an example of the importance of code verification. If the same conditions had not been run by multiple users on multiple machines using different configurations, the bug may have gone unnoticed indefinitely.

### 3.2.10 Numerical Behavior

As described in Section 2, the global solution procedure produces a spectrum of approximate eigenvalues, and the local procedure iterates those guesses to the converged solution. For the Stetson et al. conditions, and presumably others, there exist many solutions for each frequency, and different guesses will converge to different solutions. To determine the complex wavenumber of the second mode, the local solver must analyze a guess that converges to that most unstable solution. The



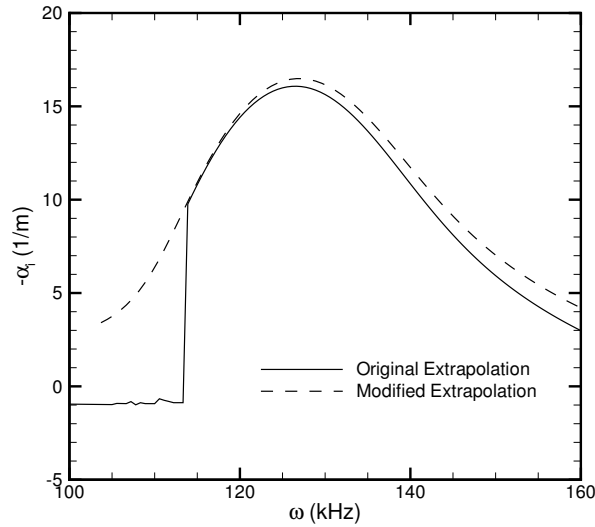


Figure 3.23: Amplification curves for Stetson's blunt cone at  $s/r_n = 175$  with  $r_n = 3.81$  mm obtained with the original extrapolation routine and with the modified extrapolation routine.

solutions can be differentiated by their phase speeds. The second mode typically had phase speeds in the range of 0.90–0.95, whereas the other solutions would have phase speeds greater than 1.0. Mack shows schematic diagrams of the different families of solutions in Figures 1 and 2 of Reference [58]. An example of the different families of results for the Stetson case at  $s/r_n = 175$  is shown in Figure 3.22.

Mack observes that the radius of convergence for the most unstable solution can be very small at hypersonic speeds, and that was observed in the present work. As an example, PSE-Chem gives the user the option to specify a wavenumber guess to the local solver. Even when the converged results of a previous local solution at the same frequency are fed back to the solver with five significant figures, often the new solution would converge to one of the damped families of solutions. PSE-Chem has options to extrapolate guesses for new frequencies based on converged solutions at neighboring frequencies. Based on results obtained by the author, the extrapolation

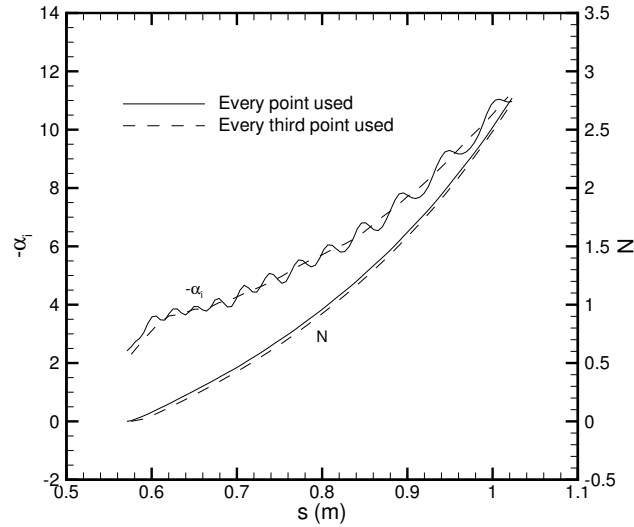


Figure 3.24: Spatial growth rate and N factor for Stetson's blunt cone with  $r_n = 3.81$  mm computed using different step sizes for the PSE marching procedure.

algorithm was changed to enable sweeps of both increasing and decreasing frequency, which helped to ensure that once the second mode family was found for one frequency it would be found for the rest of the range. Figure 3.23 shows the results obtained when the original extrapolation routine is used and when the new extrapolation routine is used.

Another numerical difficulty encountered during the solution process was an instability of the PSE marching procedure. Although the pressure gradient is modified in the PSE marching to suppress upstream disturbances [23], the solution can become unstable for small step sizes. In PSE-Chem, the problem manifested itself in oscillations in the spatial growth rate, as shown in Figure 3.24. PSE-Chem provides an option to the user to skip an integer number of axial stations during each marching step. This allows the user to specify a large number of axial points to obtain a more accurate mean flow without sacrificing the numerical stability of the PSE procedure.

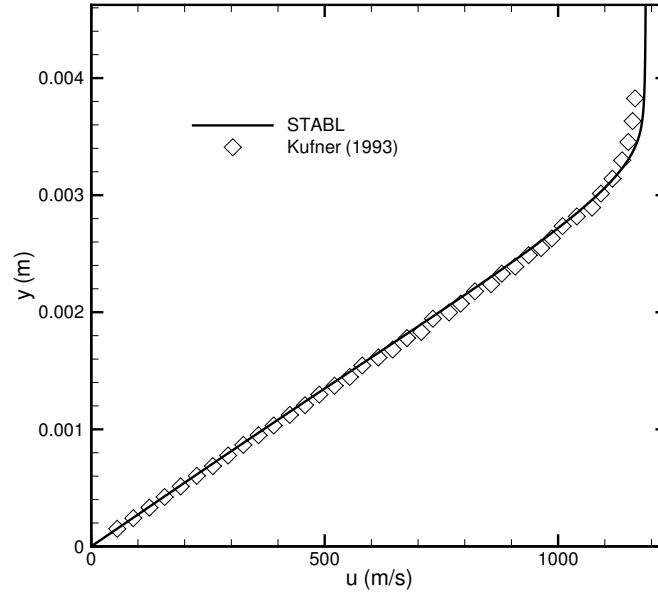


Figure 3.25: Mean velocity profile for conditions of Stetson et al. [33] at  $s/r_n = 175$  with  $r_n = 3.81$  mm compared with the results of Kufner et al. [36].

### 3.3 Computational Comparison

The mesh used for the final computation contained 440 axial points and 350 body-normal points, and it corresponds to the 440x350 (b) line in Figure 3.14. Chemical and thermal nonequilibrium effects were modeled, and a freestream air mixture with standard mass fractions of 76.7%  $N_2$  and 23.3%  $O_2$  was assumed. The freestream density was set to  $0.02464 \frac{kg}{m^3}$  to match the conditions thought to be used by the other researchers. Thermal equilibrium was assumed in the freestream. STABL version 1.26 was used for both the mean flow and the stability calculations.

Figure 3.25 shows the mean tangential flow velocity at  $s/r_n = 175$ . Data in Figure 1a of Kufner et al. [36] was digitized using the method described in Section 3.1 and is plotted on Figure 3.25 for comparison. Agreement is generally good, although there is a small difference near the edge of the boundary-layer. Figure 3.26 shows the second derivative of the velocity profile with respect to the body-normal distance at the same station. Data from Figure 1b in Reference [36] is also plotted. Again,

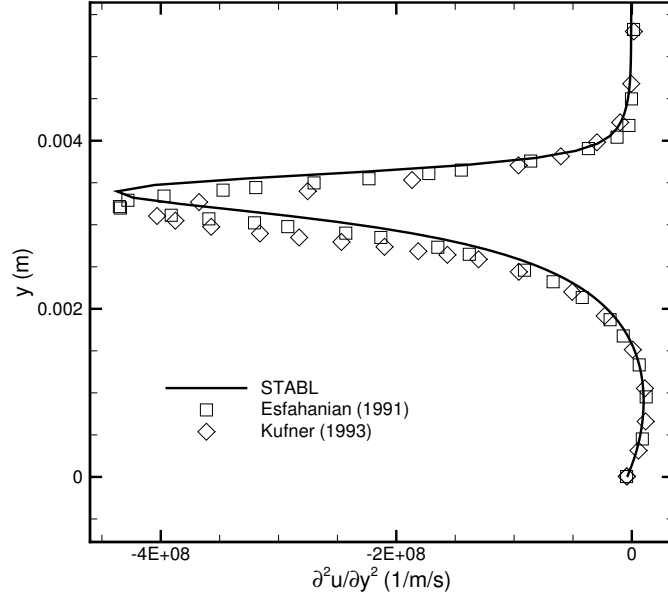


Figure 3.26: Second normal derivative of velocity profile for conditions of Stetson et al. [33] at  $s/r_n = 175$  with  $r_n = 3.81$  mm compared with the results of Kufner et al. [36] and Esfahanian [35].

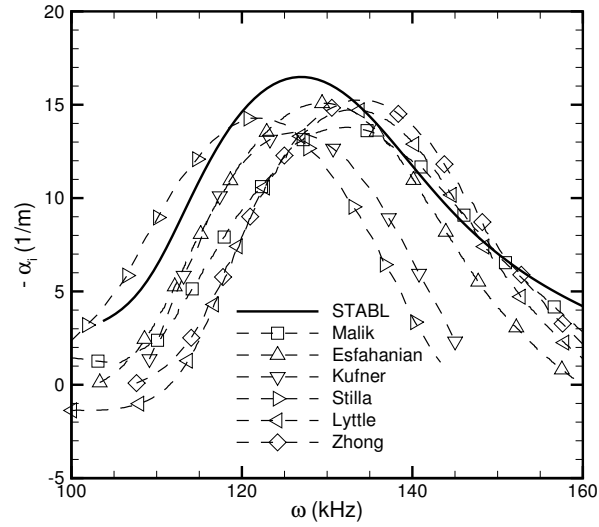


Figure 3.27: Amplification rate for conditions of Stetson et al. [33] at  $s/r_n = 175$  with  $r_n = 3.81$  mm.

Table 3.4: Location of the peak amplification as computed by STABL and several researchers.

Computation	$\omega$ (kHz)	$-\alpha_i$ (1/m)
STABL	127	16.5
Malik [34]	132	13.8
Esfahanian [35]	129	15.1
Kufner [36]	126	13.5
Stilla [36]	122	14.3
Lyttle [41]	133	14.7
Zhong [42]	134	15.2

agreement is good except near the boundary-layer edge. Because the instabilities arise near the boundary-layer edge, this difference could be significant.

Figure 3.27 shows the amplification curve at  $s/r_n = 175$  compared with that computed by other researchers. The peak frequency is slightly lower than the mean peak frequency, but it is within the scatter of the other results. The peak amplification rate is higher than any of the other researchers. The magnitude of the difference in the peak amplification rate is comparable to the scatter in the other results shown. Table 3.4 summarizes the location of the peaks in Figure 3.27.

As mentioned previously, most of the literature pertaining to the Stetson et al. experiment focuses on the  $s/r_n = 175$  axial station. Malik et al. present amplification rates for  $s/r_n = 215$  in Figure 15b of Reference [34]. Figure 3.28 shows a comparison of the amplification curve computed by STABL at that station with Malik's data. The level of agreement is consistent with the results presented in Figure 3.27, in that the peak computed by PSE-Chem is shifted up and to the left with respect to Malik's peak.

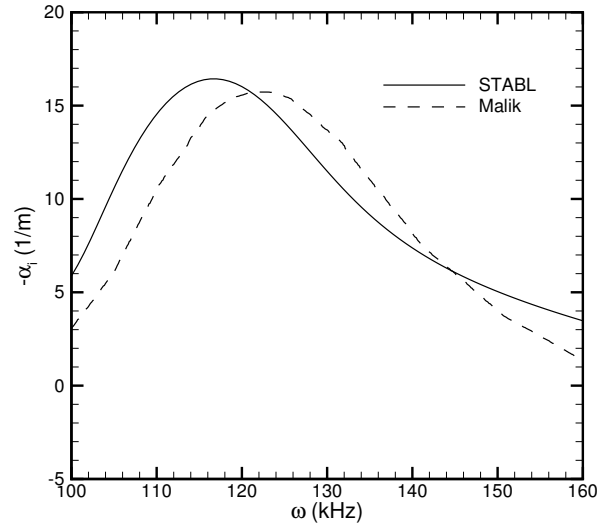


Figure 3.28: Amplification rate for Stetson's blunt cone with  $r_n = 3.81$  mm at  $s/r_n = 215$  compared with the data of Malik et al. [34].

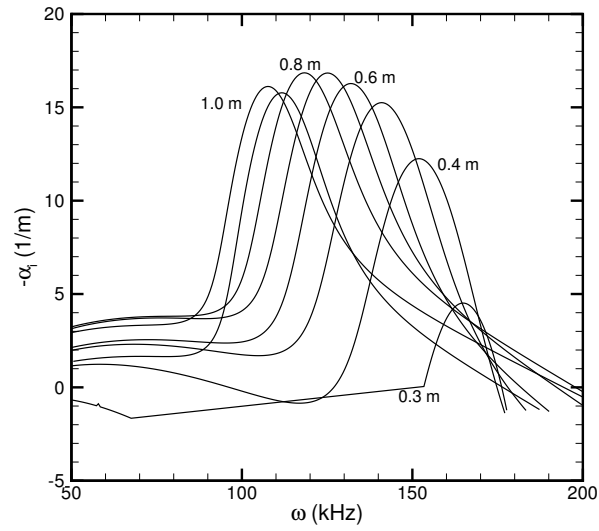


Figure 3.29: Amplification rate curves at axial locations ranging from  $s = 0.3$  m to  $s = 1.0$  m for Stetson's blunt cone with  $r_n = 3.81$  mm.

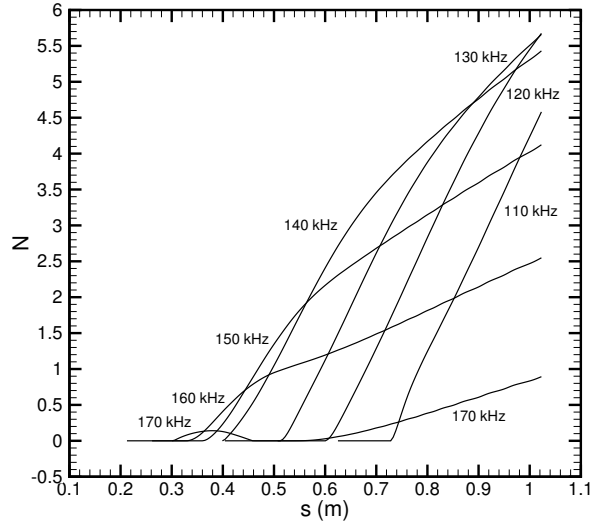


Figure 3.30: Maximum N factors obtained for various frequencies for Stetson's blunt cone with  $r_n = 3.81$  mm.

Figure 3.29 presents the local amplification rate computed at axial locations ranging from  $s = 0.3$  m to  $s = 1.0$  m. No amplification is found forward of  $s = 0.3$  m. The peak amplification grows from  $s = 0.3$  m to  $s = 0.5$  m and is nearly constant from  $s = 0.5$  m to the aft end of the cone. The most amplified frequency decreases as the axial distance increases. This is expected, given that the frequency is highly tuned to the boundary-layer thickness [59]. One interesting phenomenon is that for all locations from  $s = 0.4$  m aft, amplification occurs for frequencies below the primary second mode frequency. That amplification represents a 2-D first mode instability, and amplification in that frequency range is greater for oblique wave angles. The solution from 70–150 kHz at  $s = 0.3$  m represents one of the damped families of solutions described in Section 3.2.10. In this case, that solution is less stable than the second mode solution at those frequencies.

Figure 3.30 displays the maximum N factors obtained for various frequencies for Stetson's  $r_n = 3.81$  mm case. To obtain these N factors, a test matrix was con-

Table 3.5: Transition location predicted by STABL for Stetson et al. blunt cone case compared with that predicted by other researchers. Transition was assumed at  $N=5.5$  for all computations.

Computation	$s_{tr}$ (m)	$Re_{\infty, s_{tr}}$
STABL	1.00	$8.192 \times 10^6$
Esfahanian and Hejranfar PNS [40]	1.00	$8.21 \times 10^6$
Esfahanian and Hejranfar IPNS [40]	0.973	$7.98 \times 10^6$
Stilla [37]	0.956	$7.84 \times 10^6$
Malik et al. [34]	0.956	$7.84 \times 10^6$
Rosenboom et al. [38]	$> 1.0$	$> 8.2 \times 10^6$

structed consisting of all combinations of the starting locations  $s = 0.1, 0.15, \dots, 1.0$  m and frequencies  $\omega = 50, 60, \dots, 200$  kHz. PSE marching was conducted at each point in the test matrix, and the maximum  $N$  factors for each frequency are plotted in Figure 3.30. If, following the work of Malik et al. [34], Stilla [37], and Esfahanian and Hejranfar [40], transition is assumed to occur at  $N = 5.5$  in this noisy environment, STABL would predict transition at  $s = 1.00$  m with 130 kHz the most amplified frequency. Table 3.5 shows a comparison of the transition location predicted by STABL with that of the other researchers. The unit Reynolds number specified by Stetson et al. of  $2.50 \times 10^6/\text{ft}$  was used to convert between the  $Re_{\infty, s_{tr}}$  and  $s_{tr}$ . Agreement with the other researchers is better than 5%.

Figure 3.31 shows a comparison of the  $N$  factors computed by STABL with the local  $N$  factors computed by Rosenboom et al. [38]. Agreement in the location of amplification of the various frequencies is fair, with no clear trends evident. The STABL 140 kHz and 160 kHz lines show amplification throughout the full surface length, in contrast to the Rosenboom results, which begin to decay at  $s = 0.85$  and  $s = 0.55$  m, respectively. The STABL results are consistent with Figure 3.29, which



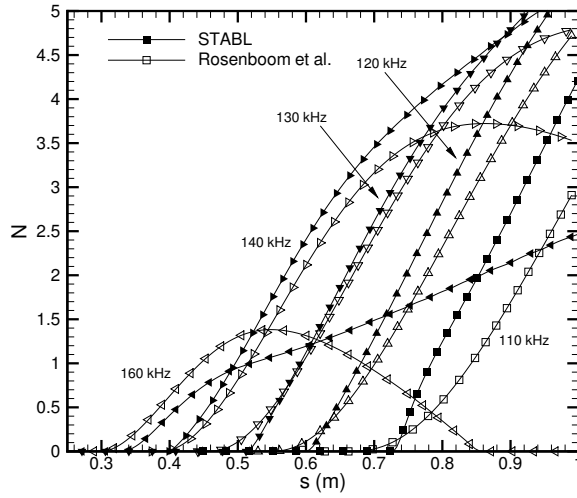


Figure 3.31: Comparison of  $N$  factors calculated by STABL with local  $N$  factors of Rosenboom et al. [38] for Stetson's blunt cone with  $r_n = 3.81$  mm.

shows all frequencies up to 180 kHz amplifying on the aft portion of the cone. The reason for the differences is not clear. Exact results for Rosenboom et al. are not given in Table 3.5 because the data do not extend beyond  $s = 1.00$  m or  $N = 5.0$ , so only lower bounds for the predicted transition location are given.

Figures 3.32 and 3.33 show the temperature and pressure eigenfunctions at the aft end of the cone. These are dimensional quantities obtained for an initial disturbance amplitude of 0.001 K or Pa. The shape of the curves is indicative of second mode disturbances, as shown by Johnson [23]. The pressure amplitude shows two peaks, which matches the results of Mack [12] for second mode waves. The pressure amplitude in Figure 3.32 does not cross zero because the amplitude is plotted, in contrast to Mack, who plotted the real component of the eigenfunction. The bump in the pressure amplitude and phase at  $y/\delta = 0.85$  is thought to be a numerical artifact, but it was not investigated.

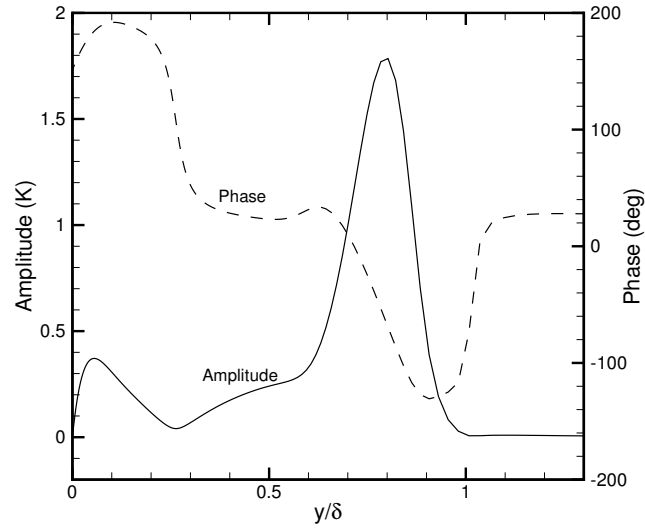


Figure 3.32: Amplitude and phase of the temperature eigenfunction at the aft end of the cone for Stetson's blunt cone with  $r_n = 3.81$  mm.

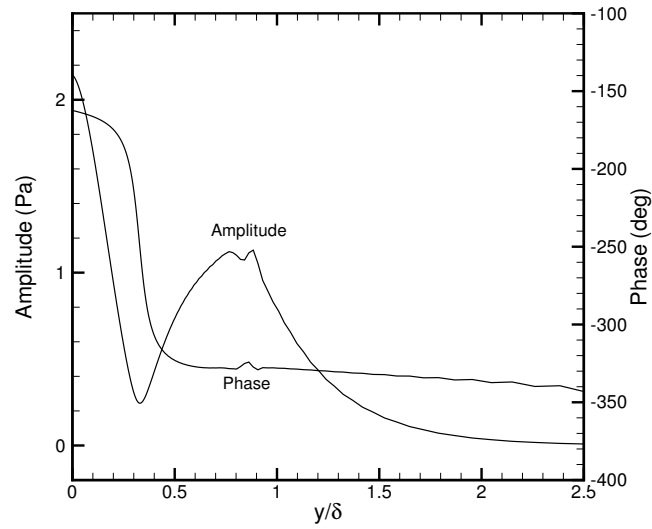


Figure 3.33: Amplitude and phase of the pressure eigenfunction at the aft end of the cone for Stetson's blunt cone with  $r_n = 3.81$  mm.

## 4. First-Mode Verification

Two cases were analyzed to verify STABL’s ability to correctly calculate first-mode disturbances. Since real hypersonic vehicles have some degree of bluntness to control stagnation-point heating, a blunt cone case was desired. However, no previously calculated blunt cone cases for which the first mode was dominant could be found. A low Mach number sharp cone was found that had been shown to be first mode dominant. In addition, a large-bluntness cone was found for which the first mode had a degree of amplification comparable to the second mode. Both cases will be discussed in this chapter.

### 4.1 Sharp Cone at Mach 3.5

#### 4.1.1 Experimental Conditions

A sharp cone was analyzed using the conditions shown in Table 4.1 to verify STABL’s ability to calculate first mode disturbances. The conditions correspond to experimental data obtained by Beckwith et al. [60] in the NASA Langley Mach 3.5 pilot quiet tunnel. This tunnel is designed to give freestream disturbance levels comparable to flight. The conditions chosen correspond to the fourth unit Reynolds number data set in Run 5 of Reference [60]. The first mode is expected to be dominant at this low freestream Mach number with an adiabatic wall.

This case was previously analyzed by Malik as case QT1 in Reference [61] using the COSAL stability code. This older LST-based code calculates temporal stability and uses Gaster’s group velocity transformation to obtain spatial stability results. The mean flow was obtained from a boundary-layer code and provided as an input to COSAL.

Table 4.1: Test conditions for sharp cone at Mach 3.5

Condition	Value
Cone half angle	5°
Cone length (m)	0.381
Wall temperature	Adiabatic
Fluid	Air
$M_\infty$	3.5
$p_o$ (kPa)	525
$T_o$ (K)	319.0
$T_\infty$ (K)	92.53
$\rho_\infty$ (kg/m <sup>3</sup> )	0.02592
$Re_\infty/m$	$2.74 \times 10^7$
$s_{tr}$ (m)	0.278

Roger Kimmel of the Air Force Research Laboratory (personal communication, March–April 2005) performed additional computations for this case using the  $e^{Malik}$  stability solver. This more recent code is also widely used for hypersonic stability analysis. Spatial stability results are calculated directly, and a perfect gas model is assumed. For the cases shown, the mean flow was provided by a similarity solver built into the  $e^{Malik}$  code. These computations were performed at the request of the author, and a good deal of collaboration and discussion with Dr. Kimmel occurred to troubleshoot differences between the results.

#### 4.1.2 Computational Comparison

A grid with 450 axial points and 350 normal points was used for the DPLR2D mean flow solution. Exponential stretching was used in both directions to cluster grid

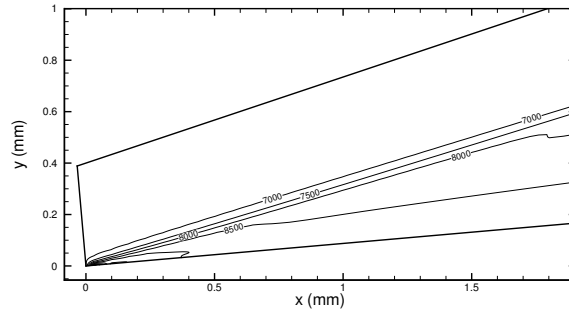


Figure 4.1: Lines of constant pressure at the nosetip for a sharp cone at Mach 3.5.

points near the cone tip. This clustering increased the number of points within the boundary-layer and reduced the degree of numerical error caused by the singularity at the nose. Figure 4.1 shows isobars for the first 0.5% of the cone length. The solution is valid very near the nose, despite the singularity caused by the sharp tip. The number of grid points within the boundary-layer varied from 148 near the nose tip to 109 at the base. Chemical and thermal nonequilibrium effects were modeled with thermal equilibrium assumed in the freestream, and the blended viscosity model was used for all calculations.

Figure 4.2 shows wall-tangential mean flow velocity profiles computed by STABL and  $e^{Malik}$  at three axial locations. The velocities computed by STABL are on the order of 10–20 m/s larger than those computed by  $e^{Malik}$  throughout the profile for all distances. Similar trends are seen in the temperature profiles, shown in Figure 4.3, with the differences being on the order of 5 K. These visible differences in the temperature and velocity can be expected to have a significant effect on the stability results. Meaningful second-derivative comparisons were not available due to the lack of precision in the output of the  $e^{Malik}$  similarity solution.

Linear stability calculations were performed at several axial locations. Figure 4.4 shows the amplification rate plotted as a function of both frequency and wave angle for six different axial locations. The contour plots shown were created by interpolat-

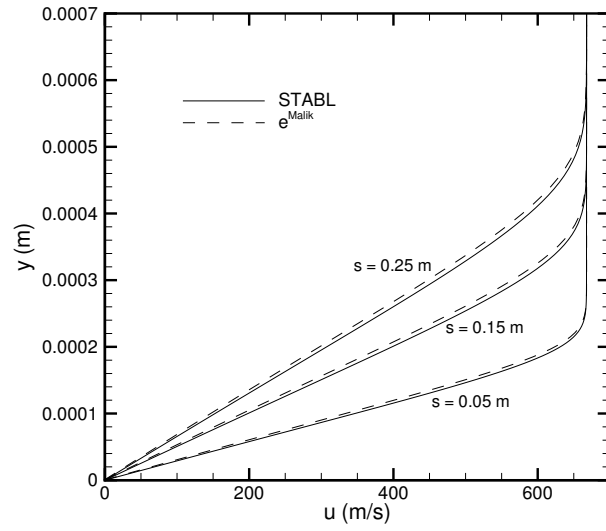


Figure 4.2: Mean flow velocity profiles for the sharp cone at Mach 3.5 at several axial locations.

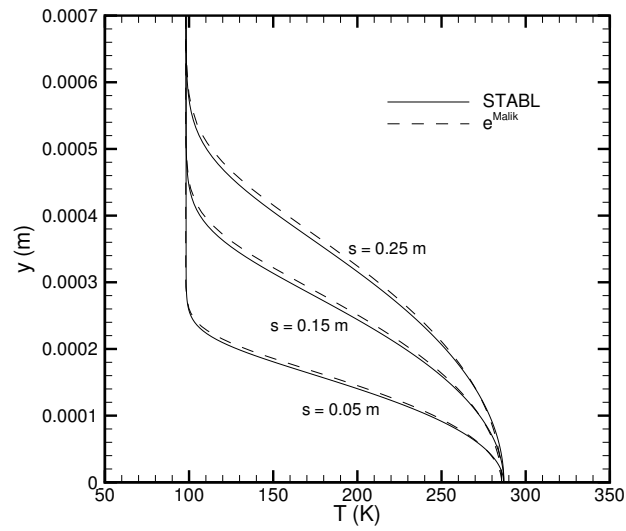


Figure 4.3: Mean flow temperature profiles for the sharp cone at Mach 3.5 at several axial locations.

ing between the results of twelve solutions at each location. Each of the individual solutions had a varying frequency but constant  $\beta$ . The constant dimensional spanwise wavenumber condition obeys the irrotationality condition on the wavenumber vector described by Mack [12, 58]. The wave angle was computed for every point using Equation 4.1.

$$\psi = \arctan \left( \frac{\beta_r}{\alpha_r} \right) \quad (4.1)$$

Several qualitative conclusions can be drawn from Figure 4.4. The most amplified frequency decreases as  $R$  increases. The maximum amplification rate also decreases as  $R$  increases, although that effect is not seen very near the nose. The wave angle of the most amplified mode increases from approximately  $60^\circ$  very near the nose to approximately  $70^\circ$  on the aft portion of the cone.

Several mean flow solutions using different numbers of grid points within the boundary-layer were analyzed to ensure grid-independence of the solution. Figure 4.5 shows the effect of the different grids on the  $N$  factor calculations. These calculations are for a mode at  $\omega = 104$  kHz and  $\beta = 2400/\text{m}$  with marching beginning at  $s = 0.0339$  m. Four of the solutions are very similar; the only difference is seen for the grid with 72 points in the boundary-layer. The reason for this repeatable difference is not clear. The grid with 109 points in the boundary-layer was used for all other calculations in this section.

To obtain the maximum  $N$  factors for this case, a test matrix was constructed consisting of  $\omega = 25, 50, \dots, 250$  kHz,  $\beta = 1000, 2000, \dots, 8000$  1/m, and starting location  $s = 0.02, 0.04, \dots, 0.12$  m. The modes producing the maximum  $N$  factors at each location are shown in Figure 4.6. Amplification began at  $s = 0.02$  m for the higher frequencies and shortly thereafter for the 75 kHz mode. At the experimental transition location of  $s = 0.278$  m, the most amplified mode has a frequency of 75 kHz, a  $\beta$  of 2000 1/m, a wave angle of  $64^\circ$ , and a  $N$  factor of 12.2. This  $N$  factor is larger than the range of 9–11 commonly calculated at experimentally measured transition locations in low disturbance environments. For comparison, the value of  $Re_\theta/M_e$  is 154 at the transition location, as shown in Figure 4.7.

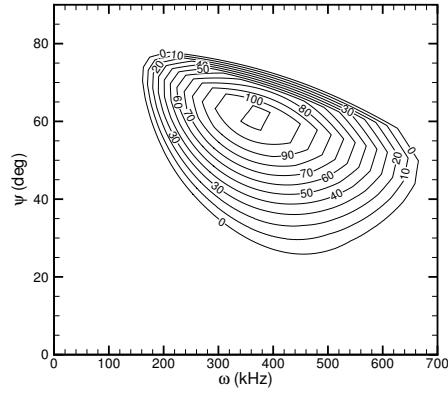
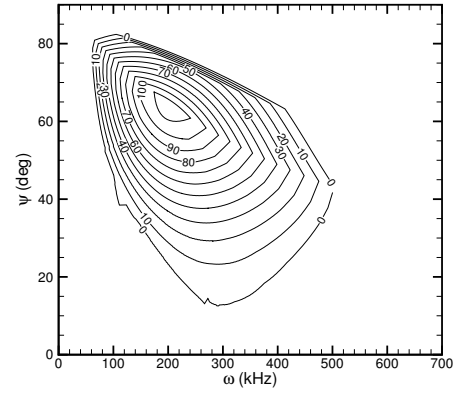
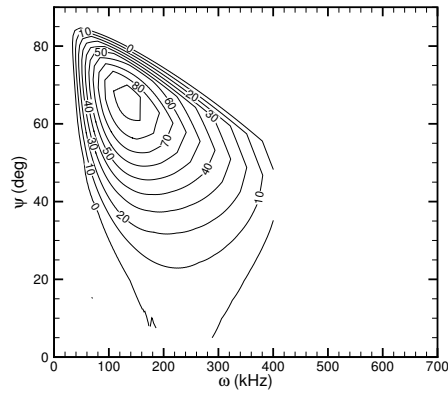
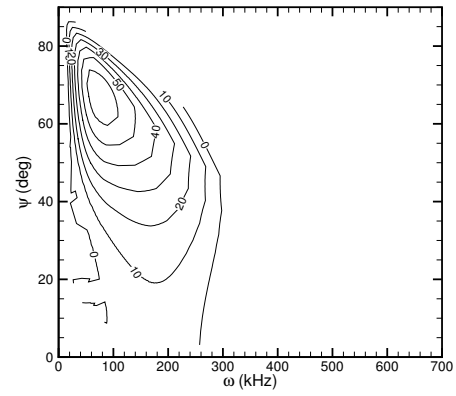
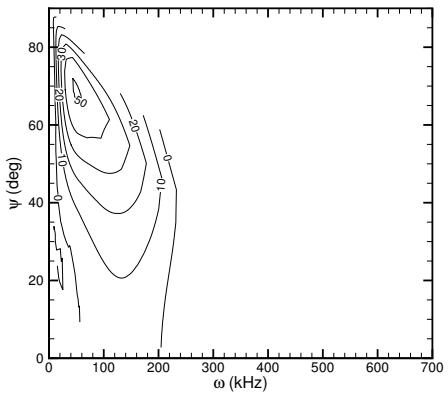
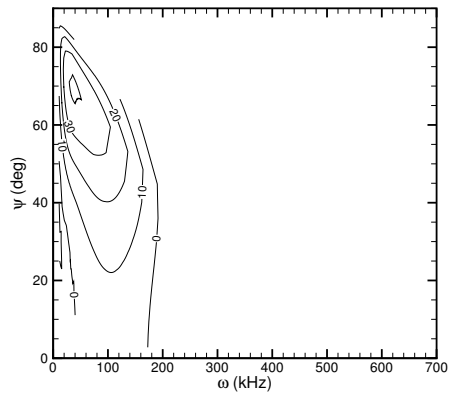
(a)  $R=500$  ( $s = 0.00849$  m)(b)  $R=750$  ( $s = 0.0191$  m)(c)  $R=1000$  ( $s = 0.0339$  m)(d)  $R=1500$  ( $s = 0.0764$  m)(e)  $R=2000$  ( $s = 0.136$  m)(f)  $R=2500$  ( $s = 0.212$  m)

Figure 4.4: Amplification rate for the sharp cone at Mach 3.5 as a function of frequency and wave angle for various axial locations.



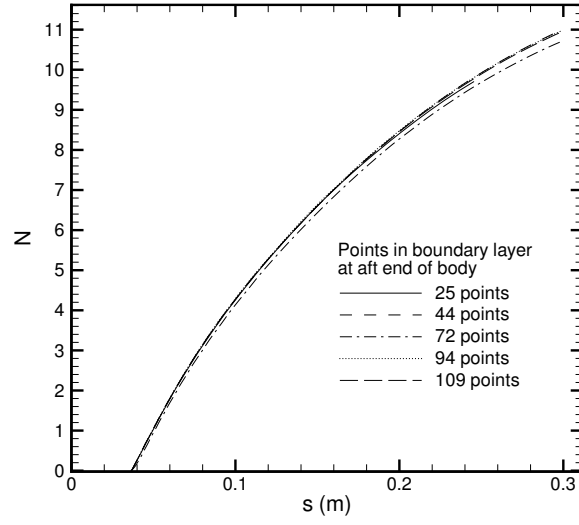


Figure 4.5: N factor calculations for the sharp cone at Mach 3.5 with five separate mean flow grids. Calculations are for a mode with  $\omega = 104$  kHz and  $\beta = 2400/\text{m}$ , beginning at  $s = 0.0339$  m.

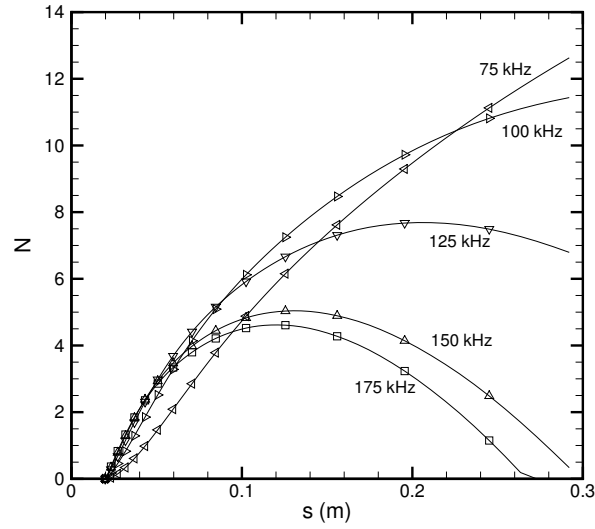


Figure 4.6: Maximum N factors obtained from many combinations of frequency, spanwise wavenumber, and starting location for the sharp cone at Mach 3.5.

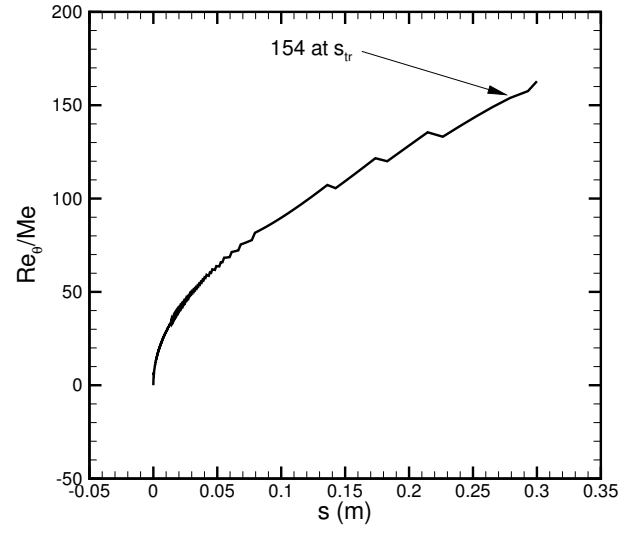


Figure 4.7: Ratio of edge momentum thickness Reynolds number to edge Mach number for the sharp cone at Mach 3.5.

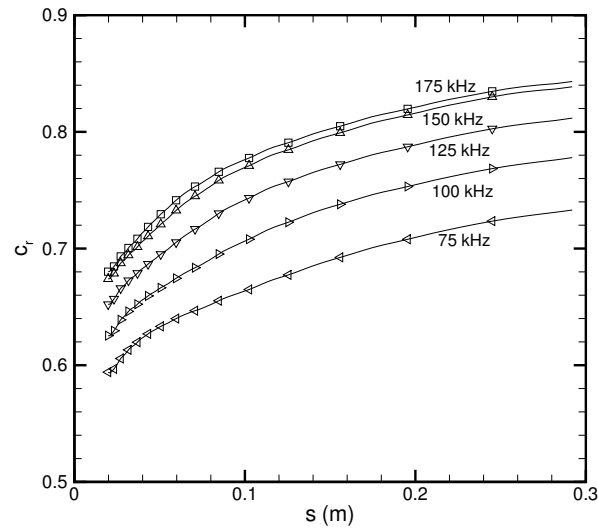


Figure 4.8: The phase speed for the five most amplified modes on the sharp cone at Mach 3.5.

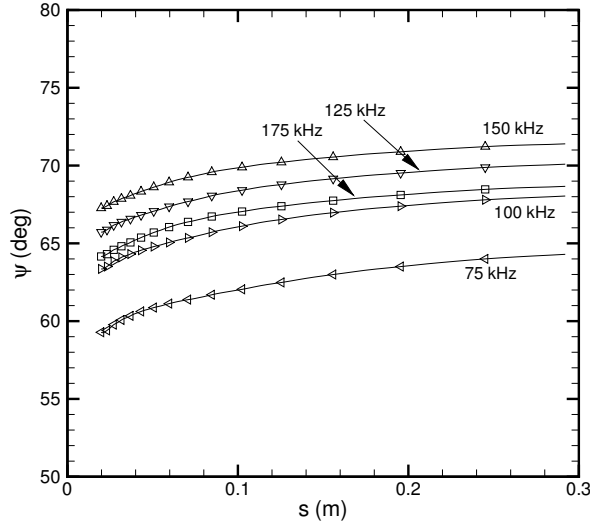


Figure 4.9: The wave angle for the five most amplified modes on the sharp cone at Mach 3.5.

Figure 4.8 shows the phase speed for each of the five modes shown in Figure 4.6. The phase speed is always within the range 0.55–0.85, which is lower than the 0.90–1.00 range found for second mode waves. The phase speed increases for each mode as the surface distance increases, as is expected based on Equation 3.11 since  $\alpha_r$  decreases as the boundary-layer thickness increases. The phase speed increases at all distances as the frequency increases, as is also expected based on Equation 3.11. The phase speed of the most amplified mode at the transition location is 0.73.

Figure 4.9 shows the wave angles for each of the five modes shown in Figure 4.6. The wave angle increases as the surface distance increases, which is expected based on Equation 4.1 since  $\alpha_r$  decreases and  $\beta$  is held constant. No clear trend of wave angle with frequency is evident. The wave angle of the most amplified mode at the transition location is  $64^\circ$ .

Figure 4.10 shows the amplitude and phase of the temperature eigenfunction at the aft end of the cone for a 104 kHz disturbance with  $\beta = 2400$  1/m. Figure 4.11

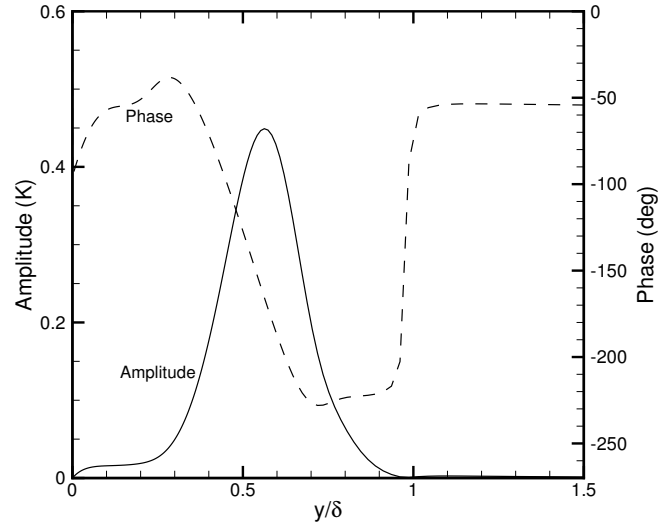


Figure 4.10: Amplitude and phase of the temperature eigenfunction for a 104 kHz disturbance with  $\beta = 2400$  1/m at the aft end of the sharp cone at Mach 3.5.

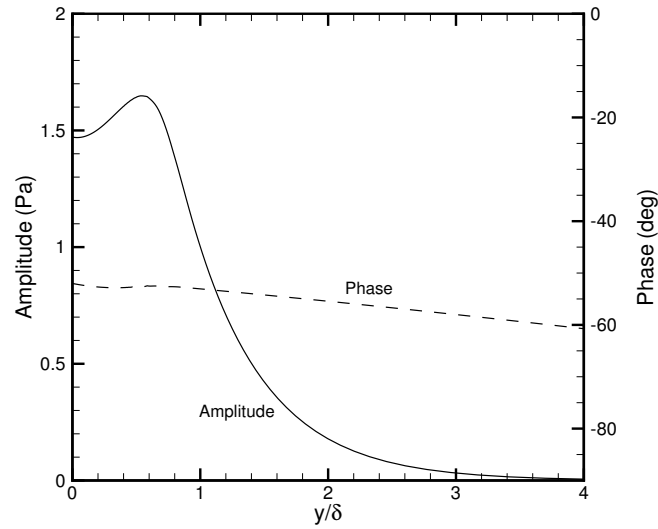


Figure 4.11: Amplitude and phase of the pressure eigenfunction for a 104 kHz disturbance with  $\beta = 2400$  1/m at the aft end of the sharp cone at Mach 3.5.

shows the pressure eigenfunction for the same disturbance. The one peak present in both the temperature and pressure amplitudes is indicative of a first mode disturbance. The shape of the pressure amplitude curve matches well with that shown by Mack [12] for first mode waves. The amplitudes shown are for an initial disturbance amplitude of 0.001 at  $s = 0.0339$  m.

#### 4.1.3 Verification and Validation Issues

Comparisons were made between the present results and those obtained by Malik using COSAL [61] and Kimmel using  $e^{Malik}$  (personal communication, March–April 2005). Malik calculated N factor growth rates for six frequencies ranging from 22–188 kHz. His most amplified mode at the experimental transition location has a frequency of 78 kHz, a wave angle of approximately  $60^\circ$ , and a N factor of 10.1. Compared to the transition N factor calculated by STABL of 12.2, this is a significant difference, although the frequency and wave angle of the most amplified disturbances agree to within 10%.

Figure 4.12 shows a comparison of the N factors calculated by STABL and those calculated by Kimmel using the  $e^{Malik}$  code for a mode at 104 kHz with  $\beta = 2400$  1/m. The N factors calculated by STABL are approximately 30% higher than those calculated by  $e^{Malik}$ . The agreement is much worse than that seen in Figures 4.2 and 4.3 for the mean-flow profiles. The difference in N factor may be due to the subtle differences in the mean flow, or it may be due to differences in the stability solvers. An attempt was made to analyze the  $e^{Malik}$  meanflow using PSE-Chem, but publication-quality results were not obtained due to problems converting the similarity solution to a general 2D flowfield.

## 4.2 Large-Bluntness Cone at Mach 8

All hypersonic vehicles have some degree of nosetip bluntness to control stagnation point heating. For a blunt cone, when the nose radius increases for a fixed, high

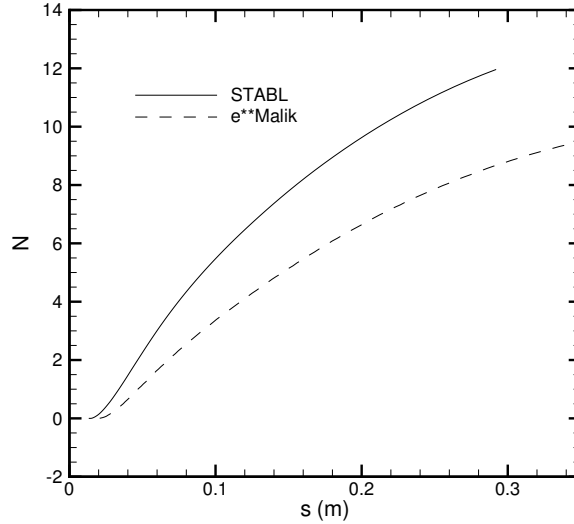


Figure 4.12: N factors calculated using STABL compared with results of Kimmel using  $e^{Malik}$  for a mode at 104 kHz with  $\beta = 2400$  1/m for the sharp cone at Mach 3.5.

freestream Mach number, the first mode may become dominant. For this reason, a very blunt cone was analyzed using the conditions shown in Table 4.2 to further verify first and second-mode computations. The flow conditions match those of the Stetson et al. [33] blunt cone experiment, but the bluntness was increased while the ratio of the nose-tip radius to the body length was kept constant, making this case impractical for wind tunnel experiments. This case was previously analyzed by Rosenboom et al. [38, 62]. This case was chosen for first mode verification because Rosenboom et al. found first mode N factor growth at a level comparable to second mode growth. Their LST based calculations showed a maximum first mode N factor at  $s = 11$  m of approximately 6.75 for a 2 kHz disturbance. For comparison, the maximum second mode N factor Rosenboom et al. calculated was 8.6 at 34 kHz. Kufner [63] performed calculations for this case without finding any first mode instabilities. However, Rosenboom points out that his second mode calculations for

Table 4.2: Test conditions for cone with  $r_n = 42.67$  mm at Mach 8

Condition	Value
Nose radius (mm)	42.67 mm
Cone half angle	$7^\circ$
Maximum arc length (m)	11.35
Wall temperature	Adiabatic
Fluid	Air
$M_\infty$	7.99
$p_o$ (kPa)	4000
$T_o$ (K)	750
$T_\infty$ (K)	54
$\rho_\infty$ (kg/m <sup>3</sup> )	$2.7 \times 10^{-2}$
$Re_\infty/m$	$2.5 \times 10^6$

this case suffered from numerical difficulties that manifested themselves as wiggles in the disturbance growth rates. This casts doubt on the first mode calculations for the present case.

An accurate mean flow was computed using a mesh with 450 axial points and 350 wall-normal points. Approximately 100 grid points were contained within the boundary-layer over the cone frustum. The edge Mach number was 4 near the cone shoulder and increased to 6.3 far downstream of the nose.

#### 4.2.1 First Mode Stability

Rosenboom et al. [38] calculated the first mode critical point to be 0.15 m. Figure 23 of Reference [38] shows all frequencies from 1–9 kHz becoming unstable around 0.15 m, followed by a region of approximately 5 meters where they again become

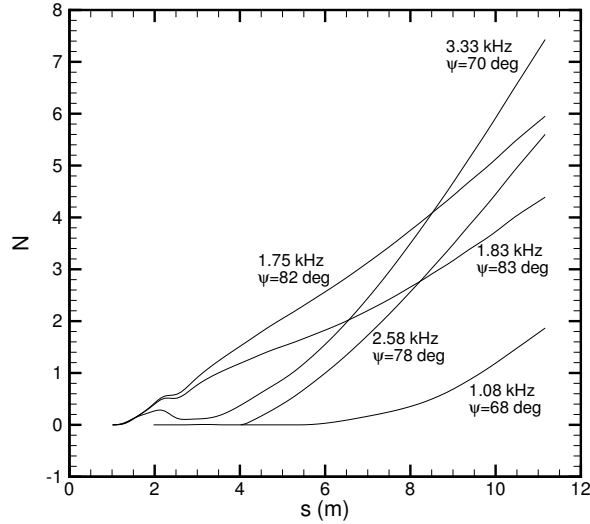


Figure 4.13: First mode N factors for the large bluntness cone at Mach 8.

stable, and a region from  $s = 7$  m to the end where all frequencies from 1–9 kHz are again unstable. Figure A.12 of Reference [62] shows the wave angles for the instabilities Rosenboom calculated. For frequencies from 1–5 kHz, the wave angle is greater than  $80^\circ$  at the critical point, drops to around  $60^\circ$  almost immediately, and eventually levels off between  $65^\circ$  and  $70^\circ$ . For frequencies greater than 5 kHz, the wave angle is less than  $50^\circ$  at the critical point but rises to the trend of the lower frequencies by  $s = 1$  m. Figure 28 of Reference [38] shows N factors for this case. Rosenboom shows amplification from 0.5–2.0 m, a short period of damping, and then monotonic growth from approximately 4 m to the end of the cone. The figure was digitized using the Un-Scan-It software, and  $N = 5.5$  is first reached at  $s = 9.7$  m by the 2 kHz mode at a wave angle of  $70^\circ$ .

Computations were performed with STABL to compare with the results of Rosenboom et al. Figure 4.13 shows samples of the first mode N factors calculated by STABL. A test matrix consisting of combinations of  $s = 0.5, 1.0, \dots, 10.5$  and  $\beta = 20, 40, \dots, 100$  1/m was analyzed. Combinations involving additional values



Table 4.3: Transition location predictions for the large bluntness cone at Mach 8. Transition is assumed at  $N = 5.5$ .

Computation	$s_{tr}$ (m)	$\omega$ (kHz)	$\psi$
First Mode			
STABL	9.7	3.33	$70^\circ$
Rosenboom et al. [38, 62]	9.7	2	$70^\circ$
Second Mode			
STABL	9.0	34	$0^\circ$
Rosenboom et al. (local) [38]	9.6	34	$0^\circ$
Rosenboom et al. (nonlocal) [38]	9.8	34	$0^\circ$

of  $\beta < 20$  1/m were also analyzed separately, but no significant amplification was found. For all cases shown, 100 frequencies within the range 1–10 kHz were analyzed at the starting location using LST, and the lowest unstable frequency was used for PSE marching. For these particular conditions, that lowest unstable frequency was always the lowest for which the global and local solvers could obtain converged solutions. The spanwise wavenumber  $\beta$  and the frequency  $\omega$  were fixed as the marching progressed downstream. Table 4.3 summarizes the comparison.  $N = 5.5$  is first reached at  $s = 9.7$  m by a 3.33 kHz instability at  $70^\circ$ . Despite differences in the frequency, the transition location and wave angle predicted by STABL and Rosenboom et al. are the same. In addition, the general characteristics of the N factor curves calculated by STABL and Rosenboom et al. agree well. Both show an initial hump, followed by brief damping and a long rise.

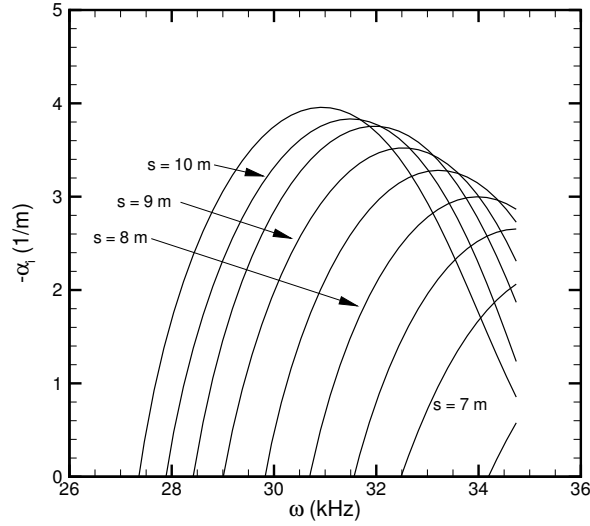


Figure 4.14: Second mode amplification curves for the large-bluntness cone at Mach 8.

#### 4.2.2 Second Mode Stability

A comparison was also made with the second mode stability results of Rosenboom et al. Rosenboom shows second mode amplification beginning at  $s = 5.5$  m at 40 kHz.  $N = 5.5$  is reached at approximately 9.6 m for the local calculation and approximately 9.8 m for the nonlocal calculation at a frequency of 34 kHz for both local and nonlocal.

Figure 4.14 shows the second mode amplification curves calculated by STABL. For the computations shown, a frequency range of 20–60 kHz was analyzed, but no eigenvalues were found by the global solver at frequencies greater than 35 kHz for any location. These calculations found a critical frequency of 34 kHz at  $s = 6.5$  m. The peak amplification increases and the unstable frequencies decrease as  $s$  increases. The critical location is slightly aft of Rosenboom's critical location of 5.5 m at 40 kHz. However, since the lack of eigenvalues above 35 kHz in PSE-Chem's calculations appears to have been caused by unknown numerical difficulties, higher frequency

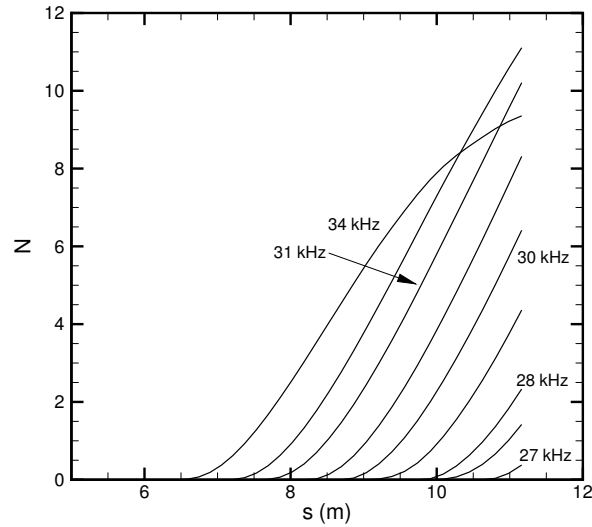


Figure 4.15: Second mode N factors for the large-bluntness cone at Mach 8.

modes may have provided better agreement in the critical location. Rosenboom shows the 34 kHz mode beginning to amplify at  $s = 7$  m, which is comparable to the location calculated by STABL of 6.5 m.

Figure 4.15 shows the second mode N factor curves generated by STABL. A frequency range of 20–60 kHz was analyzed in 2 kHz increments for the global solution and 0.2 kHz increments for the local solution, but no eigenvalues were found by the global solver at frequencies greater than 35 kHz for any location. STABL selected the critical frequency at each starting location to begin PSE marching. Table 4.3 summarizes the comparison. Amplification begins at  $s = 6.5$  m, slightly behind the critical location of  $s = 5.5$  m calculated by Rosenboom et al. An N factor of 5.5 is first reached at  $s = 9.0$  m by a 34 kHz wave. This is slightly ahead of the location calculated by Rosenboom of  $s = 9.6$  m for the local calculation or  $s = 9.8$  for the nonlocal calculation, but the difference is on the order of the starting distance resolution of 0.5 m. Additional computations should be performed to reduce the gap

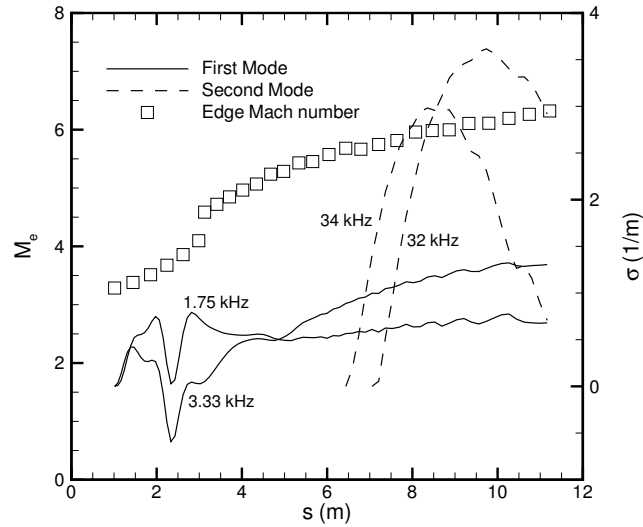


Figure 4.16: A comparison of the spatial growth rates of the largest first and second-mode N factors for the large-bluntness cone at Mach 8.

between STABL computations. Overall second-mode agreement between STABL and Rosenboom is good.

An outstanding question in stability theory is the nature of the interaction between the first and second modes. Figure 4.16 shows the amplification rates of the most amplified first and second mode waves, and Figure 4.17 shows the N factors for those waves. Both figures show the edge Mach number distribution. The apparent discontinuity in the edge Mach number at  $s = 3$  m is caused by numerical difficulties of the type described in Section 3.2.3. The first mode amplifies over the full length of the body. The second mode begins to amplify when the edge Mach number is 5.7, and it becomes dominant when the edge Mach number is 6.0.

The calculations also showed another unstable mode that was not expected. Figure 4.18 shows the N factors calculated by two-dimensional waves at 1 kHz. The different curves represent different starting locations. The waves amplify very slightly until  $s = 3$  m, at which point they amplify very rapidly until  $s = 4$  m. They then

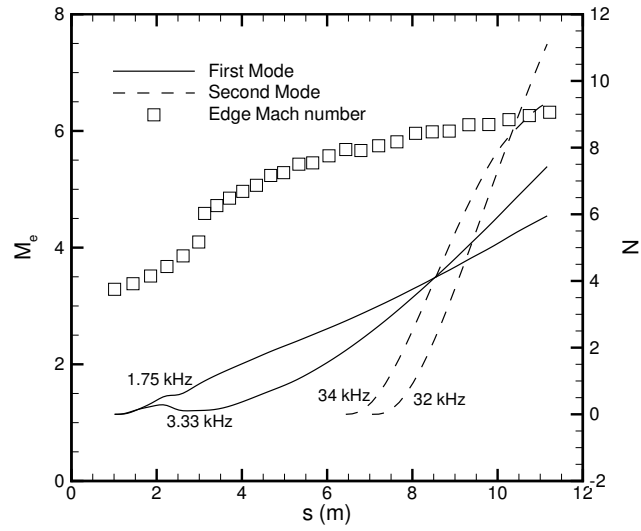


Figure 4.17: A comparison of the largest first and second-mode  $N$  factors calculated by STABL for the large bluntness cone at Mach 8.

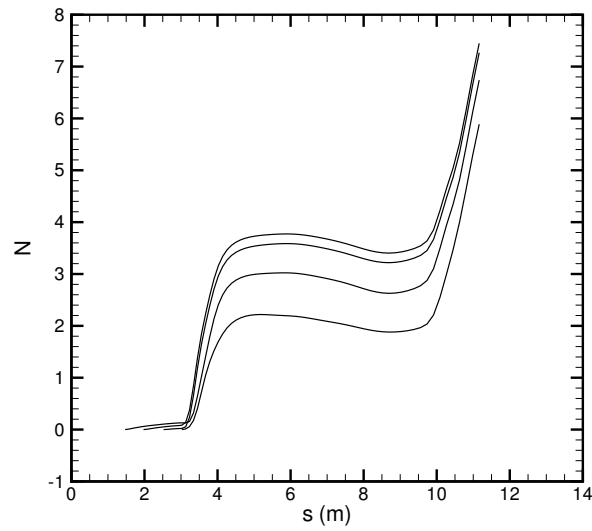


Figure 4.18:  $N$  factors of a two-dimensional instability at 1 kHz on the large-bluntness cone at Mach 8. The four lines represent different beginning marching locations.

decay slightly until  $s = 10$  m, at which point they again amplify rapidly until the end of the body.  $N = 5.5$  is first reached at  $s = 10.6$  m. These waves were found serendipitously during a search over the 1–10 kHz frequency range when the lowest amplified frequency was chosen for marching. Although this search was run every 0.5 m, only the starting locations between 1.5 and 3.0 m exhibited this behavior. The reason for the different amplification between the different starting locations is unknown. This might be a new phenomenon, but further investigation is necessary before it can be characterized.

## 5. Comparisons to Purdue Mach-6 Ludwig Tube Experiments

As discussed in Chapter 3, the Stetson et al. [33] hot-wire measurements are of limited utility for validation purposes. In addition, the expense of conducting research experiments in a production wind tunnel like Tunnel B makes it unlikely that the test can be replicated in that tunnel. For this reason, Rufer and Schneider [64] have been developing equipment and procedures to conduct hot-wire measurements of instability waves in the Purdue Mach-6 Ludwig Tube (M6LT). Although this wind tunnel is designed for quiet flow, it is currently quiet only at low unit Reynolds numbers [11], and the experiments described here take place under conventional-noise conditions. The measurement of natural second-mode instability wave growth is complicated by the six-to-ten-second usable run time of the M6LT, which makes calibration in the tunnel difficult and results in frequent wire breakage from the many start-up and shut-down cycles. This chapter will present computations that are designed to match the conditions of several of Rufer's experiments.

The test conditions for the cases discussed here are summarized in Table 5.1. The total pressure corresponds to the pressure in the tunnel driver tube, and it was set to one of the three values shown in the table. The specific value will be noted for each case. In addition, as the driver tube empties, the total pressure decreases throughout the run, and the value given in Table 5.1 is the nominal total pressure at the beginning of the run. As the hot-wire measurements were taken within the first second of operation, the actual pressure should be close to the nominal pressure. The freestream Mach number also changes as the total pressure changes throughout the run. The wall temperature listed in Table 5.1 is an estimate. Although the driver tube section of the M6LT is heated to 433 K, the temperature of the test section is

Table 5.1: Nominal test conditions for the hot-wire experiments of Rufer [64]

Condition	Sharp Cone	Blunt Cone
Half angle	7°	7°
Length, x (m)	0.5689	0.5653
Base diameter (m)	0.1397	0.1397
Nose radius (mm)	0	0.508
Wall temperature (K)	300	300
Fluid	Air	Air
$M_\infty$	5.8	5.8
$p_o$ (psia)	90, 125	45, 125
$T_o$ (K)	433	433
$T_\infty$ (K)	56	56
$\rho_\infty$ (kg/m <sup>3</sup> )	0.03008, 0.04177	0.01504, 0.04177

believed to be at or near room temperature. The short run time is assumed to be insufficient to cause significant heating of the model. The sensitivity of the stability to small deviations from these assumptions will be discussed.

Distances in this section are expressed using both the axial length  $x$  and the arc length  $s$ . STABL uses the arc length for all of its calculations, but the experimentalist uses  $x$ . These are related by Equation 5.1, where the cone half angle  $\phi$  is given in degrees.

$$s(x) = 2\pi r_n \frac{90 - \phi}{360} + \frac{x - r_n(1 - \tan \phi)}{\cos \phi} \quad \text{for all } x > r_n \quad (5.1)$$

For a sharp cone,  $r_n = 0$  and Equation 5.1 reduces to  $s(x) = x / \cos \phi$ .

Mean flows were computed for all cases using grids with 440 axial points and 350 streamwise points. The outer grid boundary was carefully specified to closely match the angle of the shock. Stretching was used to cluster the points near the nose and the body surface. Approximately 100 wall-normal points were contained within the



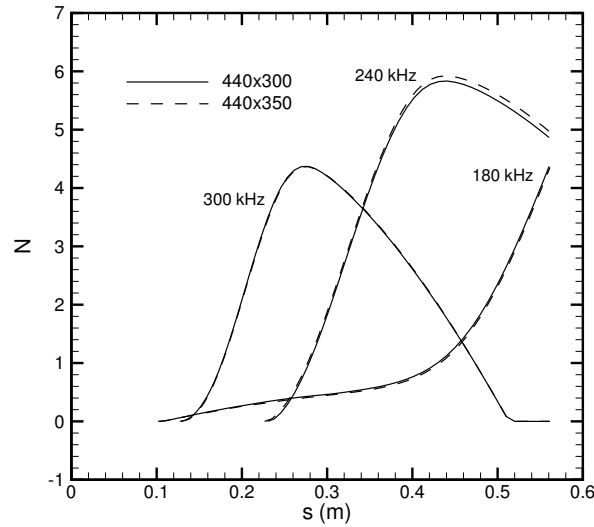


Figure 5.1: N factors calculated for Rufer's blunt cone at 125 psia using two separate grids.

boundary layer. A second mean flow was calculated using a 440x300 mesh for one of the cases. Although the outer grid boundary was the same for each grid, different stretching parameters were used. The second grid had a minimum of 70 points in the boundary layer. Figure 5.1 shows three sets of N factor calculations using each of the grids. The results are almost identical, which suggests that the results are grid independent. The results of this test and those shown in previous chapters were deemed sufficient to assume grid independence for the other cases calculated in this chapter.

## 5.1 Sharp Cones

### 5.1.1 Sharp Cone: 90 psia

Figure 5.2 shows a comparison of the boundary-layer profiles calculated by STABL and measured by Rufer at two axial locations. Calibrated hot-wire measurements

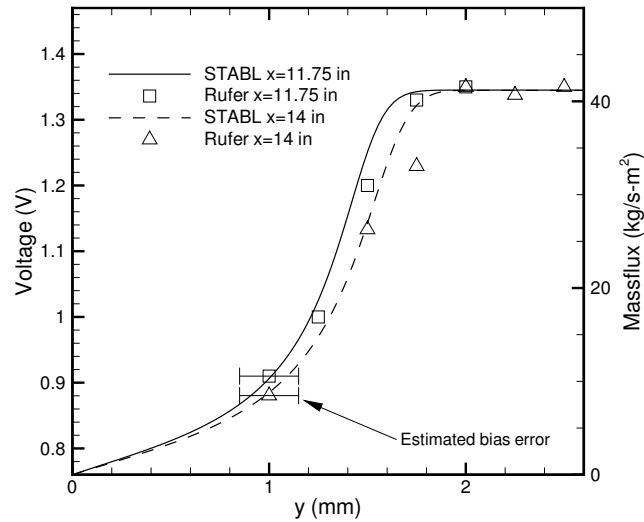


Figure 5.2: A comparison of the mass flux calculated by STABL with the uncalibrated hot wire measurements of Rufer at two locations on the sharp cone at 90 psia.

are needed for a direct comparison between experiment and computation. As of this writing, only uncalibrated hot-wire measurements have been obtained. As the hot-wire mean voltage is proportional to the mass flux, a limited comparison can still be made using these uncalibrated measurements. The height and shape of the boundary-layer profiles can be compared by adjusting the scales of the computations and experiments to make the curves fit as well as possible. However, a full comparison will require calibrated measurements. The height of the hot wire relative to the cone wall is determined using a telescope and custom-built lens system that is designed to correct for the optical distortion caused by the thick, curved plexiglass window. The bias error in the measured heights is estimated to be within 0.15 mm. The distance between successive data points is controlled by the traverse mechanism, and the error is presumed to be negligible. Measurements were taken on separate runs to minimize the effect of the pressure drop during the run. For this

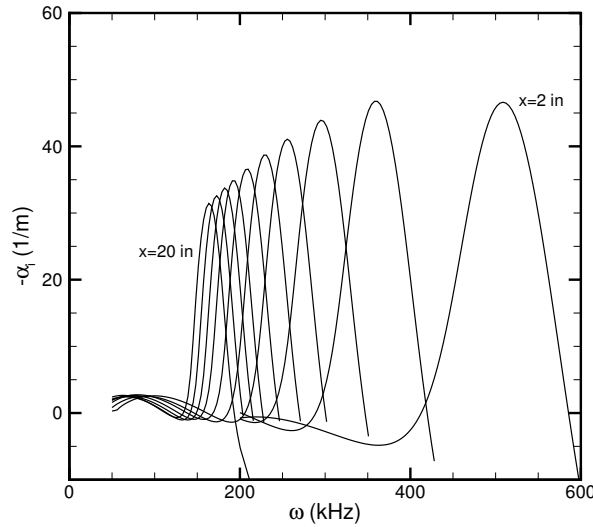


Figure 5.3: Amplification rate curves for Rufer's sharp cone at 90 psia. The spacing between the curves is two inches.

case, the boundary layer thickness calculated by STABL and measured by Rufer appear to agree to within the uncertainty in the measurements for both axial locations. Agreement with the profile shape is good, particularly for the  $x = 11.75$  inch data. Separate scales are used for the voltage for each axial distance, but for clarity only the scale for the  $x = 11.75$  inch measurements is shown.

Figure 5.3 shows amplification rate curves calculated by STABL for several axial locations. As expected, the most unstable frequency decreases as the boundary layer thickens. The peak amplification rate also decreases with increasing distance downstream. This trend is similar to that seen in Figures 3.29 and 4.4.

N factor curves for this case are shown in Figure 5.4. Modes with frequencies higher than 300 kHz are not shown, as they were not necessary to define the N-factor envelope in the region near transition. Figure 14 in Rufer and Schneider [64] shows suspected second-mode instabilities at  $x = 11.75$  inches and  $x = 14.0$  inches but not at  $x = 16.7$  inches. This is taken as an indication that transition occurred somewhere

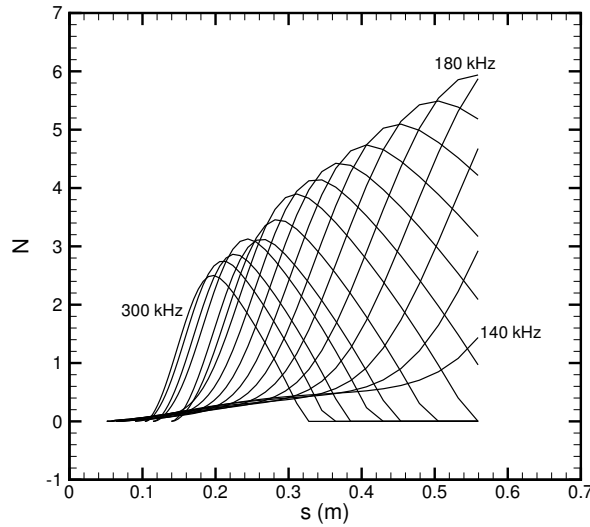


Figure 5.4: N factors for Rufer's sharp cone at 90 psia. The spacing between the curves is 10 kHz.

between 14.0 and 16.7 inches, although it should be noted that this may not coincide with the transition location that would be found using a different detection method. Using the envelope of the curves shown in Figure 5.4, transition occurred between N factors of 4.3 and 4.7. The expected transition N factor will be lower for experiments in the M6LT than for those in Tunnel B because the noise level is higher in smaller tunnels [10]. Thus, transition N factors less than 5 are not surprising. The most amplified frequencies calculated by STABL at  $x = 11.75$  inches and  $x = 14.0$  inches are 220 kHz and 200 kHz. These are within 10% of the peaks on the amplification curve shown in Figure 14 of Rufer and Schneider [64], which are 235 kHz and 200 kHz, respectively. Table 5.2 summarizes the comparison with Rufer's data for all of the cases discussed in this chapter.

Table 5.2: Comparison of most unstable frequencies calculated by STABL and measured by Rufer [64]. Transition N factors are also shown for each case.

Case	Location (in)	Rufer $\omega$ (kHz)	STABL $\omega$ (kHz)	$N_{tr}$
Sharp 90	11.75	235	220	4.3–4.7
	14.0	200	200	
Sharp 125	10.3	280	220	> 5.1
	12.3	250	280	
Blunt 125	14.25	240	260	> 5.4
Blunt 45	18.0	150	140	3.6–4.0
	20.0	130	130	

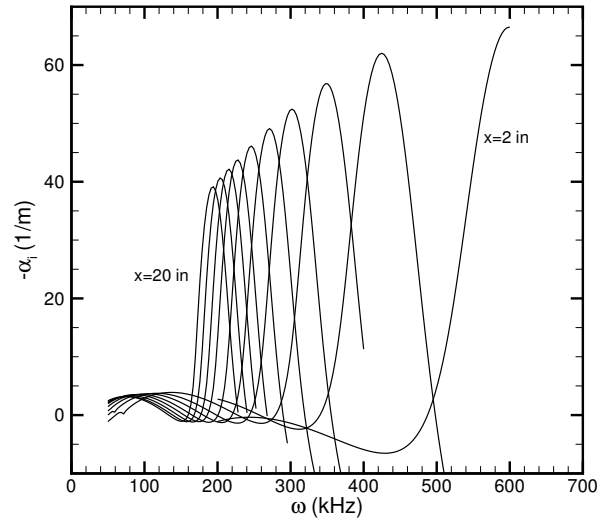


Figure 5.5: Amplification rate curves for Rufer's sharp cone at 125 psia. The spacing between the curves is two inches.

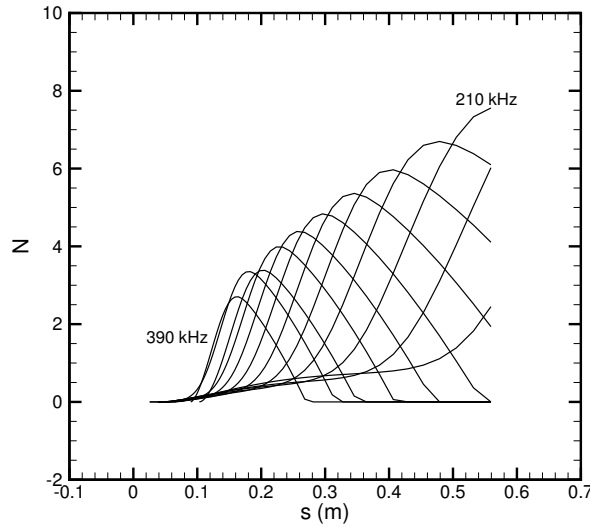


Figure 5.6: N factors for Rufer's sharp cone at 90 psia. The spacing between the curves is 20 kHz.

### 5.1.2 Sharp Cone: 125 psia

Figures 10 and 11 of Reference [64] show hot-wire spectra on a sharp cone with an initial driver-tube pressure of 125 psia. Although the cone used in this experiment was shorter than that used in the others, the same computational grid was used as for the 90 psia sharp cone. Figure 5.5 shows the amplification rate curves calculated by STABL for this case, and Figure 5.6 shows the N factors. The computation was carried out with 10 kHz spacing, but only 20 kHz spacing is shown in the figure for clarity. Rufer's frequency spectra show a peak amplitude of approximately 280 kHz at  $x = 10.3$  inches and 250 kHz at  $x = 12.3$  inches. STABL calculates an N factor of 4.5 at 300 kHz at  $x = 10.3$  inches, and an N of 5.1 at 280 kHz at  $x = 12.3$  inches. Transition was not observed for this condition, so the transition N factor is presumed to be greater than 5.1.

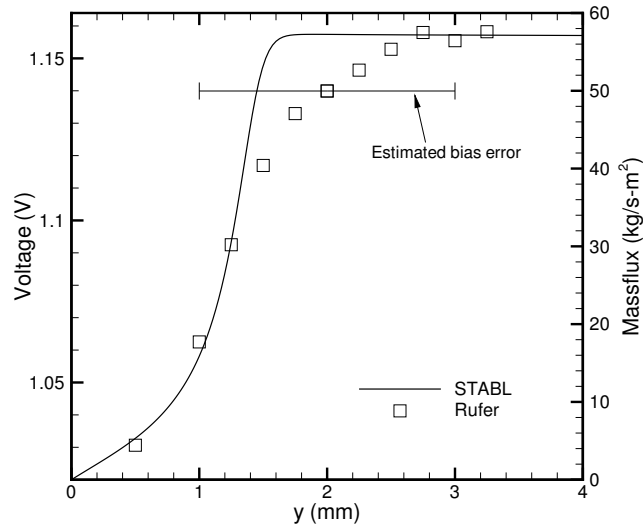


Figure 5.7: A comparison of the mass flux calculated by STABL with the uncalibrated hot wire measurements of Rufer at  $x = 14.25$  inches on the blunt cone at 125 psia.

## 5.2 Blunt Cones

### 5.2.1 Blunt Cone: 125 psia

Figure 5.7 shows a comparison of the boundary-layer profiles measured by Rufer and computed by STABL for the blunt cone with a 125 psia driver tube pressure. These measurements were conducted before the telescope system was in place to increase the accuracy of the hot-wire positioning relative to the cone wall. Thus, although the distance between Rufer's points is accurate, the entire set may have a constant error in the wall normal distance of up to 1 mm. This comparison shows a boundary-layer calculated by STABL that is approximately 1 mm thinner than that measured by Rufer. The maximum difference in the profile shape is approximately 20% with respect to the massflux scale. These measurements are being repeated using the new system to try to resolve these differences.

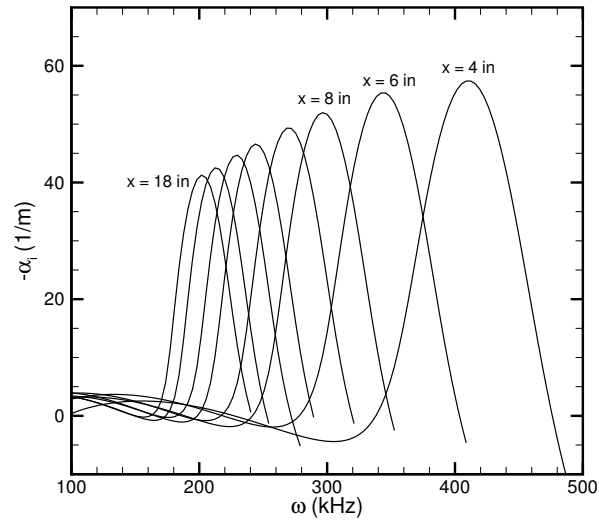


Figure 5.8: Amplification rate curves for Rufer's blunt cone at 125 psia. The spacing between the curves is two inches.

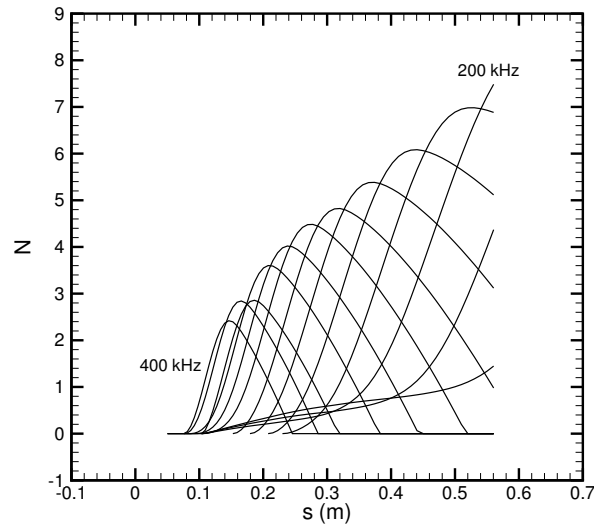


Figure 5.9: N factor curves for Rufer's blunt cone at 125 psia. The spacing between the curves is 20 kHz.



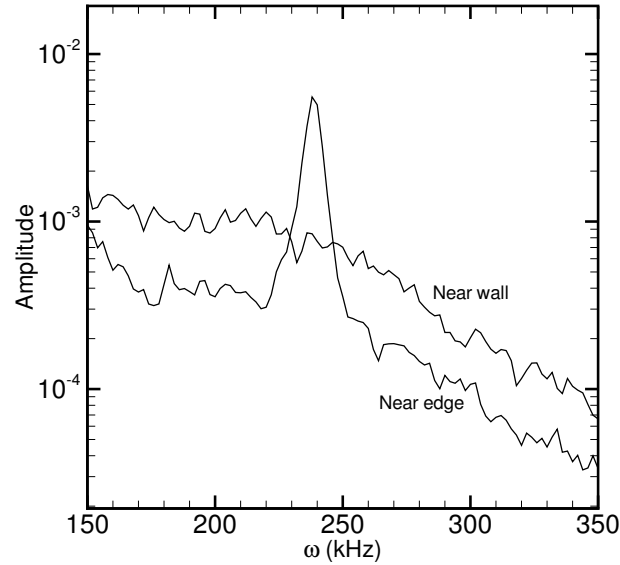


Figure 5.10: Frequency spectra measured by Rufer at  $x = 14.25$  inches on the blunt cone at 125 psia.

Figure 5.8 shows amplification rate curves for every two inches in the range  $4 \text{ in} < x < 18 \text{ in}$ . Well defined second mode peaks are present. The bandwidth of the unstable region is approximately 150 kHz near the nose and 100 kHz farther aft. Figure 5.9 shows  $N$  factor curves for this case. The computation was carried out with 10 kHz spacing, but only 20 kHz spacing is shown in the figure for clarity. A clear envelope is evident.  $N = 5.5$  is first reached by a 240 kHz wave at  $s = 0.388 \text{ m}$  ( $x = 15.2 \text{ in}$ ).

Figure 5.10 shows frequency spectra measured by Rufer at  $x = 14.25$  inches. A sharp peak is evident near the boundary-layer edge with no corresponding peak near the wall. The peak frequency of approximately 240 kHz is close to the frequency with the highest  $N$  factor calculated by STABL, which is 260 kHz at that location. The frequency calculated by STABL to have the highest amplification rate at  $x = 14.25$  inches is 226 kHz.

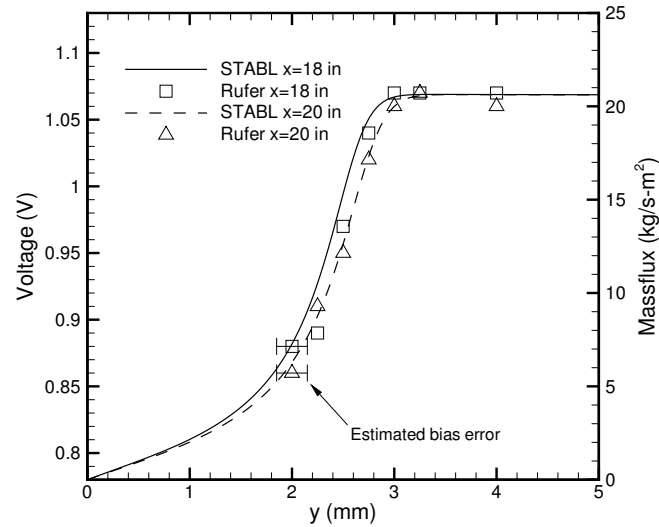


Figure 5.11: A comparison of the mass flux calculated by STABL with the uncalibrated hot wire measurements of Rufer at two locations on the blunt cone at 45 psia.

### 5.2.2 Blunt Cone: 45 psia

Figure 5.11 shows a comparison of the boundary layer profiles computed by STABL and measured by Rufer using the telescope and lens system for the blunt cone at 45 psia. No discernable difference is present in the computed and measured boundary layer thicknesses. In addition, the shape of the profiles agrees well, with a maximum deviation of any point of less than 5%. The same scale is used for both sets of experimental data.

Figure 5.12 shows amplification rate curves calculated by STABL for several axial locations. The trend here is slightly different than that seen for the sharp and blunt cones at 125 psia, in that the largest amplification rate seen is not the most forward curve. The trends seen in the amplification rate plots for the other cases are probably caused by the computations not being carried out far enough forward to capture behavior just aft of the critical point. This should not affect the N factor

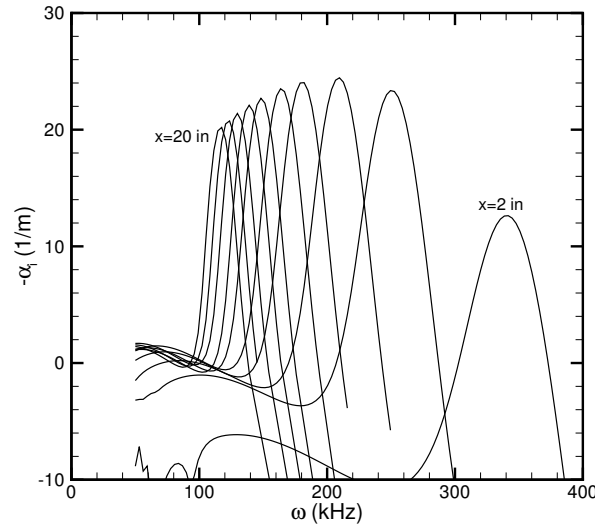


Figure 5.12: Amplification rate curves for Rufer's blunt cone at 45 psia. The spacing between the curves is two inches.

calculations, since the high frequency disturbances that begin to amplify first damp out well before the N factor envelope reaches the transition value. The N factor calculations were begun far upstream of where the transition-causing modes first begin to amplify.

Figure 5.13 shows N factors for the blunt cone at 45 psia. Figure 18 in Rufer and Schneider [64] shows suspected second-mode instabilities at  $x = 18$  inches and  $x = 20$  inches but not at  $x = 22$  inches, suggesting transition occurred between 20 and 22 inches. Using the curves in Figure 5.13, these locations correspond to N factors of 3.6 and 3.7. Improved frequency resolution in the computation might increase the latter number to approximately 4.0. The peaks of the power spectra in Figure 18 of [64] occur at approximately 150 kHz and 130 kHz. The most amplified frequencies in Figure 5.13 at those locations are 140 kHz and 130 kHz, respectively. Agreement is again within 10%.

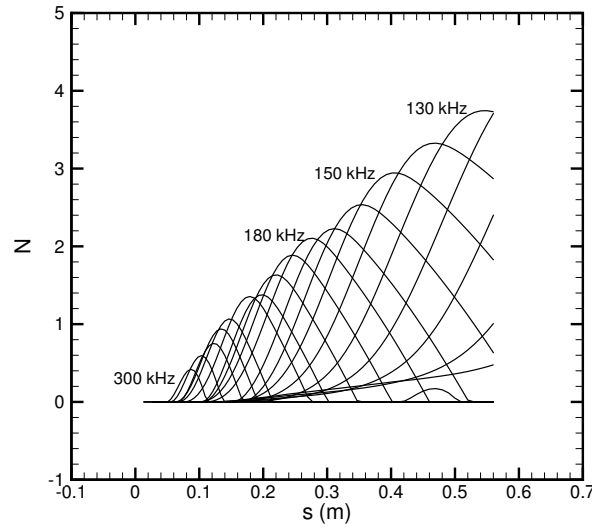
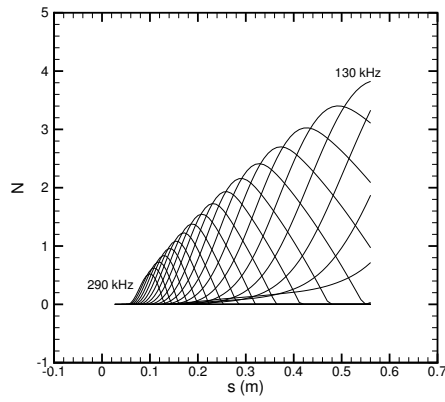


Figure 5.13: N factors for Rufer's blunt cone at 45 psia. The spacing between the curves is 10 kHz.

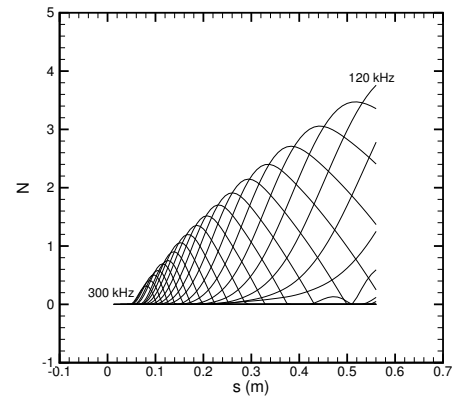
Appendix D provides all of the input conditions needed to obtain the mean flow for this case and the stability results shown in Figure 5.13. Numerical output from selected points is also tabulated.

### 5.3 Sensitivity Studies

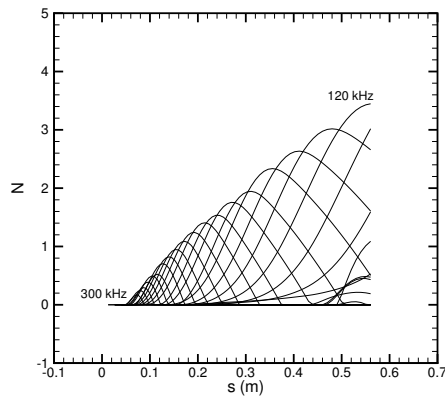
In order to gauge the effect of the various assumptions made in setting up the boundary conditions, several cases were analyzed with slight perturbations to the boundary conditions. The blunt cone at 45 psia was chosen as the baseline case due to the available high quality experimental data, the fact that all flight vehicles have some degree of bluntness, and the relative ease of numerical solution of blunt relative to sharp cones. The test conditions, summarized in Table 5.3, were chosen to represent a reasonable band of uncertainty in the nominal conditions. Each case changed only one variable from the baseline values.



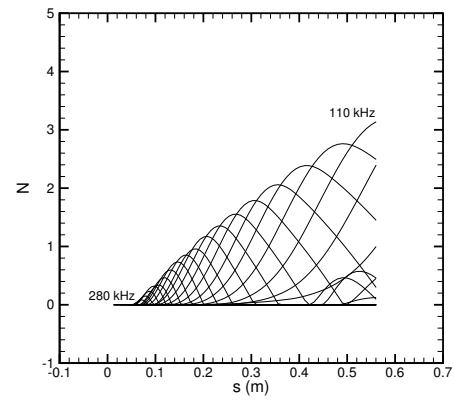
(a) Case A



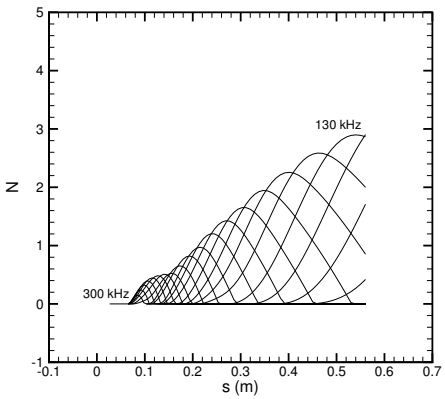
(b) Case B



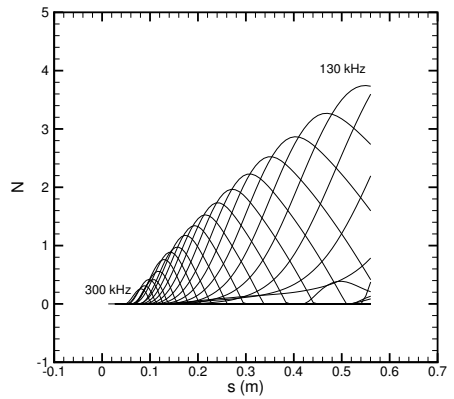
(c) Case C



(d) Case D



(e) Case E



(f) Case F

Figure 5.14: N factor curves obtained with various perturbations to nominal boundary conditions for Rufer's 45 psia blunt cone.

Table 5.3: Frequencies, N factors, and transition locations for a variety of input conditions for Rufer's blunt cone at a nominal driver tube pressure of 45 psia. Frequencies and N factors are for  $x = 20$  inches.

Case	$M_\infty$	$p_o$ (psia)	$T_{v_\infty}$ (K)	$T_w$ (K)	$\omega$ (kHz)	N	$s_{N=2.5}$ (mm)
Base	5.8	45	56	300	130	3.63	340
A	5.7	45	56	300	130	3.47	338
B	5.9	45	56	300	130	3.47	345
C	5.8	40	56	300	120	3.19	379
D	5.8	35	56	300	110	2.75	438
E	5.8	45	433	300	130	2.82	436
F	5.8	45	56	dist1	130	3.61	339

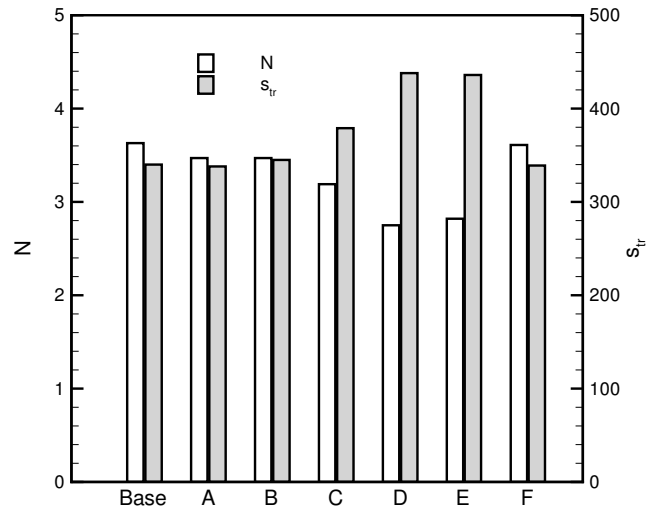


Figure 5.15: N factors and transition locations obtained with various perturbations to nominal boundary conditions for Rufer's 45 psia blunt cone.

Figure 5.14 shows the  $N$  factor curves for the six perturbed cases, and the results are summarized in Table 5.3. Figure 5.15 graphically depicts the  $N$  factors and transition arc lengths shown in Table 5.3. The most amplified frequency and maximum  $N$  factor are taken at  $x = 20$  inches ( $s = 0.5121$  m). A transition arc length is also given based on an  $N_{tr}$  of 2.5. Although this is considerably smaller than the expected transition  $N$  factor, this was the highest round number that was reached by all of the cases. In future studies of this type, the computational domain should be extended to ensure that a reasonable transition  $N$  factor is reached in the domain. Although this  $N$  factor is low, the envelope curve is reasonably linear, and the trends should still hold.

Cases A and B represent a small difference in the freestream Mach number.  $M_\infty$  is a function of the area ratio in the tunnel, which changes with  $p_o$ . Pitot measurements with the cone in the M6LT showed an approximate range of  $5.7 \leq M_\infty \leq 5.9$ , but values beyond the extremes were also seen. A 2% change in  $M_\infty$  caused a 4% change in the  $N$  factor at  $x = 20$  inches and a 1% change in the location where  $N = 2.5$ . The stability results do not appear overly sensitive to the freestream Mach number.

Cases C and D represent a change in the tunnel stagnation pressure. The amount is representative of the typical pressure drop during the course of the run. All of Rufer's instability measurements were taken within the first second of the run to minimize the effects of this pressure drop. A 22% decrease in  $p_o$  caused a 24% decrease in  $N$  and a 29% increase in  $s$ . In addition, this was the only variable which caused a significant change in the most unstable frequency. Since this perturbation is not an uncertainty, but rather a natural change in the test conditions, the best results will be obtained if all measurements are taken at the same time, as is currently done, rather than using the full test time.

Case E is the result obtained when the freestream vibrational temperature is set equal to the stagnation temperature. As discussed earlier, if the flow in a wind tunnel expands quickly enough, the translational and vibrational energy modes may not have time to equilibrate. The stagnation temperature in the M6LT is almost 50%

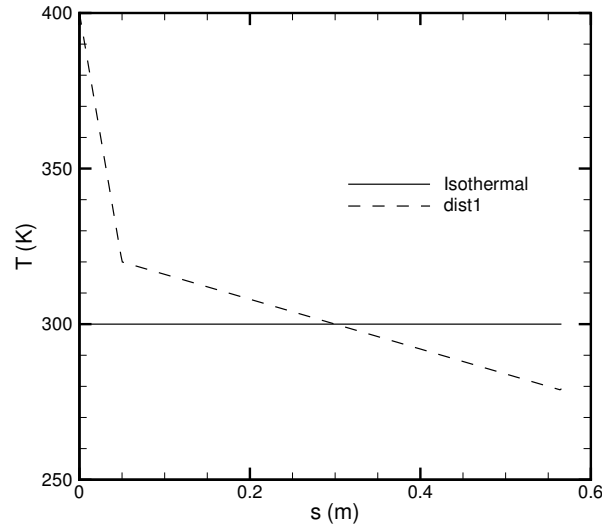


Figure 5.16: Wall temperature distribution “dist1” used in sensitivity study on Rufer’s 45 psia blunt cone.

lower than the threshold value proposed by Bertolotti [57] of 800 K. In addition, the very long nozzle in the M6LT makes flow relaxation more likely than in a conventionally designed tunnel. However, some degree of thermal nonequilibrium may be present, and this study will assess the potential effect. The baseline case assumes full equilibrium, while case E assumes frozen conditions. The effect of the frozen conditions is a 22% decrease in  $N$  and a 28% increase in  $s$ . This is a significant effect, and a computation of the flow of the tunnel should be made to determine the degree of thermal nonequilibrium present.

Case F was obtained by assuming the wall temperature had the distribution shown in Figure 5.16. The stagnation point wall temperature was set close to the freestream stagnation temperature, and the wall temperature was assumed to drop rapidly and fall below room temperature by the aft end. The actual distribution was arbitrary, but this was assumed to be a worst-case scenario with respect to the difference from a constant 300K wall. The effect of this distribution is negligible,



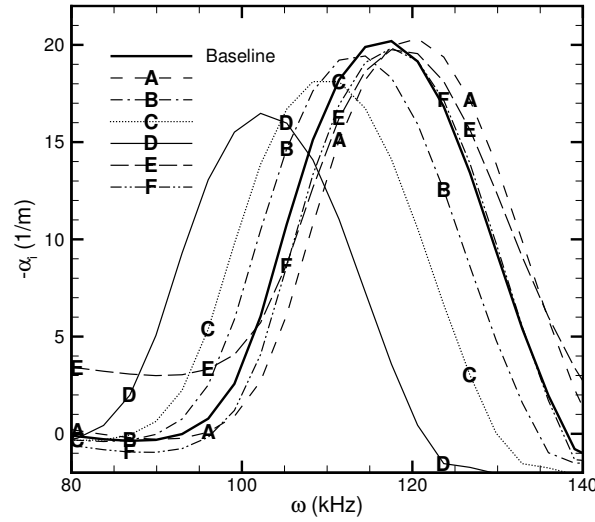


Figure 5.17: Amplification rate curves at  $x = 20$  inches for baseline and perturbed boundary conditions.

with less than a 1% effect on both  $N$  and  $s$ . This suggests that additional effort does not need to be spent to determine more precisely the actual wall temperature distribution.

The amplification rate curves at  $x = 20$  inches for the baseline and each of the perturbed conditions are shown in Figure 5.17. A clear trend of decreasing frequency and peak amplification rate is evident with increasing Mach number. As with the  $N$  factors, the largest difference from the baseline case is seen with cases C and D, which correspond to the total pressure drop. This has the effect of thickening the boundary layer, which decreases the unstable frequency. Interestingly, although freestream thermal nonequilibrium in case E has a large effect on the  $N$  factors compared to the other cases, the effect on the local amplification rate is small. Almost no difference is seen for the different wall temperature in case F.

## 6. Conclusions

Future systems involving hypersonic flight will require better methods of laminar to turbulent boundary-layer transition prediction. The current methods, which in most cases are empirical correlations combined with extrapolation from wind-tunnel tests, are inadequate to reduce design margins and expand the state of the art. The semi-empirical  $e^N$  method coupled with LST or the PSE shows promise for some conditions, but these methods have not yet successfully transitioned from the research to the design setting. The STABL code package is designed to make that transition, but before it can be used by researchers and accepted by designers, it will require extensive verification and validation.

STABL and its stability code, PSE-Chem, are currently transforming from an arcane research code designed for a single type of problem to a user-friendly, broadly-applicable prediction tool. As the first-ever user from outside the developer's research group, the author has been instrumental in suggesting and testing improvements to the user interface, method of operation, and documentation. Several bugs with varying degrees of severity have been uncovered. The experiences of the author have helped STABL's developers to understand the areas that need to be improved to make the tool accessible enough for design use. Several cases have been analyzed in an effort to verify and validate STABL.

The Stetson et al. [33] experiment is the best-known example of second mode wave growth on a blunt cone. The case has been computed by many other researchers, which makes it an ideal test case for code verification. Many issues were addressed to improve the agreement between the results of STABL and those of the other researchers.

This effort exposed the inadequacy of the method originally implemented in STABL for computing the viscosity of low-temperature flows, such as those com-

monly found in hypersonic wind tunnels. Modifications that were made to use a blended viscosity law improved agreement with experimental data and helped to extend the applicability of STABL to the low-temperature regime. A related issue was the use of the proper freestream density. Many CFD codes require a unit Reynolds number input, but the unit Reynolds number reported in Stetson et al. is not consistent with the other reported quantities if a Sutherland viscosity law is used. Thus, any researcher that used the unit Reynolds number specified by Stetson et al. as an input to a code that uses the Sutherland law modeled the flow conditions of the experiment incorrectly. In addition, the boundary-layer edge detection algorithm was modified to a more robust scheme which allows it to give an accurate location even when overshoots in the total enthalpy profile exist. The sensitivity of several other factors, including grid convergence, wall temperature, user-specified options, freestream thermal non-equilibrium, normalization, compilers, and PSE-Chem numerical behavior were all also examined.

The transition location predicted by STABL for the 3.81 mm Stetson cone agreed well with that predicted by other researchers. The location where  $N = 5.5$  is within about 5% of the other values in the literature. However, when LST is used to calculate the amplification rate at  $s/r_n = 175$ , STABL calculates a peak amplification rate that is more unstable than any of the data sets used for comparison. The difference is approximately equal to the scatter in the other results. Furthermore, when the viscosity model and method of calculating the freestream density were changed, the results calculated by STABL shifted by amounts similar to the overall scatter in the results. This shows a high sensitivity to the physical models employed, and work should continue in validating these models for various flow regimes. However, this viscosity-model uncertainty is currently less than the overall uncertainty in the  $e^N$  method, so this is not a critical issue at this point.

Computations were also conducted to verify the ability of STABL to predict first mode disturbances. The maximum N factor at the transition location was 12.2, which is slightly higher than expected. The N factor computed for a single mode

differed by 30% compared to a new corresponding calculation using the  $e^{Malik}$  code. Analysis of the  $e^{Malik}$  mean flow using PSE-Chem suggests that the differences could be caused by differences between the DPLR2D Navier-Stokes solution and the  $e^{Malik}$  similarity solution.

Analysis of an adiabatic large-bluntness cone at Mach 8 showed first-mode amplification over most of the body. Second-mode amplification began farther aft at an edge Mach number of 5.7, but its amplitude rapidly overtook that of the first mode and became dominant at  $M_e = 6.0$ . Agreement with the results of Rosenboom et al. [38] was excellent for first mode transition location and most unstable wave angle, although there was a significant difference in frequency. Second mode transition frequencies matched to within 3%, and the transition location agreed to within 10%.

Computations were also made to match the ongoing hot-wire experiments of Rufer in the Purdue Mach 6 Ludwig Tube. These experiments should provide an additional source of badly-needed validation data. Good agreement in the boundary layer shape and thickness is obtained for both blunt and sharp cones when the telescopic height-measurement system is used in the experiments. Agreement between experiment and computations in the most unstable frequency is within 10% for all cases shown in Rufer and Schneider [64]. Transition N factors based on locations inferred from hot-wire spectra ranged from 3.6 to greater than 5.4. This matches the expected trend that the transition N factors will be lower than in Tunnel B, since the smaller test section means that the noise intensity will be higher. The transition N factors decrease as the tunnel stagnation pressure decreases. This matches the unit Reynolds number effect observed in conventional wind tunnels, which says that transition Reynolds number decreases as unit Reynolds number decreases [10].

Sensitivity studies were also conducted to gauge the effect of various assumptions that were made. A dependence on freestream Mach number was observed, as a change of 2% in the Mach number caused a 4% change in the N factor at a given location. The normal change in the driver tube pressure over the course of a tunnel run caused a 25% change in the N factor and a 15% change in the frequency. This

reiterates the importance of taking measurements during the same driver-tube pressure window for each run. Freestream thermal non-equilibrium was found to have a potentially large effect on the stability computations, with a frozen freestream vibrational temperature resulting in a 22% decrease in the N factor, although the actual degree of freestream thermal nonequilibrium is unknown. Almost no effect was seen from a different wall temperature distribution.

A general observation is better agreement is found in overall transition locations computed using different computational methods than in the individual computations used to create the overall prediction. This was seen in Stetson's 3.81 mm blunt cone, where STABL calculated a local amplification rate that was higher than other researchers' results, but the predicted transition location fell within the scatter. It was also seen for the sharp cone at Mach 3.5. STABL and  $e^{Malik}$  calculated N factors for a single mode that disagreed by 30%, but the transition N factor STABL calculated was within 15% of the expected range for low disturbance environments. Since the N factor is an integrated quantity, and determining the transition location through the N factor envelope involves using many individual growth rates, it seems logical that this process would tend to smooth out differences in the growth rates.

It is interesting that the N factors seen for the sharp cone at Mach 3.5 were larger than expected, whereas those seen for Rufer's cases were smaller than expected. It is important to remember that the  $e^N$  method is semi-empirical. The N factor that best predicts transition is dependent on freestream noise and other factors, and it needs to be chosen from comparisons to experimental data. When Malik [61] first computed the sharp cone case, he appears to have performed a total of seven N factor calculations. In contrast, twenty-one years of advances in hardware and software allowed calculation of 480 individual N factors here. It does not seem unreasonable that this could result in a different transition N factor.

A great deal of progress has been made in transforming STABL from a research code to a design tool. The computations presented here help to provide confidence in the ability of STABL to analyze boundary-layer stability and predict transition.

These results can also serve as a benchmark to allow other researchers using STABL to verify their method of operation. Additional computations on different cases in a variety of flow regimes should be performed to further this effort.

## LIST OF REFERENCES

## LIST OF REFERENCES

- [1] John J. Bertin and Russell M. Cummings. Fifty years of hypersonics: Where we've been, where we're going. *Progress in Aerospace Sciences*, 39:511–536, 2003.
- [2] Ronald P. Fuchs et al. Why and whither hypersonics research in the US Air Force. Technical Report SAB-TR-00-03, US Air Force Scientific Advisory Board, December 2000.
- [3] Air Force Space Command. Strategic master plan FY06 and beyond, October 2003.
- [4] Steven P. Schneider. Hypersonic laminar-turbulent transition on circular cones and scramjet forebodies. *Progress in Aerospace Sciences*, 40(1):1–50, 2004.
- [5] Defense Science Board. Report of the Defense Science Board on the National Aerospace Plane (NASP). Technical report, Defense Science Board, September 1988. DTIC Citation AD-A201124.
- [6] Eli Reshotko. Boundary layer instability, transition and control. Paper 94-0001, AIAA, January 1994.
- [7] A.M. Berkowitz, C.L. Kyriss, and A. Martellucci. Boundary layer transition flight test observations. Paper 77-125, AIAA, January 1977.
- [8] John J. Bertin, Timothy E. Hayden, and Winston D. Goodrich. Shuttle boundary-layer transition due to distributed roughness and surface cooling. *Journal of Spacecraft and Rockets*, 19(5):389–396, Sept–Oct 1982.
- [9] Steven P. Schneider. Flight data for boundary-layer transition at hypersonic and supersonic speeds. *Journal of Spacecraft and Rockets*, 36(1):8–20, January–February 1999.
- [10] Steven P. Schneider. Effects of high-speed tunnel noise on laminar-turbulent transition. *Journal of Spacecraft and Rockets*, 38(3):323–333, May–June 2001.
- [11] Steven P. Schneider, Craig Skoch, Shann Rufer, Erick Swanson, and Matthew P. Borg. Laminar-turbulent transition research in the Boeing/AFOSR Mach-6 Quiet Tunnel. Paper 2005-0888, AIAA, January 2005.
- [12] Leslie M. Mack. Boundary-layer linear stability theory. In *AGARD Report 709, Special Course on Stability and Transition of Laminar Flow*, pages 3/1–3/81. AGARD, 1984.
- [13] Thorwald Herbert. Parabolized stability equations. In *AGARD Report 793, Special Course on Progress in Transition Modeling*, pages 4/1–4/34. AGARD, 1993.



- [14] Mujeeb R. Malik. Hypersonic flight transition data analysis using parabolized stability equations with chemistry effects. *Journal of Spacecraft and Rockets*, 40(3):332–344, May–June 2003.
- [15] William L. Oberkampf and Frederick G. Blottner. Issues in computational fluid dynamics code verification and validation. *AIAA Journal*, 36(5):687–695, May 1998.
- [16] Douglass E. Post and Lawrence G. Votta. Computational science demands a new paradigm. *Physics Today*, pages 35–41, January 2005.
- [17] Frederick G. Blottner. Accurate Navier-Stokes results for the hypersonic flow over a spherical nosetip. *Journal of Spacecraft and Rockets*, 27(2):113–122, March–April 1990.
- [18] Helen L. Reed. Computational fluid dynamics validation issues in transition modeling. *AIAA Journal*, 36(5):742–751, May 1998.
- [19] Daniel P. Aeschliman and William L. Oberkampf. Experimental methodology for computational fluid dynamics code validation. *AIAA Journal*, 36(5):733–741, May 1998.
- [20] Les Hatton and Andy Roberts. How accurate is scientific software? *IEEE Transactions on Software Engineering*, 20(10):785–797, October 1994.
- [21] Heath B. Johnson, Trevor G. Seipp, and Graham V. Candler. Numerical study of hypersonic reacting boundary layer transition on cones. *Physics of Fluids*, 10(10):2676–2685, Oct 1998.
- [22] Heath B. Johnson and Graham V. Candler. PSE analysis of reacting hypersonic boundary layer transition. Paper 99-3793, AIAA, June 1999.
- [23] Heath B. Johnson. *Thermochemical Interactions in Hypersonic Boundary Layer Stability*. PhD thesis, The University of Minnesota, 2000.
- [24] Heath B. Johnson and Graham V. Candler. Hypersonic boundary layer stability analysis using PSE-Chem. Paper 2005-5023, AIAA, June 2005.
- [25] Michael J. Wright, Graham V. Candler, and Deepak Bose. Data-parallel line relaxation method for the Navier-Stokes equations. *AIAA Journal*, 36(9):1603–1609, September 1998.
- [26] Heath B. Johnson. *STABL Stability and Transition Analysis for Hypersonic Boundary Layers: Program Reference*. Department of Aerospace Engineering and Mechanics, University of Minnesota, March 2005.
- [27] Joseph L. Steger and R. F. Warming. Flux vector splitting of the inviscid gasdynamic equations with application to finite-difference methods. *Journal of Computational Physics*, 40:263–293, 1981.
- [28] Robert W. MacCormack and Graham V. Candler. The solution of the Navier-Stokes equations using Gauss-Seidel line relaxation. *Computers and Fluids*, 17(1):135–150, 1989.

- [29] Graham V. Candler and Robert W. MacCormack. Computation of weakly ionized hypersonic flows in thermochemical nonequilibrium. *Journal of Thermophysics and Heat Transfer*, 5(3):266–273, July 1991.
- [30] Bonnie J. McBride and Sanford Gordon. *Computer program for calculation of complex chemical equilibrium compositions and applications: II. Users manual and program description*. NASA Reference Publication 1311, June 1996.
- [31] Mujeeb R. Malik. Numerical methods for hypersonic boundary layer stability. *Journal of Computational Physics*, 86:376–413, February 1990.
- [32] Linda Kaufman. Algorithm 496: The LZ algorithm to solve the generalized eigenvalue problem for complex matrices [F2]. *ACM Transactions on Mathematical Software*, 1(3):271–281, September 1975.
- [33] K.F. Stetson, E.R. Thompson, J.C. Donaldson, and L.G. Siler. Laminar boundary layer stability experiments on a cone at Mach 8, part 2: Blunt cone. Paper 84-0006, AIAA, January 1984.
- [34] M.R. Malik, R.E. Spall, and C.-L. Chang. Effect of nose bluntness on boundary layer stability and transition. Paper 90-0112, AIAA, January 1990.
- [35] Vahid Esfahanian. *Computation and Stability Analysis of Laminar Flow over a Blunt Cone in Hypersonic Flow*. PhD dissertation, The Ohio State University, 1991.
- [36] Ewald Kufner, Uwe Dallmann, and Joachim Stilla. Instability of hypersonic flow past blunt cones — effects of mean flow variations. Paper 93-2983, AIAA, July 1993.
- [37] J. Stilla. Engineering transition prediction for a hypersonic axisymmetric boundary layer. *AIAA Journal*, 31(6):1358–1364, November 1994.
- [38] I. Rosenboom, S. Hein, and U. Dallman. Influence of nose bluntness on boundary-layer instabilities in hypersonic cone flows. Paper 99-3591, AIAA, June 1999.
- [39] Steven P. Schneider. Hypersonic laminar instability on round cones near zero angle of attack. Paper 2001-0206, AIAA, January 2001.
- [40] Vahid Esfahanian and Kazem Hejranfar. Accuracy of parabolized Navier-Stokes schemes for stability analysis of hypersonic axisymmetric flows. *AIAA Journal*, 40(7):1311–1322, July 2002.
- [41] Ian J. Lyttle, Helen L. Reed, Alexander N. Shipyluk, Anatoly A. Maslov, Dmitry A. Buntin, Eugene V. Burov, and Steven P. Schneider. Numerical-experimental comparisons of second-mode behavior for blunted cones. Paper 2004-0097, AIAA, January 2004.
- [42] Xiaolin Zhong. Numerical simulation and experimental comparison of hypersonic boundary layer instability over a blunt cone. Paper 2004-2244, AIAA, June 2004.
- [43] Ian J. Lyttle and Helen L. Reed. Sensitivity of second-mode linear stability to constitutive models within hypersonic flow. Paper 2005-0889, AIAA, January 2005.

- [44] F.G. Blottner, M. Johnson, and M. Ellis. Chemically reacting viscous flow program for multi-component gas mixtures. Technical Report SC-RR-70-754, Sandia National Laboratories, Albuquerque, NM, December 1971.
- [45] Frank M. White. *Viscous Fluid Flow*. McGraw Hill, Boston, 2nd edition, 1991.
- [46] Daniel R. Grieser and William H. Goldwaite. Experimental determination of the viscosity of air in the gaseous state at low temperatures and pressures. Technical Report AEDC-TDR-63-143, Arnold Engineering and Development Center, June 1963.
- [47] G.P. Matthews, C.M.S.R. Thomas, A.N. Dufty, and E.B. Smith. Viscosities of oxygen and air over a wide range of temperatures. *Journal of the Chemical Society, Faraday Transactions I*, 72(1):238–244, January 1976.
- [48] E.W. Lemmon and R.T. Jacobsen. Viscosity and thermal conductivity equations for nitrogen, oxygen, argon, and air. *International Journal of Thermophysics*, 25(1):21–69, January 2004.
- [49] Sydney Chapman and T.G. Cowling. *The Mathematical Theory of Non-Uniform Gases*. Cambridge University Press, third edition, 1970.
- [50] Frederick G. Keyes. A summary of viscosity and heat-conduction data for He, A, H<sub>2</sub>, O<sub>2</sub>, N<sub>2</sub>, CO, CO<sub>2</sub>, H<sub>2</sub>O, and air. *Transactions of the ASME*, 73(5):589–596, July 1951.
- [51] Geoffrey C. Maitland and E. Brian Smith. Critical reassessment of viscosities of 11 common gases. *Journal of Chemical and Engineering Data*, 17(2):150–156, February 1972.
- [52] Frederick G. Keyes. The heat conductivity, viscosity, specific heat, and Prandtl numbers for thirteen gases. Technical Report 37, Project Squid, April 1952.
- [53] William J. Taylor and Herrick L. Johnston. An improved hot wire cell for accurate measurements of thermal conductivities of gases over a wide temperature range. *The Journal of Chemical Physics*, 14(4):219–233, April 1946.
- [54] Robert G. Vines. Measurement of the thermal conductivity of gases at high temperatures. *Transactions of the ASME: Journal of Heat Transfer*, 82(2):48–52, February 1960.
- [55] D. Arnal, L. Dussillols, E. Kufner, Y. Oye, S. Shafpar, and Ph. Tran. TRP EAS/ESTEC (SN 7): computational results for transition prediction. Technical report, ONERA, 1996.
- [56] Christopher J. Roy, William L. Oberkampf, and Mary A. McWherter-Payne. Verification and validation for laminar hypersonic flowfields, part 2: Validation. *AIAA Journal*, 41(10):1944–1954, October 2003.
- [57] Fabio P. Bertolotti. The influence of rotational and vibrational energy relaxation on boundary-layer stability. *Journal of Fluid Mechanics*, 372:93–118, 1998.
- [58] Leslie M. Mack. Boundary-layer stability analysis for sharp cones at zero angle-of-attack. Technical Report AFWAL-TR-86-3022, Air Force Wright Aeronautical Laboratories, Wright-Patterson Air Force Base, Ohio, August 1986.

- [59] Kenneth F. Stetson and Roger L. Kimmel. On hypersonic boundary-layer stability. Paper 92-0737, AIAA, January 1992.
- [60] Ivan E. Beckwith, Theodore R. Creel Jr., Fang-Jenq Chen, and James M. Kendall. Free stream noise and transition measurements in a Mach 3.5 pilot quiet tunnel. Paper 83-0042, AIAA, January 1983.
- [61] Mujeeb R. Malik. Instability and transition in supersonic boundary layers. In E.M. Uram and H.E. Weber, editors, *Laminar-Turbulent Boundary Layers*, Proceedings of the Energy Sources Technology Conference, pages 139–147, New Orleans, LA, February 1984. ASME.
- [62] I. Rosenboom, St. Hein, and U. Dallman. Numerische untersuchungen des einflusses der nasenstumpfheit auf grenzschichtinstabilitäten bei axialsymmetrischer kegelumströmung im hyperschall. Technical Report IB 223-98 A 34, Institut für Strömungsmechanik, DLR Göttingen, October 1998. (In German).
- [63] E. Kufner. *Numerische Untersuchungen der Strömunsinstabilitäten an spitzen und stumpfen Kegeln bei hypersonischen Machzahlen*. PhD thesis, University of Stuttgart, 1994. Also DLR-FB 95-11. (In German).
- [64] Shann J. Rufer and Steven P. Schneider. Hot-wire measurements of instability waves on a blunt cone at Mach-6. Paper 2005-5137, AIAA, June 2005.
- [65] Ames Research Staff. Equations, tables, and charts for compressible flow. Report 1135, NACA, 1953.
- [66] John D. Anderson Jr. *Hypersonic and High Temperature Gas Dynamics*. AIAA, Reston, Virginia, 2000.

## APPENDICES

## Appendix A: Typical N-Factor Script

An example script used to run multiple combinations of starting location, frequency, and spanwise wavenumber is given below.

```
#!/usr/bin/perl

# Reference the pse_scripting library routines
require "../lib/pse_scripting.lib";

# Set the directory in which to store the results
my $od= "/home/trobarge/pseruns/133";
my $pid= $$;

# Set number of processors
my $np=2;

# Set up the parameter space for the test matrix
my @sdists= map {$_/50;} (1..3);
my @freqs= map {$_*25;} (1..10);
my @betas= map {$_*1000;} (1..8);

# Set PSE-Chem options to be used for all runs
my %params= (iest_omeg=>0, iftest3=>1, ltest3=>0,
             flow=>0.2, fhigh=>1.0, istep_march=>1,
             mean_flow_file=>"../out/first145.bin",
             ichem_on=>1, ivib_on=>1, idiff_on=>1);

# Create status file - deletion stops the run
my $statusfile= psechem_statusfile_new(".", 'continue');
```

```

print "-- Status file is: $statusfile\n";

# Make the main output directory if it doesn't already exist
if (!-d $od) {
    mkdir($od);
    if (!-d $od) {
        die "Unable to make output directory '$od'\n";
    }
}

# Loop over frequencies and set options for each loop
foreach my $f (@freqs) {
    $params{omega1}=$f;
    $params{omega2}=$f;

# Loop over starting locations and set option for each loop
    foreach my $s (@sdists) {
        $params{"start_sdist"}= $s;

# Loop over betas and set options for each loop
        foreach my $beta (@betas) {
            $params{beta0_local}=$beta;
            $params{beta0_pse}=$beta;

# Name run according to individual parameters
            my $run="$f-$s-$beta";

# Options to pass to PSE-Chem solver
            my @oargs= (-np=>$np, -copy_to=>$od, -id=>"$run",

```

```

        -args=>"> $od/psechem.$run.out",
        -outdir=>"../out/pserun.$pid.data");

# Pass options to input file and solver and run using library routine
print "-- Running PSE-Chem on case $run\n";
my %ret= psechem_run_solver(-infile=>%params,@oargs);
psechem_check_error(%ret);

# Check status file to see whether to continue
my $status= psechem_statusfile_check($statusfile);
if ($status=~ /abort/) {
    print "Stopping. Status file contains: $status\\\n";
    if (-f $statusfile) {unlink($statusfile);}
    exit;
}
}
}

# Remove status file and exit when all runs finished
if (-f $statusfile) {unlink($statusfile);}
print "\n-- Done --\n\n";
exit;

```



## Appendix B: STABL User's Guide

This appendix is designed to be a guide to using STABL from a user's perspective. It supplements the extensive documentation included with the STABL distribution. This is believed to be accurate as of July 2005, but since STABL is still under active development, many of the details provided here may become obsolete, and the STABL documentation should be considered the authoritative source.

The opinions given in this appendix are my own, and they should not be construed as those of STABL's developers. I will describe the lessons I have learned, the way I used STABL and set up the environment, and in some cases the way I wish I had. Individual preferences will vary, and I don't claim to have found the best way to do everything, so use this as a guide, not as a directive.

### B.1 Prerequisites

#### Hardware

STABL parallelizes very efficiently, allowing it to effectively utilize the resources of a large cluster supercomputer, but it can also run fully on a single workstation. This section will summarize my experiences and recommendations.

I was given access to an 812 processor cluster at Sandia National Laboratories, and I used that computer to run most of my mean flows. I typically used 8–16 processors at a time, and grids with 150,000 points would converge in approximately six hours with no user intervention. If necessary, I could be more aggressive in increasing the CFL number and freezing, and significantly reduce the time to converge, but this was normally not worth the user-time involved, given the complexity caused by the batch system and the need for remote operation and file transfers. I also occasionally used the Sandia cluster for PSE-Chem runs, particularly when I ran scripts involving large numbers of global and local frequencies, since those portions of the code parallelize well.

I used a dual processor Symmetric Multi-Processing (SMP) workstation for the majority of my time with STABL. It was a Dell Precision 650, which was their largest workstation model at the time it was purchased. The workstation contained two 3.06 GHz Intel Xeon processors, each with 1 MB of L3 cache. The system had 2 GB of ECC SDRAM and an 80 GB IDE hard drive. Graphics were rendered by a dual-monitor-capable nVidia QuadroFX 500 graphics card with 128 MB of video RAM. A CD-RW/DVD drive, 3.5 inch floppy drive, keyboard, and mouse were also included. No monitors were purchased, as suitable used monitors were available free of charge from the University. The total cost of the system in May 2004, including academic and volume pricing, was \$2,628.80.

In retrospect, all of the computations presented in this thesis could have been done on the workstation alone, although the Rufer sensitivity studies would have taken considerably longer. The mean flows could be obtained in 2–3 days, and the workstation could still be used for other, less processor-intensive tasks such as data analysis in the mean time. There would be a significant effect on the system response time for other tasks, but if the full capability of 4 GB of RAM had been purchased and the process prioritizing ability of Linux was used, the effect could be greatly decreased. However, the nature of the work in this thesis was limited by analysis time, rather than CPU cycles. If, for example, a parametric study was performed to obtain transition Reynolds numbers for many combinations of flow and geometry variables, the analysis load for each individual solution would be much smaller, and CPU cycles would become the limiting factor. Therefore, the necessity of supercomputer access will probably depend on the manner of usage of STABL.

Irregardless of supercomputer availability, a quality workstation is essential for intensive use of STABL. The workstation will at a minimum be used for compilation, post-processing, and data analysis. I found the workstation described above to be excellent for all of those tasks. A high end graphics card is not necessary for 2D/axisymmetric data visualization, and the reasonably priced card chosen allowed me to use two monitors to double the effective size of my workspace, which greatly

increased my productivity. I found the processor speed and amount of RAM fully adequate for my purposes. Changes I would make now would be to purchase a DVD writer to assist in data backup and a SCSI hard drive instead of IDE for faster data transfer.

I found it useful to have a fixed IP address and registered host name. Since I accessed the Sandia cluster remotely through SSH, this allowed me to connect back to my workstation from Sandia to transfer files in a single step rather than through a proxy. In addition, I could connect to the workstation from home in the evenings and weekends to monitor the status of ongoing computations.

## **Software**

STABL was written in and for a UNIX environment. Many varieties of UNIX are available; I recommend using Linux if a new system is used. All of my computations were done using Red Hat Linux 9. The workstation came with Windows loaded; Linux was installed locally, with Windows retained on a second partition. Other varieties of UNIX should work fine once initial setup is complete, although there may be some extra work if this is the first time STABL has been used on that particular variety. It may be possible to run STABL under Windows using Cygwin, which is a freely available program that provides a UNIX environment on a Windows operating system. Currently, this has never been tried extensively, and I would highly recommend Windows users either use a second computer or create a dual-boot system with Linux.

STABL is distributed in source form, so C and Fortran compilers are needed to create the binary executable files. I originally used the GNU compilers, but later switched to the Portland Group compilers for reasons described in Section 3.2.9. Theoretically, the Intel compilers should work also, although these have not been used yet to my knowledge. The Portland Group C and Fortran compilers were downloaded from the website and installed on the workstation using the license manager

option. This was slightly more complicated to set up, but it allowed multiple users access to the compilers. The details are described in the compiler documentation. A Perl interpreter is also required for the GUI, scripting capabilities, and many of the additional utilities. This is usually installed by default on UNIX systems, and a Windows version can be downloaded free of charge from <http://www.activestate.com>. The STABL documentation contains detailed information on the installation of additional Perl modules that are required.

DPLR2D and PSE-Chem use MPI libraries for message passing between multiple processors. Several versions of MPI are available; I installed the MPICH MPI libraries, which are freely available online. The LAM MPI libraries were also tested, and no effect was seen on the results. I found it best to set up the compilers before setting up the MPI libraries so that the `mpif90` and `mpicc` commands could be properly configured. The Portland Group website FAQ contains information about setting up their compilers with MPICH.

The commercial data visualization software Tecplot was used extensively for analysis of the results. STABL is designed to format its data files to be Tecplot-ready, although it would not be very difficult to change the source code so that another formatting is used. A single commercial license of Tecplot currently costs \$1600, and an educational license is approximately \$800. Many institutions will have a site license which would make Tecplot available at no additional cost, as was the case for me.

## Knowledge

STABL is an advanced system, and users more experienced with CFD and transition prediction will have an easier learning curve than others. In particular, a working knowledge of CFD principles, as can be gained in an introductory course, will be very helpful. A user should be reasonably proficient in using the command line in UNIX. Knowledge of Fortran is only strictly necessary to understand the

source code, but that would be beneficial, since the code is still under active development. A basic knowledge of scripting in Perl is necessary to utilize the advanced operation methodologies currently being developed. While only basic knowledge in these areas is necessary to use STABL, more advanced users will be better able to exploit the full capabilities of the software.

## B.2 Method of Operation

The STABL documentation gives a detailed tutorial to allow a user to run a case with all of the correct options in place. While this is sufficient to teach the new user how to execute the proper commands, it does not teach why those options were set and when a user will want to change the defaults. This section is an attempt to fill that gap with some of the lessons I learned over the course of my time using STABL.

### Case Definition

The first step in analyzing a new case is to gather the relevant information about that case. What you need depends on your goals for the analysis, but at a minimum you will need the model geometry, the freestream properties, and the wall temperature boundary condition. The information needed for the model geometry depends on the class of problem. For a blunt cone, you will need the nose radius, the half angle, and the arclength from the sphere-cone tangency point to the end. For the input conditions, you will need the freestream Mach number or velocity, the freestream static translational temperature  $T_\infty$ , the freestream static vibrational temperature  $T_{v_\infty}$ , and the freestream density. You will most likely need to calculate the density from other parameters. Be careful in doing this to ensure you are doing it in a way that is consistent with the goal of the analysis; see Section 3.2.2 for more discussion of this. For the wall temperature condition you can specify a constant temperature, a temperature distribution, radiative equilibrium, or an adiabatic wall.

You may need other information to make use of the STABL results. If you want to compare to experiments, you will need data such as the experimental transition location or the wall temperature or pressure distributions. For transition prediction, you will need to specify an  $N$  factor appropriate for the environment. It would be helpful to know the relative uncertainty in the various input quantities so that at least basic sensitivity studies can be performed.

## **Grid Generation**

The first step in the analysis is to generate a grid. I used the STABL GUI to run the grid generator. The model geometry is used to define the inner boundary. The outer boundary should be tailored to match the angle of the shock as closely as possible. At least five or six grid points should stand between the shock and the domain outer boundary to ensure the shock is well captured.

The problem with matching the grid to the shock shape is that the shock shape is not known at the outset. To get around this, I recommend using two grids. To make the first, use the graphs in NACA Report 1135 [65] or Billig's correlation [66] to obtain an approximate outer shock angle. Apply a generous margin of error and create a large, coarse grid that you are sure will completely capture the flow. Run the solution for this case, which due to the small problem size and low aspect ratios should converge very quickly. Postprocess the solution and plot Mach number contours in Tecplot. I like to make the shock the only contour level shown to enhance the contrast. Then make a second grid that will better match the shock. Read the grid file into Tecplot and overlay it on the contours. I like to activate only the contour layer in the original solution and only the mesh or boundary in the new grid. Now go back to the GUI and make another, better grid that uses the lessons learned. Continue doing this until your new grid matches the shock shape. I typically use around ten line segments in constructing the outer grid shape for a blunt cone. Tecplot macros can make the iterations go much faster. Increase the number of

points in the second grid. The spacing factors may have to be changed to place sufficient points within the boundary layer. The boundary-layer thickness can be approximately determined from the first solution, as well.

After the second grid is created, save your work and run the mean flow solver. Be sure to check that your grid still matches the shock well and the spacing within the boundary layer is sufficient in the final solution.

## Mean Flow Solution

The next step is to obtain the laminar mean flow. The STABL documentation gives a good description of how to run the solver. I will focus on how to set up the problem and various choices that need to be made. Most of the work is in setting up the input file. Brief descriptions of each of the options are given at the bottom of the sample file. I will focus on the ones that you are most likely to need to change from the defaults.

The grid filename is self-explanatory. `iwall` should be 1 for an adiabatic wall, 2 for an isothermal wall, 3 for a specified distribution, or 4 for radiative equilibrium. For an isothermal wall, the temperature is specified by `Twall`, and for a specified distribution it is given in the file declared as the `wall temperature filename`. `istop` gives the total number of iterations to perform in the run. If you restart from a previous run, the iteration count resets for the purposes of `istop`. To restart, change `iconr` to 1, ensure that the `<BASE>.flow` file is in the `../out` directory, and run the solver with the normal command.

The `kbl` parameter is most likely to be overlooked. In layman's terms, this tells the solver at which  $j$  value it should toggle a limiter that results in an increase in the effective viscosity. This should be set to a  $j$  value such that is at every  $i$  beyond the boundary layer edge but inside of the shock. A suitable value should be determined when the second grid is created. If this is set to a value within the boundary layer, discontinuities may appear in the profile derivatives.

`nplot` specifies the interval of iterations between writing restart files. I adjust this based on the problem size and system used so that it writes a restart file every minute or two. `igeom` should be set to 1 for a blunt cone or 3 for a sharp cone. `ichem` and `ivib` settings are at your discretion. They should probably both be 1 unless you are trying to compare to another computation or assess the real gas effects. The initial CFL number is set through `cfl`, and subsequent numbers to change to are listed after the mass fractions. The CFL is changed every `ijump` iterations. The freestream conditions and the mass fractions will also need to be set; those are self-explanatory.

I prefer to run new cases on my workstation first, where I can easily monitor the progress, start and stop easily, and experiment with different CFL numbers. Once I have gained confidence that the solution is converging well, I will transfer it to the cluster, where it runs faster but is much more difficult to monitor.

The mean flow code gives you the option to change the freezing level and CFL number while it is running. This capability is very useful in a batch-scheduling system where restarting the job may mean going to the end of the queue. However, if you increase the CFL number too aggressively, the solution may blow up. For this reason, I was often overly conservative and would let the solution converge slower than it needed to. However, I gained the flexibility to let it run unattended and it would eventually converge.

After the residual has leveled off, you should postprocess it and look for several factors. First, plot contours of the residual on a logarithmic scale. I used a Tecplot macro to easily automate this. I always saw slightly higher residuals near the nosetip in the boundary layer, but other “hot spots” should be examined carefully. Look at the shock shape to make sure the grid matches the angle while maintaining a reasonable standoff distance. A good check is to probe at various points outside the shock to ensure that the freestream values were maintained. I also like to look at velocity and temperature profiles to ensure that they look reasonable before proceeding to the stability analysis.



## Stability Analysis

The final step is to complete the stability analysis. This step is particularly dependent upon the goals for the analysis. Predicting transition is relatively easy. The walkthrough included with the STABL release gives good examples for obtaining N factors and LST amplification curves. Almost all of the plots I show in this thesis were obtained using the PSE scripting routines with setup files modified from the examples provided. To obtain N factors for transition prediction, I recommend running a two-parameter test matrix with combinations of frequency and starting location. For first mode N factors, the  $\beta$  value is a third parameter that must be varied.

After the runs are completed, use command-line wild-card expansion to load all of the `psealpha` files into Tecplot. Plot each of the N factors, and select the maximum N factors for each frequency. A routine has just been added to STABL to extract the most unstable modes automatically, but I have not tried it myself. The predicted transition location will be where the maximum N factor first reaches the preset value. Amplification rate curves and eigenfunctions can be plotted if desired. Other work will be determined by the goals of the study.

There are several input file parameters that I change on a regular basis. The parameters `mean_flow_file`, `start_sdist`, `iselect_freq`, `beta0_local`, `beta0_pse`, and `iest_omeg` are all well explained in the documentation and in the descriptions in the input file. I vary `num_coarse` and `num_fine` depending on the application, but I rarely increase them over the default values. I normally leave `ichem_on`, `ivib_on`, and `idiff_on` set to 1 unless I am specifically testing their effect. I have not seen an effect between the various settings of `istr`, with the exception of the uniform setting. I normally leave that at 1, since I use high-quality mean flow grids. I use a `bl_method` of 3, but you should check to see if the boundary layer edge location is reasonable. I have experimented with most of the other options, and I recommend

that other users do the same, but those are the ones I generally considered when setting up a new case.

### **B.3 Final Thoughts**

Hopefully this users' guide has filled some of the gaps in the STABL documentation and provided a slightly different perspective on the working of the code. I would encourage you to ask questions and to try out the many options available. The PSE-Chem source code is well documented and laid out, so you can often look directly at that section of the code to learn the differences between the various options. Take careful notes, and always save your input files. If you have your input files, you can recreate your data; if you only have your data, you may not be able to determine how you obtained it. Best wishes.

## Appendix C: Boundary Layer Edge Detection

The edge detection algorithm was modified to account for overshoots in the total enthalpy profiles. The file `STABL/cfd_solver/src/cfd_detect_bl_edge.fpp` was the only file modified. A partial listing of the source code is shown below.

```

c      *** Total enthalpy method
      if (imethod.eq.1) then

          hp= rbl_fact

          hf= h(nj)           ! Freestream value
          hw= h(1)            ! Wall value
          hd= abs(hf - hw)     ! Difference

c      *** Initialize variables
          jedge = 0
          ioversht= 0

c      *** First use original method
          do j= 1,nj-1
              if (abs(h(j)-hw) .ge. hp*hd) then
                  jedge = j
                  jfirst= j
                  exit
              endif
          enddo

          if (jedge.eq.0) goto 999

c      *** Find out if an overshoot exists

```

```

do j= jfirst+1,nj
    if ((h(j)-hw) .gt. hd/hp) then !overshoot exists
        ioversht= 1
    endif

c    *** Next line makes sure we're past overshoot and checks the flag
c    *** to make sure it isn't fooled by random fluctuations in the freestream
    if (iand(ioversht==1,h(j) .lt. h(j-1))) then
        if ((h(j)-hw) .lt. hd/hp) then
            jedge= j
            exit
        endif
    endif
endif

enddo

```

## Appendix D: Input and Output Data for Rufer's 45 psia Blunt Cone

This appendix is designed to provide all of the input data needed to recreate the plot shown in Figure 5.13. The case is Rufer's blunt cone with a stagnation pressure of 45 psia. Computations were performed in May 2005 using STABL 1.29.2.

The mean-flow input file is provided in Section D.1. All of the inputs needed for the GUI elliptical nose grid generator are provided in Table D.1. A script that can be used to generate the PSE data is printed in Section D.2. Mean-flow output data is tabulated for several locations in Table D.2. N factors for several frequencies and locations are printed in Table D.3.

### D.1 Mean Flow Input File

```
! Grid filename,
'../grids/grid_shann150.dat'
! chemistry input filename,
'../props/air_5sp_88.inp'
! wall temperature filename,
'../inp/twall.inp'
! NASA thermodynamic properties filename
'../props/nasa_1996_thermo.dat'

!   itvd      iorder   iextst      kmax      ivis      iwall      i2j
      -1,        2,      -1,        4,        1,        2,        2
!   istop      iplot    iconr      iaxi      inor      isn      kbl
      50000,      1,      -1,        1,        1,        0,      220
!   nplot      igrd     ilt      i2n      igeom      irm      iej
      100,        1,      -1,        5,        1,        1,      -1
!   ichem      ivib     itv      itl      irk      iset      icfljmp
      1,          1,        1,      -1,        1,        1,      20
```

```

! machin      density      Tin      Tvin      Twall      vin      rvr
    5.80d0,   1.5046d-2, 5.6000d1, 5.6000d1,   3.00d2, 3.06000d3,   1.3d0
!   cfl      epsi      epsj      epsk      pmul      alpha      yaw
    1.0d-3,      0.3,      0.3,      0.3,      0.5,      0.0d0,   0.0d0
!  stime      rconv  rfreeze  racccl  vaccel      emisw  radrx
    10.0      0.5d-7      -1.0      1.0d+5      1.0d+5      0.8d0      0.5d0

! Mass fractions, species order: N2,O2,NO,N,O
    0.767000
    0.233000
    0.000000
    0.000000
    0.000000

! List of additional CFL numbers
0.01
0.1
1.
2.
4.
10.
20.
40.
100. , 5
200. , 5
400. , 20
1000.
-1

```

Table D.1: Grid input conditions for Rufer's 45 psia blunt cone.

Major (x) nose radius			0.000508 m	
Minor (y) nose radius			0.000508 m	
Number of points on nose			80	
Major (x) axis upper grid radius			.00141	
Minor (y) axis upper grid radius			.00120	
Upper grid x offset			0.0008	
Number of body-normal points			351	
Nose grid point spacing factor			0.07	
End grid point spacing factor			0.09	
Surface-normal stretching type at nose			Exponential	
Surface-normal stretching type at end			Exponential	
Elliptical smoothing iterations			3	
Overlap correction factor			0.30	
Normal relaxation factor			0.30	
Segment	Angle (deg)	Length (m)	Num Points	Spacing
Lower Segment 1	7	0.0267	150	Automatic
Lower Segment 2	7	0.53808	211	Automatic
Upper Segment 1	35	0.0003	10	Automatic
Upper Segment 2	32.5	0.0002	10	Automatic
Upper Segment 3	30	0.0005	10	Automatic
Upper Segment 4	25	0.0007	10	Automatic
Upper Segment 5	20	0.0012	10	Automatic
Upper Segment 6	18	0.0025	10	Automatic
Upper Segment 7	16	0.006	10	Automatic
Upper Segment 8	14	0.03	10	Automatic
Upper Segment 9	13.1	0.6	281	Automatic

## D.2 PSE Script

```
#!/usr/bin/perl
require "../lib/pse_scripting.lib";
my $od= "/home/trobarge/pseruns/139";
my $pid= $$;
my $np=2;
## Locations at which to start
## Want to be able to specify x distances to match experiments
## and automatically convert them to s distances
## Use general formula for x to s on frustum of sphere-cone
# Set up parameters:
my $Rn=0.000508; # Nose radius in meters
my $phi=7; # Cone half angle in degrees
my @xdist= map {$_/2;} (1..16); # Distances to run in inches
my (@sdist);
# Convert phi to radians:
my $pi=3.14159;
my $phirad=$phi*$pi/180;
# Convert each point
foreach my $x (@xdist) {
    my $slong=$pi*$Rn/180*(90-$phi)+
        ($x*.0254-$Rn*(1-sin($phirad)/cos($phirad)))/cos($phirad);
    $slong=~/([\d\.]{6})/;
    push @sdist, $1;
}
## Frequencies to run
my @freqs= map {$_*10;} (1..30);
# Set PSE-Chem parameters
```



```

my %params= (iest_omeg=>0,iftest3=>1,lstest3=>0,
             flow=>0.2,fhigh=>2.5,istep_march=>3,
             mean_flow_file=>"../out/shann150.bin");
# Make the main output directory if it doesn't already exist
if (!-d $od) {
    mkdir($od);
    if (!-d $od) {
        die "Unable to make output directory '$od'\n";
    }
}
foreach my $f (@freqs) {
    $params{"omega1"}= $f; $params{"omega2"}= $f;
    my $count=0;
    foreach my $s (@sdist) {
        # Identify runs by xdist in inches
        my $run="$f-$xdist[$count]";
        $params{"start_sdist"}= $s;
        my @oargs= (-np=>$np,-copy_to=>$od,
                   -args=>"> $od/psechem.$run.out",
                   -id=>$run,-outdir=>"../out/pserun.$pid.data",
                   -machinefile=>$machines);
        # Run PSE-Chem
        print "-- Running PSE-Chem on run $run\n";
        my %ret= psechem_run_solver(-infile=>\%params,@oargs);
        psechem_check_error(%ret);
        $count++;
    }
}
exit;

```

Table D.2: Selected mean-flow data points for Rufer's 45 psia blunt cone.

$i$	$j$	x	y	u	v	T	rho1
100	100	0.000649426	0.00054862	166.748	23.6314	302.1	0.00851877
200	100	0.00556437	0.00120189	169.859	20.8005	304.759	0.00401514
300	100	0.153165	0.0200131	475.453	58.0136	255.638	0.00494973
400	100	0.423942	0.0545917	761.355	93.5567	138.664	0.00904155
380	1	0.361808	0.0448739	0	0	300	0.00418237
380	21	0.361782	0.0450876	90.1133	11.0512	304.538	0.00412025
380	41	0.361748	0.0453598	203.443	24.9148	301.709	0.00415896
380	61	0.361707	0.0456987	343.936	42.0663	284.934	0.00440401
380	81	0.361655	0.0461207	517.583	63.2922	243.29	0.00515838
380	101	0.36159	0.046646	719.269	88.2518	161.753	0.00776011
380	121	0.36151	0.0472999	848.891	104.766	72.5221	0.0173031
380	141	0.36141	0.0481142	851.67	103.487	67.8951	0.0184762
380	161	0.361286	0.0491279	851.916	101.358	67.9034	0.0184585
380	181	0.361131	0.0503899	852.243	98.8221	67.8784	0.0184351

Table D.3: Selected PSE N-factor data for Rufer's 45 psia blunt cone.

$\omega$ (kHz)	Starting $x$ (inches)	N factor				
		$s = 0.1$	$s = 0.2$	$s = 0.3$	$s = 0.4$	$s = 0.5$
100	4.0	0	0.0485344	0.1259	0.240659	0.546947
120	5.0	0	0.0226291	0.159789	0.920884	2.69965
140	1.0	0	0.0422786	0.846723	2.76787	3.2411
160	6.5	0	0.195131	2.03906	2.30514	1.33935
180	0.5	0	0.988848	1.9931	0.857645	0
200	4.0	0	1.50983	0.74352	0	0
220	1.0	0.118642	1.20406	0	0	0
240	1.0	0.333265	0.298658	0	0	0
260	2.5	0.493529	0	0	0	0
280	2.0	0.582963	0	0	0	0
300	1.5	0.288483	0	0	0	0